Radiation-induced Deep-level Defects in CCD Imaging and Spectroscopy Sensors

Thesis

Radiation-induced deep-level defects in CCD imaging and spectroscopy sensors

Thesis submitted for the degree of

Doctor of Philosophy

at The Open University

by

Daniel Wood

Centre for Electronic Imaging

School of Physical Science

Faculty of STEM

The Open University

Radiation-induced deep-level defects in CCD imaging and spectroscopy sensors

Daniel Wood

Abstract

This thesis is concerned with the analysis of radiation-induced defects within the silicon lattice of a Charge-Coupled Device (CCD) image or spectroscopy sensor and particularly those defects with energy levels which can trap charge as it passes through a device, ultimately leading to image quality degradation. A novel technique for the study of certain defect levels within the silicon lattice in a CCD is introduced and developed, allowing for the analysis of individual defects and providing high spatial and temporal resolution. The technique and results both have potentially important consequences for CCD characterisation and use; particularly in the case of space-based detectors for which the radiation environment is harsh and the sensor performance specifications increasingly demanding.

CCDs currently constitute the standard sensor for large-scale space-based telescopes such as the Hubble Space Telescope (HST), GAIA, EUCLID etc. Through design processes, careful device optimisation, and post-image correction algorithms the effects of radiation-induced image degradation can be mitigated to levels which have, until now, been sufficient. However the increasingly ambitious scientific goals of such missions (the upcoming EUCLID mission being a prime example) place more and more stringent demands on sensor performance. Therefore further analysis of the defects responsible for loss of image quality is required to enable more efficient and detailed correction algorithms to be implemented, as described in Chapter 3 of this thesis. Current, well-established defect analysis techniques may not have the ability to provide the accuracy required for future missions and so in Chapter 4 a relatively new technique of single trap-pumping is introduced and developed for our research aims. Using

this technique both p-channel (Chapter 5) and n-channel (Chapter 7) CCDs are analysed, with the primary aim being to measure defect emission time constants (the length of time between the capture and emission of a charge carrier at a defect level) since this is the property of a defect level which most strongly affects its ability to degrade an image, depending on the operational conditions of the device. A number of important defects are studied over a range of temperatures allowing for further defect parameters, such as energy level, to be deduced.

Defect emission time constants are highly temperature-sensitive and so the dominant charge-trapping defects differ depending on the operational temperature of the device and the clock timings used. The effect of device temperature during irradiation on the defect distribution within a CCD is investigated in Chapter 6 using a p-channel CCD irradiated with protons at 153K. The results show large differences between this device and one irradiated at room-temperature, which is currently the standard practice for device characterisation and testing for all space missions. This is an important result which shows that current irradiation testing procedures may require changing as device performance specifications become more and more demanding. Further potential uses of the trap-pumping method as a defect analysis tool are outlined in Chapter 8 before the entire results are summarised.

Declaration

I hereby declare that no part of this thesis has been previously submitted to this or any other University as part of the requirement for a higher degree. The work described herein was conducted solely by the undersigned except for those colleagues and other workers acknowledged in the text.

Daniel Wood

Dedication

To all those whose efforts have put me in a position to do what I enjoy.

Acknowledgements

Numerous people have contributed to the work in this thesis and I would like to express my gratitude to them.

Firstly I would like to thank my lead supervisor Dr. David Hall for his knowledge, support and enthusiasm throughout the entire study.

Dr. Jason Gow for all of his support, particularly with my experimental work. I would also like thank him for the RADECS 2016 conference which was one of the highlights of my time at the OU.

Prof. Andrew Holland for his faith in me and for improving my morale with his regular jibes.

Dr. Peter Turner, for interesting discussions and for kindly providing me with the CCDs for my study.

Dr. Neil Murray, for his expertise and time in helping me in developing my CCD sequencer and camera system.

Dr. Jesper Skottfelt, for his great contribution to the RADECS work and for his excellent simulations which enabled me to solve a problem that had eluded me for a long time!

Laura, who has always been my greatest supporter. Her belief in me has been such a great source of motivation and I will never forget that. For everything she does that makes me smile.

Aga! For our talks which always made me feel better, and for continually being a great friend to me at the OU.

Ewan, forever my physics brother!

All of the current and former students and members of the CEI, for their help and support regarding numerous aspects of my work and my time at the OU;

I would also like to gratefully acknowledge the financial support received from both the Science and Technologies Facilities Council and Teledyne e2v during my research.

Finally I would like to thank my family for their continued support and faith throughout my studies.

List of acronyms

ADC – Analogue to digital converter

CCD – Charge-coupled device

CDS – Correlated double sampling

CTE/CTI – Charge transfer efficiency/inefficiency

DLTS – Deep-level transient spectroscopy

DN – Digital numbers

EPER – Extended pixel edge response

EPR – Electron paramagnetic resonance

ESA – European Space Agency

FF – Fringing-fields

FPR – First pixel response

FWHM – Full-width half maximum

HST – Hubble space telescope

MOS – Metal-oxide-semiconductor

NIEL – Non-ionizing energy loss

PKA – Primary knock-on atom

QE – Quantum efficiency

ROI – Region of interest

RT – Room-temperature

SPENVIS – Space environment information system

SRH – Shockley-Read-Hall

VO – Vacancy-oxygen

VP – Vacancy-phosphorous

Contents

Chapter 1 - Introduction

For many imaging and spectroscopic applications the CCD is the detector of choice, both for terrestrial and space-based use. As such they are generally very well understood and can be produced with exceptional charge transfer performance specifications, allowing for extremely high resolution imaging. The performance of a CCD is however degraded over time when it is used in an environment where radiation in the form of charged particles and electromagnetic waves can damage the silicon lattice of the device. Among the number of effects of radiation damage is the formation of stable defect centers, some of which can introduce energy levels into the otherwise forbidden silicon bandgap. These energy levels provide transition states for the capture and emission of charge carriers between bands and can act as trapping centers, leading to loss of signal charge and image degradation. The ability of a particular defect level to affect an image is dependent both on the physical properties of the defect level itself and the operational conditions of the CCD.

The effects of radiation damage can reduce the effective lifetime of a detector and put at risk the scientific goals of a mission. Current methods for mitigating radiation damage effects involve careful device optimisation and post-imaging correction techniques; either through forward modelling of charge through a damaged CCD, as used for HST (Massey, 2010), or through an analytical charge distribution model, as used for the ESA GAIA mission (Short, 2013). Both have been shown to be successful in reducing the effects to acceptable levels for the respective missions, however the scientific goals of future space missions are becoming much more demanding, requiring us to see further, fainter and more clearly. To observe lower signals and to measure positions and shapes with better sensitivity, the levels of radiation damage mitigation and correction required have increased dramatically. With knowledge of the precise densities and properties of radiation-induced traps in a CCD one can both:

- Optimise the device more effectively, choosing with greater precision suitable temperatures and clock timings for operation.
- Correct with greater accuracy using post-imaging techniques. For example HST is currently able to correct up to 98% of radiation-induced damage (Massey, 2014) however the proposed ESA EUCLID mission will require up to a 10x greater level of correction (Massey, 2013). This will only be possible through work such as that in this thesis to study defects with a high degree of precision.

This thesis aims to study the predominant charge-trapping defect levels in an irradiated CCD with particular focus on the emission time constant of a level, which is the length of time between the capture and emission of a carrier from the level and is the parameter of most importance for charge transfer performance. The relatively new technique of single trap-pumping is developed for the direct analysis of the emission time constants of individual defects within the CCD lattice and gives excellent resolution. Through analysis of many defects of the same species a distribution is produced allowing for the emission time constants to be quoted with good confidence; in contrast to current analysis methods which deduce the time constant as a secondary parameter. Through analysis across a range of temperatures the defect energy level can also be calculated, further helping the identification of defect species. Through a better understanding of the defect emission time constants and their temperature dependence it is possible to increase the useful lifetime of a detector through optimisation and post-imaging correction algorithms.

This work is broadly split into three sections. The first involves the development of the single trap-pumping technique as a tool for defect analysis, and use of it to study a proton irradiated p-channel CCD. P-channel CCDs represent a variant of CCDs which are currently not used extensively in space, however it has been suggested that they may be more tolerant to radiation damage for certain applications. Through the timing of this work with a wider ESA-funded study into p-channel CCDs for use in space it was possible to test such a device with the added aim of confirming the credentials of

the trap-pumping technique. The two dominant charge trapping defects in p-type silicon are studied; the donor level of the silicon divacancy and the carbon interstitial defect. This work is outlined in Chapters 4 and 5.

The second part of this work (Chapter 6) is an in-depth study of the effect of temperature on the defect distribution of an irradiated CCD and particularly the device temperature during the irradiation. Temperature governs the silicon lattice energy and so is expected to play a vital role in determining defect formation and interaction rates. Currently almost all pre-mission radiation testing is carried out on devices irradiated at room-temperature, however in space devices will operate at cryogenic temperatures as they receive damage. Through analysis of a p-channel CCD irradiated at 153K and subsequently annealed at room-temperature (over several stages) the effect of temperature is investigated. Comparison of the defect distributions from this device with devices irradiated at room temperature provides insight into the radiation damage process and allows for improved testing in the future.

The third part of this study involves the set-up of a standard CCD test-bench and the use of the trap-pumping technique to study a more “standard” n-channel CCD over numerous temperature ranges. In n-channel CCDs the dominant charge trapping defects have been studied extensively, particularly the vacancy-phosphorous defect which is often cited as the most significant in terms of signal charge loss. In this work however focus is paid to defects which have the potential to most affect delicate shape measurements such as those outlined for the ESA EUCLID mission, therefore particular attention is paid to the double-acceptor level of the silicon divacancy. Through improved accuracy of defect parameters devices can be optimised more efficiently depending on the specific requirements of the CCD, and post-imaging damage mitigation algorithms can be improved to the levels demanded by the expanding science goals of space-based telescopes. This work is the subject of Chapter 7. In Chapter 8 additional tests are carried out which aim to provide a start point for potential future investigations into effects such as how the CCD gate voltage affects emission time

constants. This gives an opportunity to outline further areas where the benefits of the single trap-pumping technique may have great value.

In summary, the main research aims of the work in this thesis are as follows:

- The significant development of the single trap-pumping technique as a tool for defect analysis.
- Analysis of charge-trapping defect parameters in both n-channel and p-channel CCDs with particular focus on defect level emission time constants, to provide the accurate data required for device optimisation and damage correction.
- A study of the effect of device temperature during irradiation on the defect distribution in a p-channel CCD.
- Analysis of defect evolution in a cryogenically irradiated CCD immediately following irradiation and after room-temperature anneals of varying lengths.

Chapter 2- Semiconductor basics and CCD image sensors

The CCD is the detector of choice for many imaging and spectroscopic applications due to its high sensitivity, linearity and dynamic range. The focus of this work is the CCD image sensor and in particular the detrimental effects of radiation damage on CCDs. To understand the radiation damage effects (which are discussed in detail in Chapter 3) a basic working knowledge of the CCD and its operation is required. Presented here is a brief introduction to the semiconductor physics principles which govern CCD operation, leading to a discussion of Metal-Oxide-Semiconductor (MOS) devices and then the CCD itself. This provides a basic overview which is sufficient for the purpose of this work, with the reader directed to literature such as Janesick (2001) for a complete review of the CCD if desired.

2.1 Semiconductors

An isolated atom has discrete electronic energy states. When two identical atoms are brought close together however these energy levels split due to the atomic interactions. In solids the close proximity of many atoms means that available electronic energy states form a continuum, or an energy band. Regions with no available states are termed bandgaps, and a given material contains numerous such energy bands and bandgaps. At a given temperature many of the bands are either completely filled with electrons or completely empty. Empty bands clearly cannot contribute to the electrical conductivity of a material since they contain no electrons. Full bands also do not contribute to the conductivity, since the electrons cannot gain energy due to all states being filled.

Partially filled energy bands contain both electrons and vacant electronic states, and so the electrons have high mobility and can contribute to the conductivity of the material. The important bands in determining the electrical properties of a material are therefore the valence band, which is the collection of the highest occupied electronic states for a system at zero Kelvin, and the conduction

band, which is the collection of the lowest vacant electronic states. The gap between these two bands is often termed the bandgap, due to its importance.

In a conductor there is no bandgap and so conduction band states are always occupied. Insulators have a very large bandgap compared to *kT*, where *k* is the Boltzmann constant. This means no conduction band states are occupied at finite temperatures. In semiconductors, the bandgap is sufficiently small that electrons can be promoted from the valence band to the conduction band. The bandgap for silicon is *~1.1 eV (*Grove, *1967).* The probability of occupation of an energy state of energy *E* by an electron is given by the Fermi-Dirac distribution function:

$$f(E) = \frac{1}{1 + e^{\frac{E - E_f}{kT}}} \qquad 2.1$$

Where E_f is the Fermi level, which is the highest occupied electron state at zero Kelvin. Figure 2.1 shows the function at both zero Kelvin and high temperature. At high enough temperatures there is a probability of conduction band states being occupied.

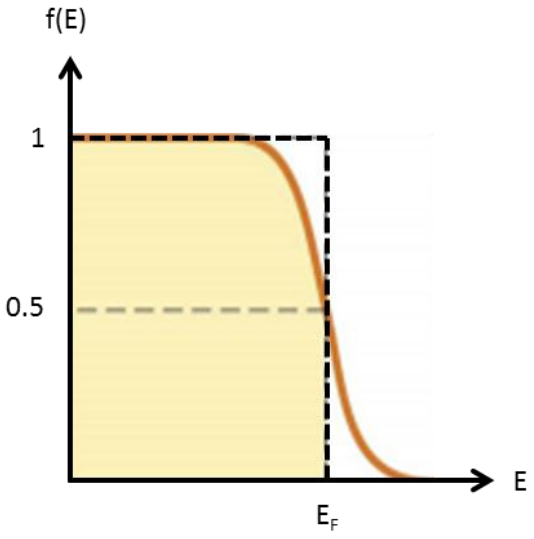

Figure 2.1 – The Fermi-Dirac function for a system at 0K (bold dashed line) and at high temperature (solid line).

The Fermi level controls the electrical properties of the semiconductor. By adding certain impurities to the silicon lattice, mid-bandgap states can be introduced to greatly enhance conductivity. The process of adding impurities to a semiconductor is known as doping. For the case of silicon, which is a group IV element with four outer valence electrons, adding dopants from groups V and VI with extra valence electrons donates an extra carrier to the conduction band. These are termed donor dopants and examples include phosphorous and arsenic. Donor dopants introduce states close to the conduction band edge and raise the Fermi level. The resulting material is known as n-type silicon. Adding group II and III elements such as boron or aluminium with one fewer valence electron introduces states close to the valence band edge and lowers the Fermi-level. Such dopants are known as acceptor dopants and the resulting material is p-type silicon.

2.1.1 - PN Junction

P-type and n-type silicon contain an excess of holes and free electrons respectively. These additional charges are countered by the now ionised dopant atoms, meaning that both n-type and p-type silicon remain electrically neutral and in equilibrium. If however a contact is made between the two different types of silicon in the presence of no external fields, then free carriers will flow across the junction and recombine with each other. The charged donor and acceptor ions are no longer balanced by the charge of the free carriers; this results in a build-up of negative charge within the p-type silicon and a build-up of positive charge in the n-type silicon. The resulting electric field acts to repel the diffusion of carriers across the junction and a new equilibrium state is reached. The region either side of the p-n junction which contains no carriers is called the “depletion region” since it has been depleted of free carriers. CCDs utilise depletion regions in order to separate out the electron-hole pairs produced by photon interaction in the silicon (Lutz, 1999). Figure 2.2 shows the p-n junction in its new equilibrium state and the resulting potential across the junction. The potential

step across the junction can be changed through altering the doping levels. This step is caused by the bending of the conduction and valence bands when the two pieces of silicon are bought together. The band bending occurs due to alignment of the two Fermi-levels.

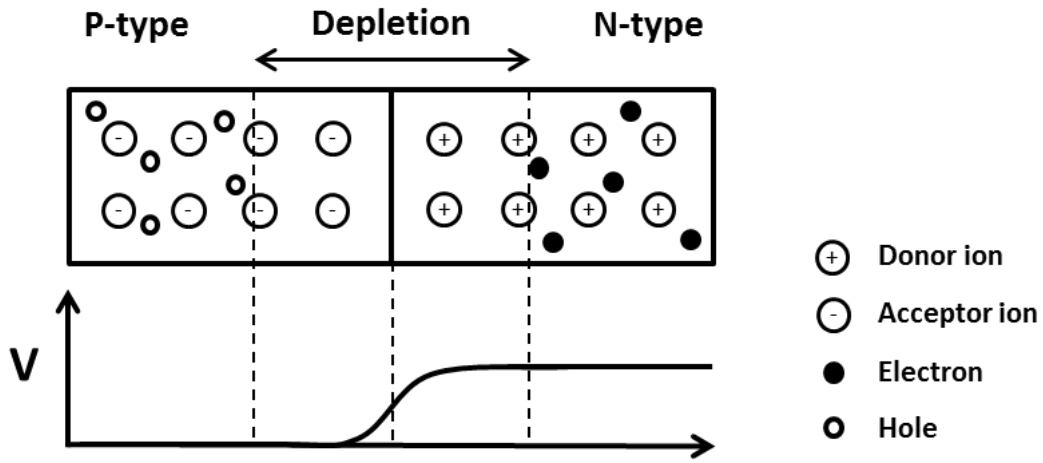

Figure 2.2 – Schematic of a PN junction, showing the formation of the depletion region and the potential step across the junction.

2.1.2 – Metal-Oxide-Semiconductor (MOS)

Metal-oxide-semiconductor (MOS) devices underpin much of modern technology. The basic principle is that the electrical properties of the semiconductor can be controlled by biasing the metal gate. With the gate bias *V* applied relative to the bulk potential then four distinct charge distributions are possible, as described below. The corresponding band structures are shown in Figure 2.3 for the case of a weakly p-type semiconductor.

Accumulation, (*V<0*) – A negative gate bias draws an excess of majority carriers (holes) to the region of semiconductor material near the oxide interface.

Flat-band (*V=0*) - With no gate bias there is no deformation of the bands and hence this condition is known as flat-band.

Depletion (*V>0*) – A positive gate bias acts to repel majority carriers (holes) from the semiconductor surface, forming a depletion region in which there exists a net negative charge due to the negatively charged acceptor ions. Therefore we have a spatially varying electrostatic potential which acts to bend the bands at the semiconductor surface (Grove 1967).

Inversion (*V>>0*) - Further increasing the gate bias widens the depletion region and the band bending effect until the conduction band begins to approach the Fermi level near the semiconductor surface. At this point the minority carrier (electron) concentration becomes significant and an inversion region is formed at the semiconductor surface.

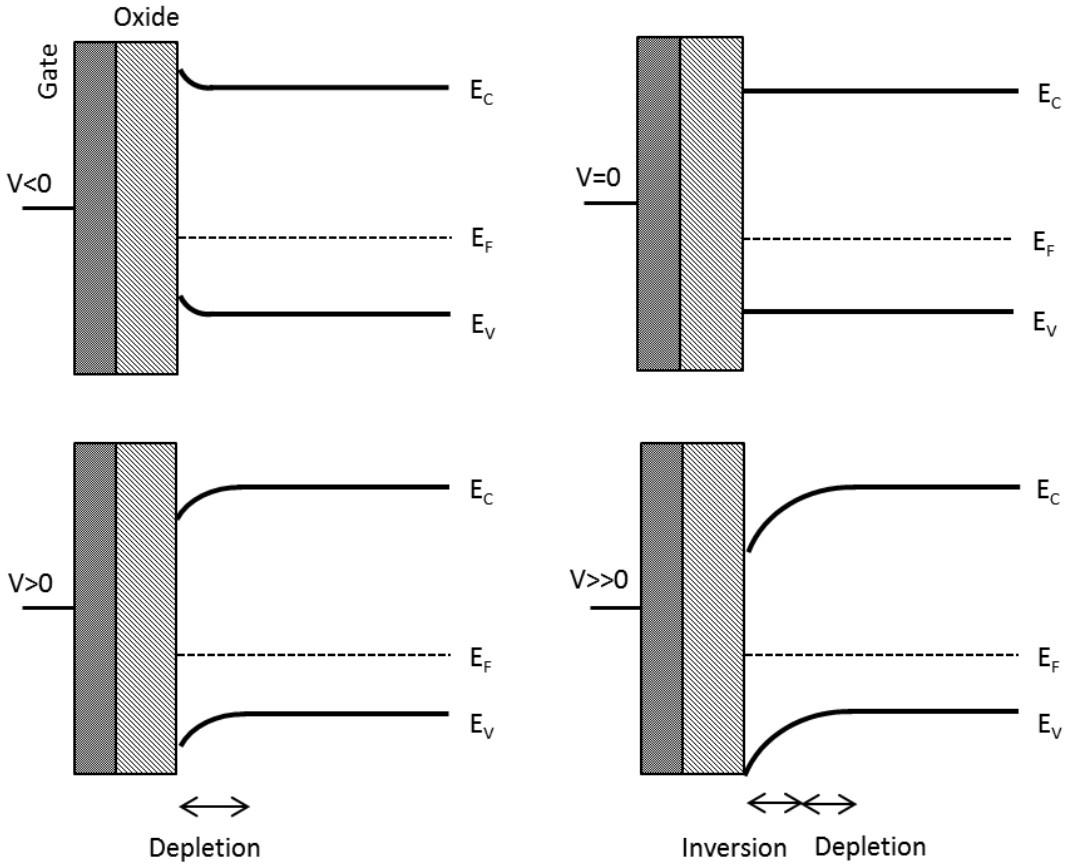

Figure 2.3 – Band structure for four different states of a p-type MOS capacitor: Accumulation (top-left), Flat-band (top-right), Depletions (bottom-left) and Inversion (bottom-right). Gate potential is denoted relative to bulk potential.

2.2 – Charge-Coupled Devices (CCDs)

Charge-Coupled Devices were invented at Bell Labs in 1969 by Boyle and Smith (Boyle, 1970) but were initially intended for use as a memory device. The potential for CCDs as position sensitive detectors was quickly realised and they have since become very popular as image sensor devices, with many industrial, medical and scientific applications. CCDs have wide dynamic range, high sensitivity and a good degree of linearity. A CCD is two-dimensional array of light sensitive silicon MOS capacitor "pixels". These are operated in deep-depletion, where the gate voltage is pulsed at a rate high enough such that an inversion layer cannot form, since the thermal generation of charge carriers is too slow. In this state the depletion layer width is increased beyond the maximum thermal equilibrium value, and inbound photons can excite electrons (or holes) into the conduction or valence bands respectively though the photoelectric effect. These charge carriers can then be controlled by electric fields through suitable biasing of the MOS capacitor gate electrodes. A single CCD pixel consists of 2 to 4 gate electrodes, with a scientific CCD typically of the order of a megapixel in size. Figure 2.4 shows a schematic of the structure of a typical 3-phase buried channel CCD pixel.

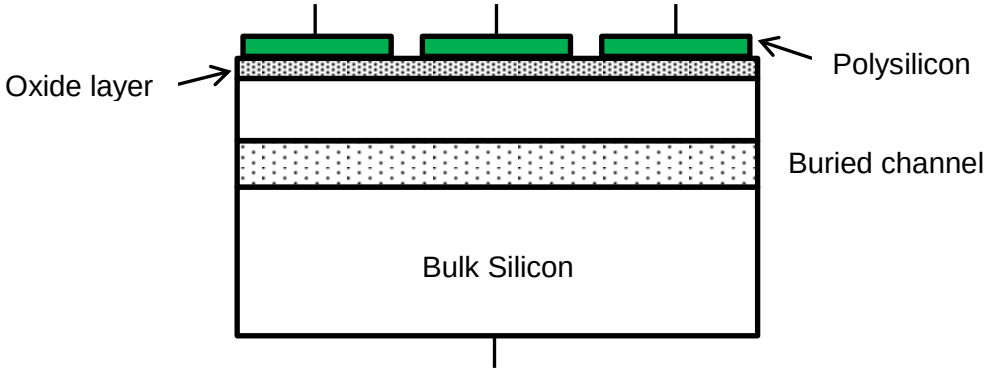

Figure 2.4 – Schematic of a 3-phase buried channel CCD pixel.

The first CCDs consisted of surface channel MOS capacitors (Boyle, 1970) such as in Figure 2.3 however these suffered from problems with charge trapping by interface states at the semiconductor/oxide boundary. A solution was the use of a buried channel MOS capacitor (Walden, 1972). Buried channel CCDs utilise a narrow region of silicon which is doped with the opposite type impurities to the rest of the substrate. This creates a potential well for charge carriers which remains separated from the oxide interface. Two variants of CCDs are therefore possible; n-channel CCDs utilising a buried channel of n-type silicon on a p-type substrate, and p-channel CCDs using a p-type channel on an n-type substrate. Both n- and p-channel devices are studied within this work, and the differences between the two will be discussed later.

The MOS gate electrode structures extend across the entire width of the CCD. Pixel columns are defined by channel stops; regions of high doping which create a potential barrier confining charge carriers to the pixel boundary. Carriers are then moved through the device by suitable biasing of the gate electrodes, creating regions of electric potential within the buried channel. Multiple parallel registers are used across the active image area of the CCD, which can be clocked simultaneously. Each parallel transfer moves one row into a serial output register, which is then clocked pixel-by-pixel onto an output node. Figure 2.5 outlines the typical CCD clocking process.

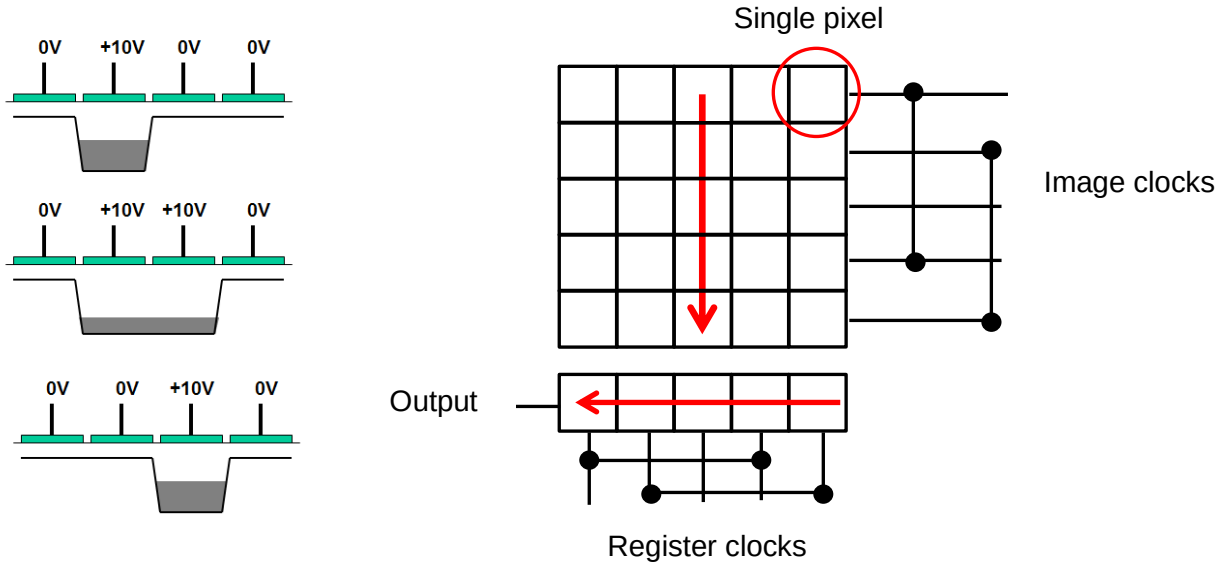

Figure 2.5 – Schematics showing the transfer of charge through gate biasing (LHS) and the overall clocking process (RHS).

2.2.1 – Charge generation and collection in a CCD

A CCD is defined by its ability to generate, store and transfer charge efficiently. In each of these areas there are a number of key measures for defining the CCD performance. These are in addition to the noise characteristics, which are discussed in the following subsection.

Regarding charge generation, the Quantum Efficiency (QE) of a CCD is defined as the ratio of incoming photons to generated signal electrons (or holes). Typically CCDs are illuminated through the polysilicon electrodes, which are semi-transparent but still absorb some of the incoming photons. To improve QE CCDs can be backside illuminated, which requires thinning of the device through chemical etching (Holland, 2003). CCDs exhibit high QE in relation to other image sensor types since the photosensitive area is not covered by other material. A thinned backside illuminated CCD can give a QE as high as *70-90%* across the visible spectrum (Holland, 2003). Typical QE values for a CMOS image sensor are around *40%* (Fowler, 1998).

With respect to charge collection in a CCD an important parameter is the full-well capacity (FWC) which defines the number of signal charges which can be held by the electric potential within a given pixel. If the CCD is exposed to too much light it will become saturated and charge carriers will “spill” out of a pixel into neighbouring pixels. This effect is known as blooming. Another important parameter for charge collection is the pixel uniformity, which describes the uniformity of the response of each pixel to light (Janesick, 2001).

2.2.2 – Charge transfer in a CCD

Once charge has been collected it must be transferred through the device to the output node. There are three main charge transfer mechanisms within a CCD: thermal diffusion, self-induced drift and Fringing-Field (FF) effects (Banghart, 1991). Thermal diffusion describes the temperature dependent movement of charge carriers within a lattice where there exists a concentration gradient. Diffusion is a slow process which is field independent, and so it defines the limiting transfer rate. Self-induced drift describes the effect of the electric field due to a signal charge packet on the individual charges within the packet, and is the dominant transfer mechanism for all but low signal levels. Fringing fields (FFs) are electric fields caused by the different electric potential of each clock electrode. Fringing field drift is a fast process compared to the other two transfer mechanisms; however FF drift is dependent on signal level and clock voltages, and falls to zero once the pixel reaches full-well capacity (Banghart, 1991).

The charge transfer performance of a CCD is defined by its charge transfer efficiency (CTE), which is defined as the fraction of carriers which are successfully moved from one pixel to the next per transfer (Janesick, 2001). Often the charge transfer inefficiency is instead referenced, which is simply defined as:

$$CTI=1-CTE \quad (2.2)$$

CTI occurs due to the trapping of signal charge. This can be due to erroneous potential wells/barriers present from the fabrication process, trapping at interface states or trapping by lattice defects within the buried channel. Typically scientific grade CCDs can be produced with a CTI of around 1×10^{-5}, meaning transfer is highly efficient. However if a device is subjected to radiation damage the formation of defect states in the bulk silicon can increase CTI. The focus of this thesis is the analysis of several prominent radiation induced defects, which are a significant source of CTI in both damaged n-channel and p-channel CCDs.

There are several possible methods for measuring CTE. The standard process for defining CTE is X-ray transfer, where an X-ray photon of a given energy will produce a known amount of signal charge within a pixel. The signal level can be then tracked across a number of trailing pixels following transfer (Janesick, 2001). Plotting the number of pixel transfers against the signal remaining in the n^{th} pixel gives a straight line from which CTE can be deduced. The drawback of this method is that with very large values of CTE or a very large number of pixel transfers the gradient of the line becomes difficult to define and so the CTE measurement becomes imprecise. Other measurement techniques exist which involve similar principles of producing a known signal level within a pixel and tracking it across a certain number of transfers, measuring the amount of deferred charge. Examples include the extended pixel edge response (EPER) and first pixel response (FPR) techniques

2.2.3 – CCD Output

The typical CCD output circuit consists of an output node capacitance providing the input for a source-follower amplifier. Typically this node capacitance is floating, such that the voltage across it is dependent only on its capacitance and the charge present on its plates. Signal charge carriers can be therefore be deposited on one of the capacitor plates to cause a voltage drop across it, according to

the capacitance equation *V=Q/C*. Between each pixel transfer a reset transistor sets the voltage across the node capacitance to a reference level. Once charge from a pixel is deposited onto the capacitor plates, the voltage drop is sensed by the output amplifier and sent off-chip to the Analogue to Digital Converter (ADC), in order to obtain a value for the signal level of that pixel. The responsivity of the output circuit is defined as the change in voltage caused by the addition of a single charge carrier onto the output node capacitor. The gain of the CCD is then defined as the ratio between the number of charge carriers in a pixel and the recorded "counts" in Digital Numbers (DN) for that pixel. Figure 2.6 shows a schematic of a typical CCD output circuit.

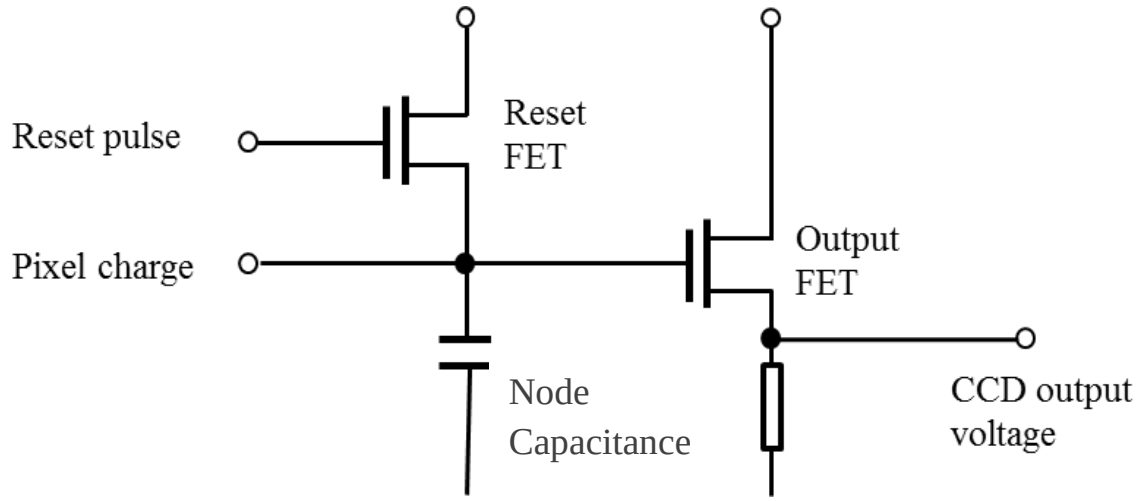

Figure 2.6 – Circuit diagram for a typical CCD output circuit.

2.3 – CCD noise sources

As with all detectors, CCDs suffer from various sources of noise both during charge generation (shot noise, dark current) and readout (reset noise, read noise) which affect the device sensitivity and image quality. The major sources of noise are discussed below along with commonly used methods to reduce them to tolerable levels.

2.3.1 – Dark current

Thermal generation of charge carriers is inherent in any semiconductor material. These carriers are indistinguishable from optically generated carriers and so are collected in the same way. Dark current generation is higher at the semiconductor surface than in the bulk due to the presence of interface traps, which can act as intermediate states for the promotion of a carrier into the conduction band. Dark current increases linearly with temperature and so it is possible to significantly reduce its impact by cooling the CCD. For this reason many scientific CCDs are operated at temperatures well below room-temperature. A large reduction in dark current can also be obtained by operating a CCD in an inverted mode, where one or more gate electrodes are inverted during image integration. This causes holes (in an n-channel device) to migrate from the channel stop regions to fill the interface states, reducing the probability of thermal generation into the conduction band.

Dark current adds noise to measurements in a CCD because of dark signal non-uniformity (DSNU) which is non-uniformity in the pixel response to thermal generation of carriers. Some pixels can exhibit particularly high levels of dark current and are referred to as “hot” pixels. In general DSNU is a greater issue for CCD imagers than dark-current alone, since dark-current can be effectively supressed through cooling or inverted mode operation (Hopkinson, 1996).

2.3.2 – Shot noise

The arrival of photons at a detector is a random process and so exhibits a Poisson noise. This is called shot noise and as can be seen from Equation 2.3 is most problematic for low signal level applications, where *s* is the signal level. It can be reduced through the use of longer exposures or through combining many exposures. Each CCD pixel also has a slightly different sensitivity to light, even in the case of high grade scientific CCDs. This is known as pixel response non-uniformity (PRNU) and can be removed through the subtraction of a flat-field exposure.

$$\sigma_{shot} = \sqrt{s} \tag{2.3}$$

2.3.3 – Reset noise and CDS

As stated previously, the signal level in a given pixel is measured by the voltage drop across the output node capacitor. In between each pixel measurement a reset transistor sets the voltage across the capacitor to a reference level. However, this reference level is not always set to the exact same value, since there is channel resistance in the reset transistor. There is therefore a thermal noise on the reset level, given in units of electrons by Equation 2.4 where *k* is the Boltzmann constant, *T* is the CCD temperature in kelvin, *C* is the output node capacitance and *q* is the unit electric charge. For reliable CCD performance the reset noise must be suppressed through the use of correlated doubling sampling (CDS). CDS involves sampling the output twice per pixel, once after the reset pulse and once after charge has been deposited onto the capacitor. This accounts for any variation in the reset level since only the difference between the two measured voltages is important. Figure 2.7 shows a simplified version of typical CCD output waveform, with CDS sampling points.

$$\sigma_{reset} = \frac{\sqrt{kTC}}{q} \tag{2.4}$$

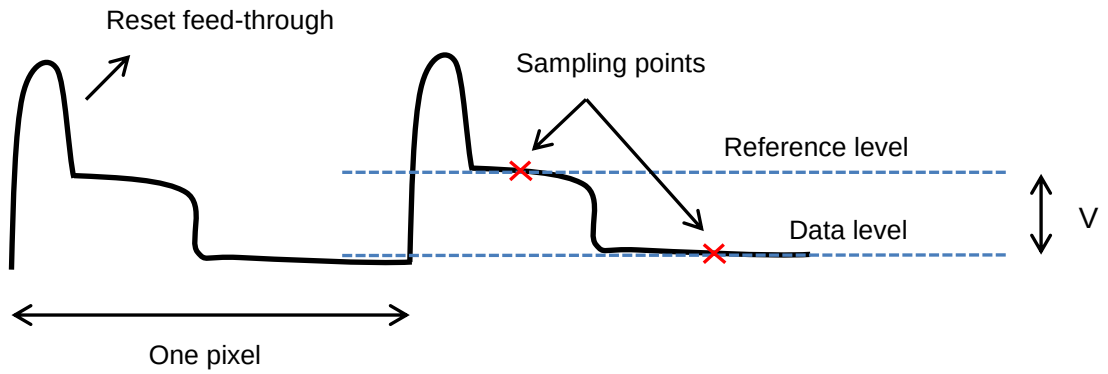

Figure 2.7 – Simplified diagram of a typical CCD output waveform, showing the two measurement points for the CDS technique.

2.3.4 – Read noise

A CCD using CDS is ultimately limited by the read noise floor. The read noise comes from two primary sources; white (Johnson) noise due to the resistance of the output amplifier circuit and flicker (1/f) noise due to traps at the Si/SiO_2 interface. The noise response is typically limited by 1/f for low frequency readout (<100kHz) and by the white noise for higher frequency readout, since this is proportional to the bandwidth. Read-noise can be reduced through standard image processing techniques such as combining frames.

2.4 – N-channel and P-channel CCD variants

As discussed earlier in this Chapter, the addition of a small amount of non-native atoms to a semiconductor material can cause significant changes to its electrical properties. This process is known as doping and leads to n-type (e.g. phosphorous doping) and p-type (e.g. boron doping) semiconductor materials. There are therefore two possible CCD variants; n-channel CCDs which use an n-type silicon buried channel on a p-type silicon substrate and p-channel CCDs which use a p-type channel on an n-type substrate. In n-type silicon electrons are the majority carrier and so constitute

the signal charge in an n-channel CCD. For the case of p-channel CCDs holes constitute the signal charge. Currently the n-channel CCD is the standard for the large majority of applications, however an increasing amount of work is going into the development of p-channel CCDs. With respect to radiation damage and the work in this thesis p-channel CCDs are thought to have to potential for greater radiation tolerance. This is discussed in more detail in Chapter 3.

Chapter 3 – The radiation environment in space and impact on CCDs

The previous Chapter introduced the CCD image sensor and discussed some of its advantages including high sensitivity and excellent charge transfer performance. However if a CCD is used in a harsh radiation environment performance can be degraded in numerous ways. The deep-level defects which are the focus of this work are one such symptom of radiation damage. Presented here is a brief discussion to the space radiation environment in which CCDs are commonly employed, an outline of some of the more general radiation damage effects and a more in-depth review of the stable deep-level defects which will be studied in later Chapters.

3.1 – Radiation environment & shielding

Radiation can exist in the form of photons (γ), charged particles (e, p) and uncharged particles (n). The predominant damage mechanism depends on both particle type and energy. Photons are the source of signal in a CCD through their interaction with the silicon via the photoelectric effect, however they can also interact at higher energies through Compton scattering or pair-production (Srour, 2003). Photons do not damage the CCD lattice directly but through secondary electrons which are excited into conduction band states and behave in the same way as impinging electrons. Neutral particles refer in the case of CCDs to neutron damage. Since they do not carry charge neutrons do not interact via the Coulomb force and so only through elastic collisions with lattice atoms. Because of this they can cause significant displacement damage and lead to the formation of defect clusters due to the large number of recoil atoms (Lindstrom, 2003).

Charged particles can interact with the lattice in two ways; elastically through Rutherford scattering and also through inelastic collisions with silicon nuclei. Lighter particles such as electrons generally displace single atoms whilst heavier particles and ions can create large numbers of recoil atoms (Srour, 2003).

The radiation environment for space imaging missions consists of galactic cosmic rays, the solar wind and trapped radiation in the Van Allen belts. These consist of mostly protons and electrons, covering a wide range of energies. It is possible to eliminate the impact of radiation through shielding, however since mass is at a premium for space missions the design aim is to reduce damage to acceptable levels over the mission lifetime. The stopping range of a particle is dependent on the particle energy and shielding material, therefore the specific radiation environment of each mission is modelled individually through the use of programs such as SPENVIS (Gow, 2012). A major concern is the secondary particles released from any shielding material by high energy incident particles. These can represent a significant portion of the total overall dose. Using a lower Z material for shielding has been shown to reduce the effects of secondary particles (Zeynali, 2012) since the number of secondaries scales with Z^2.

3.2 – Radiation damage mechanisms

Radiation damage effects can be classified as either transient or permanent. Transient effects such as ionization tracks can affect a single to several exposures and must be accounted for, however they are not relevant to the work in this thesis. Permanent effects however lead to potentially irreversible performance degradation and can shorten the effective lifetime of a detector. Permanent damage effects can be further classified into surface damage effects due to total ionizing dose, and bulk damage effects due to displacement damage in the silicon lattice.

3.2.1 – Surface damage

Ionizing radiation creates electron-hole pairs in the silicon dioxide of a MOS capacitor (Hopkinson, 1991). The electrons have high mobility and are quickly swept by the electric field to the positively charged gate electrode. However the holes are much less mobile, and some become trapped by oxide traps close to the Si/SiO_2 boundary. These trapped holes affect the performance of the MOS

device in the same way as applying a gate bias of equal magnitude; i.e. there is an induced threshold-voltage shift. In CCDs this is referred to as the flat-band voltage shift. The voltage shift is dependent on the oxide layer thickness, and so often devices are produced with thinned oxide layers to increase radiation hardness.

A second effect of ionizing radiation is to increase the density of defects at the Si/SiO_2 boundary. Defects appear at this boundary during CCD manufacture due to the presence of "dangling bonds", which are incomplete bonds at the interface. Ionization damage can both increase defect density and alter the energy distribution of interface defects. The predominant effect of this in a CCD is a large increase in surface dark current, which much be supressed through cooling or through inverted mode operation. The increased density of interface traps can also lead to a reduction in the FWC of a CCD (Hopkinson 1991).

3.2.2 – Bulk damage

As a particle passes through the lattice it may impart some or all of its energy to a silicon atom through elastic or inelastic collisions. The resulting unoccupied lattice site is referred to as a vacancy defect whilst the displaced silicon atom is a self-interstitial defect. Together the two defects constitute a Frenkel pair (Kittel, 1996). The minimum energy required to release an atom from the lattice is approximately *25 eV* (Lindstrom, 2003).

Higher energy particles will impart a large amount of energy to the initially displaced atom, the "primary knock-on atom" (PKA), as kinetic energy (the Recoil energy E_R). The PKA can then displace further atoms, leading in cases of high energy radiation to large clusters of Frenkel pair defects. Most of the self-interstitial and vacancy defects will recombine with each other over very short timescales. The remaining vacancy defects are mobile even at temperatures down to a few Kelvin (Watkins, 2000) and can diffuse through the lattice to form stable defect complexes with other vacancies, impurity atoms or dopant atoms. The resulting defects are the focus of this work and the next

section is dedicated to their discussion in greater detail.

3.2.3 – Non-ionizing energy loss (NIEL)

The NIEL scaling hypothesis states that damage produced in the bulk is proportional to a displacement damage cross-section *D*, which is the non-ionizing energy loss in the detector (Lindstrom, 2003):

$$D(E) = \sum_{v} \sigma_v(E) \times \int_0^{E_R^{max}} f_v(E, E_R) P(E_R) dE_R \qquad 3.1$$

Where σ_v is the cross-section for a specific interaction *v* and all possible interactions are summed over. f_v is the probability for the creation of a PKA with recoil energy E_R by an impinging atom of energy *E*. All possible recoil energies of the PKA are integrated over. $P(E_R)$ is the Lindhard partition function which describes the fraction of recoil energy which is deposited as displacement damage (Lazo, 1987). The NIEL hypothesis allows for the scaling of damage from different particle types, by normalizing to the damage caused by a 1MeV neutron. The actual particle energy spectrum can then be replaced by a NIEL spectrum. Figure 3.1 shows the NIEL for common particle types in silicon (Lindstrom, 2003). For charged particles NIEL is due mostly to the Coulomb interaction between the particle and the silicon atom nucleus. Neutrons interact via elastic scattering with the nucleus.

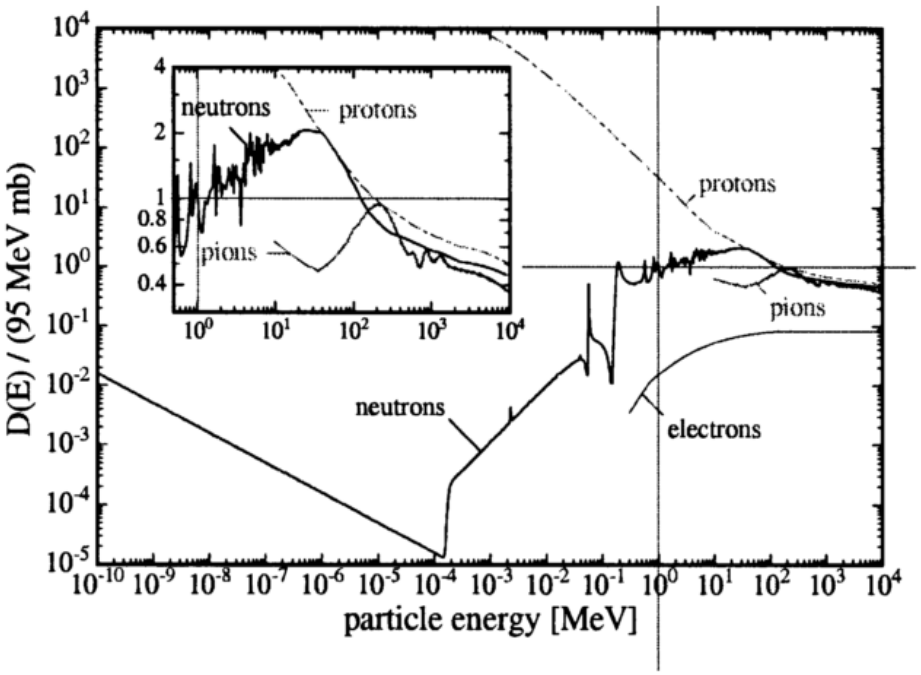

Figure 3.1 – Non-ionizing energy loss for different particle types and energies in silicon (Lindstrom, 2003)

3.3 – Displacement damage effects

As outlined earlier, with enough energy it is possible for an impinging radiation particle to displace a silicon atom (the PKA) from its lattice site. The threshold energy to remove a silicon atom is approximately *25 eV* which is equivalent to an electron of energy *260 KeV* (Lindstrom, 2003). The atom and the resulting vacant site are both mobile and can interact to form stable point defects which can be electrically active and create states within the bandgap. A point defect is classified as one which affects only its nearest neighbour atoms. Higher order defects such as column defects are also possible but beyond the scope of this work. A simple schematic of the different types of point defect is shown in Figure 3.2 which was adapted from Pichler, (2004).

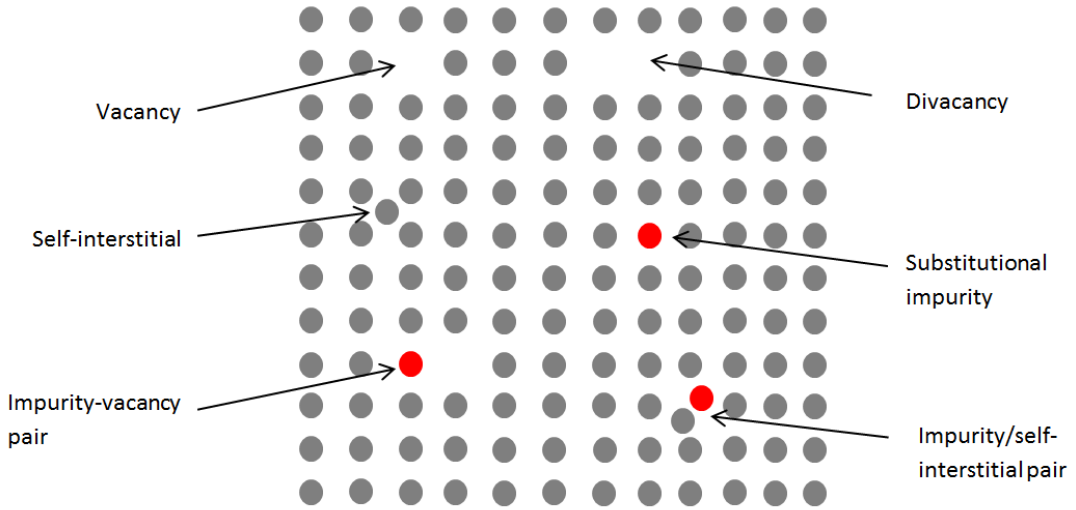

Figure 3.2 – A schematic of the various possible types of point defect in a crystal lattice. Grey circles represent native (silicon) atoms and red circles represent any impurity atom. Adapted from Pichler (2004).

Excess energy above the threshold energy may be imparted on the PKA as the recoil energy E_R. The PKA may then displace secondary atoms from their lattice sites. For E_R above ~*5 KeV* dense regions of secondary atoms and vacancies can form at the end of the PKA trail and lead to the formation of defect clusters (Srour, 2003). Both primary point defects and clusters can degrade detector performance however the focus of this thesis is the analysis of several point defects in a CCD.

The initial displacement of an atom results in the creation of what is known as a "Frenkel pair" defect consisting of the displaced atom as a silicon self-interstitial defect and the lattice vacancy. These two intrinsic defects are the initial constituents of all of the many complex defect structures which can be formed. Many Frenkel pair defects recombine with each other over very short timescales immediately after being produced (Watkins, 2000); however the self-interstitials and vacancies each have different mobility within silicon and so depending on the temperature and other conditions a significant proportion can diffuse away through the lattice to form more complex and stable defect centres. Many of these defect centres introduce deep level states into the bandgap which can greatly affect the characteristics of a semiconductor device.

3.3.1 – Deep-levels

It is important to first distinguish between the radiation-induced deep-levels within the bandgap and the shallow levels produced through the doping of a semiconductor as discussed in the previous Chapter. The term shallow simply refers to shallow within the gap; meaning close to either the conduction or valence band edge. Energy levels added through doping of a semiconductor with donor or acceptor impurities are shallow levels and act to add or remove electrons from the conduction band respectively. Deep-levels can be introduced into the bandgap by radiation-induced point defects and can act as trapping centres for free carriers. All of the defect levels which are studied in this thesis are deep-levels.

Shallow levels are short-range screened Coulomb potential levels which are de-localised in real space and so highly localised in phase-space. Deep-levels are long range central cell potential levels and are highly localized in real space (Balkanski, 2000). As is seen for example in the case of the lattice vacancy it is possible for a single defect species to have numerous deep level charge states which are associated with different localized states of the same wave function. In an extrinsic (doped) semiconductor the movement of the Fermi level away from the centre of the bandgap creates favourable conditions for the production of charged defects. Deep-level states can affect semiconductor performance through the exchange of electrons and holes between themselves and the conduction and valence bands. As well as their energies within the bandgap deep-levels are characterised by their capture cross-sections for majority and minority carriers. Many prominent defect analysis techniques are designed to analyse these parameters. However, in CCDs and other image sensors the parameter of primary importance is the emission time constant of the defect level, which defines the length of time for which a level will hold a carrier after capture before releasing it again. It is this time constant which, depending on the operating conditions of a detector, will govern how much of a concern a deep level is for performance. It is for this reason that the work

in this thesis aims to directly probe defect time constants; with the energy levels and cross-sections subsequently estimated through calculation. The motivation for this and the methodology is discussed fully in Chapter 4.

When characterising deep-level states they are referred to as “donor” or “acceptor” levels. It is important to distinguish between this and for the case of shallow levels arising from donor or acceptor impurities. A deep-level is classed as a donor level if it is electrically neutral when it is occupied by a charge carrier and electrically negative otherwise. This means that donor deep-levels act as hole traps in a semiconductor, making them of importance in p-channel CCDs. A level is classed as an acceptor level if it is neutral when unoccupied and negatively charged when occupied. Therefore they act as electron traps and are important in n-channel CCDs. Donor levels are described by their energy above the valence band edge and acceptor levels by their energy below the conduction band edge. In either case a higher energy value means the level lies deeper within the bandgap and more energy is required for capture or emission processes to take place, resulting in defect levels with longer emission time constants. It is possible for certain defect levels to be donor and acceptor-like, these are known as amphoteric levels (Pichler, 2004).

3.3.2 – Lattice Effects at a Defect Centre

The introduction of any defect to a crystal lattice can involve an abrupt change in the crystal potential. In the immediate vicinity of the defect the valence wave-functions of the host atoms may be substantially modified. If the impurity potential is weak then these changes can be treated as a perturbation of the system, however this is not always the case.

The defect potential affects the crystal interactions with valence electrons, resulting in a new electron distribution in the defect vicinity. This can substantially alter the lattice stability around the defect site, and surrounding atoms may be displaced from their host sites. This effect of reduced

lattice stability around a defect is termed the lattice relaxation. Lattice relaxation lowers the total energy of the system. The driving force for lattice distortion is often the Jahn-Teller effect, and this is always the case for vacancy related defects. The Jahn-Teller effect occurs because the electronic state is degenerate. Atomic displacements in the defect vicinity lower the symmetry and split the degenerate level (O'Brien, 1993). If there was no lattice relaxation around a defect potential then the difference in energy between different charge states of the same defect species would simply be the extra energy required to overcome the repelling Coulomb force from each additional charge carrier added to the level. However the lattice relaxation alters this greatly and in some cases can be large enough to cause an inversion of the charge state energies entirely, effectively giving a net attractive force between two equal charge carriers. This case is known as "negative-U" because of the negative correlation energy for the charge carriers. One such case of negative-U defect behaviour is the first and second donor states of the single vacancy defect (Baraff, 1980; Watkins, 1980). The energies of the two vacancy levels are shown in Figure 3.3. The double donor level lies deeper in the bandgap at $E_v + 0.13\ eV$ than the single donor level at $E_v + 0.05\ eV$, meaning that the second hole is bound more tightly than the first. Without the lattice relaxation effects, this would not be expected due to the Coulomb repulsion between the like charges.

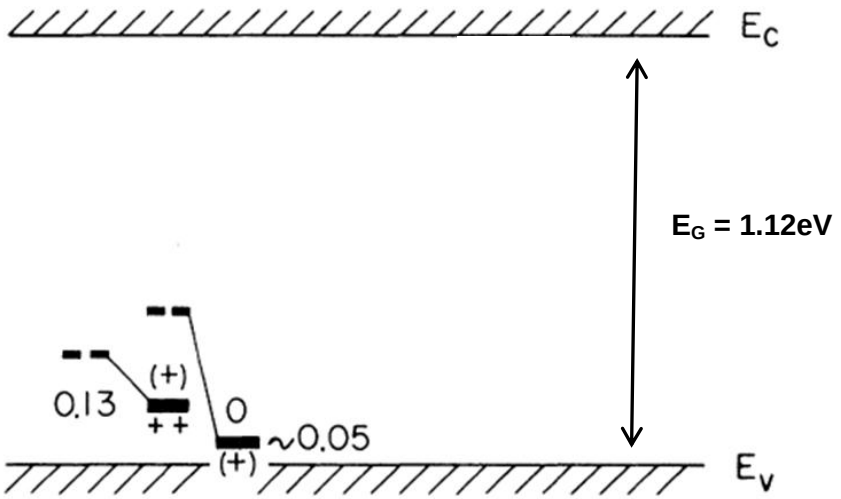

Figure 3.3 – The positioning of the single and double donor levels of the single silicon vacancy within the bandgap, showing the "negative-U" behaviour (Watkins, 1980).

3.4 – Intrinsic point defects

Intrinsic defects are those which consist of only native (silicon) atoms and lattice vacancies. They are the constituents of all other more complex defect structures and so a good understanding of their properties is important for any further analysis of the radiation damage process.

3.4.1 – The single lattice vacancy

The single lattice vacancy can take on five different charge states, resulting in four levels within the bandgap; a single donor level, a double donor level, a single acceptor level and a double acceptor level. There is a large lattice relaxation effect as the broken bonds reconstruct, with the strength of the reconstructions increasing as the defect acquires further electrons. This results in the lowering of the levels within the bandgap and also gives rise to the "negative-U" property of the donor levels as discussed in section 3.32. The existence of the different charge states affects not only the lattice reconstruction but also the subsequent movement of the vacancy and its interaction with other

defects. Single vacancies are highly mobile, with activation energies for diffusion of approximately *0.20 eV* and *0.30 eV* in n-type and p-type silicon respectively (Watkins, 2000). They are observed to completely anneal away at temperatures of ~70K and ~150K in n-type and p-type silicon respectively (Watkins, 2000).

3.4.2 – The silicon self-interstitial

Isolated self-interstitials are very difficult to produce in such a way as they can be studied, and so much of the knowledge of this defect comes from the analysis of interstitials trapped at other defect sites. It is known however that the self-interstitial is a very highly mobile defect, with diffusion observed in p-type silicon at even a few Kelvin (Auret, 2004). It is believed that the self-interstitial has three charge states corresponding to two levels within the bandgap; a single donor level and a donor level. Strong "negative-U" behaviour is expected for the two levels (Watkins, 2000). Theoretical calculations show that each charge state should be most stable in a different configuration, such that the capture and release of carriers can provide a mechanism for diffusion (Watkins, 2000).

3.4.3 – The silicon divacancy

The unperturbed silicon divacancy can be simply viewed as two vacant, nearest neighbour lattice sites. It is a fundamental defect in silicon and therefore has been studied extensively using a wide range of techniques. The divacancy can be formed as a primary defect if an impinging particle removes two adjacent silicon atoms from the lattice, or by two single vacancies combining. This results in six dangling bonds which induce two degenerate one-electron levels in the bandgap (Watkins, 1965). Following lattice re-orientation the stable defect can be formed. A schematic view of the silicon divacancy is shown in Figure 3.4 (Iwata, 2008). Analysis of the radiation dose-rate

dependence of silicon divacancy production has also suggested that the two single vacancies must have originated from the same impinging particle (Svensson, 1992).

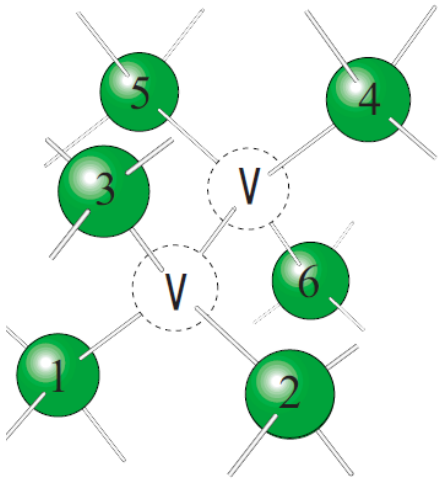

Figure 3.4 – A schematic of the structure of the silicon divacancy (Iwata, 2008):

The silicon divacancy has a binding energy of ~*2 eV* and can exist in four possible charge states; a singly positive state (V_2^+), a neutral state (V_2^0), a singly negative state (V_2^-) and a doubly acceptor level (V_2^{--}). This gives rise to three energy levels in the band gap; a single donor level ($V_2^{0/+}$), a single acceptor level ($V_2^{-/0}$), and a double acceptor level ($V_2^{--/-}$). The silicon divacancy is therefore an amphoteric defect; meaning that it introduces both acceptor and donor levels into the bandgap. This makes it an important defect in both n-channel and p-channel CCDs over a wide range of operating conditions. Extensive Deep-level transient spectroscopy (DLTS) studies have found the energies of the three levels to be at approximately $(E_v + 0.19)\ eV$, $(E_c - 0.23)\ eV$ and $(E_c - 0.41)\ eV$ respectively (Kimerling, 1977; Huppi, 1990; Hallen, 1996; Eremin, 1999; Evans-Freeman, 2000; Zangenberg, 2002; Auret, 2004; Nyamhere, 2006). There is much less consensus regarding the capture cross-section for each level, but values of $(2.0 \times 10^{-16})\ cm^2$, $(4.0 \times 10^{15})\ cm^2$ and $(2.0 \times 10^{-16})\ cm^2$ respectively were obtained by Kimerling (Kimerling, 1977) and further work since has obtained similar values (Huppi,

1990; Eremin, 1999; Fretwurst, 2000; Zangenberg, 2002; Auret, 2004). Figure 3.5 shows the positioning of the three divacancy levels within the bandgap.

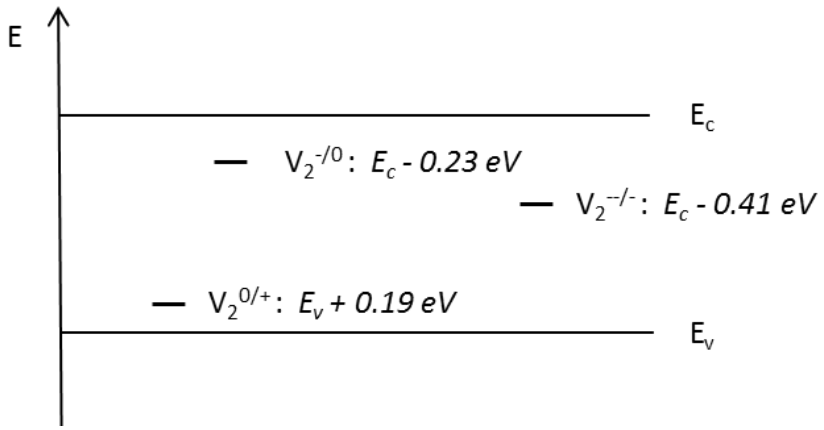

Figure 3.5 – The positioning of the three levels of the silicon divacancy within the bandgap. The divacancy is stable in four charge states resulting in a single donor level, a single acceptor level and a double acceptor level. The notation for a defect level is given by its charge state when occupied/unoccupied.

Along with the silicon-phosphorous defect (E-centre, see discussion later in this Chapter) the divacancy is the predominant radiation induced defect in phosphorous doped n-type silicon. The acceptor levels are therefore very important when concerned with charge transfer performance in n-type silicon. In p-type silicon the divacancy is also a predominant defect along with carbon related defects, and so the donor level is of importance when considering charge transfer performance.

The first major study of the divacancy in silicon was conducted by Watkins in 1965. Using Electron Paramagnetic Resonance (EPR) experiments with samples under various stresses it was shown that the divacancy can re-orient its vacancy-vacancy axis, at which point it is diffusing through the lattice. Watkins estimated an activation energy for this process of *1.3 eV* and it has since been established that the activation energy for divacancy diffusion is *1.25 eV* (Watkins, 1965). Divacancies anneal by diffusion through the lattice until they are captured by another defect complex. The binding energy

of *2 eV* stated above represents the energy required for the dissociation of the divacancy into two single vacancies. The relatively large difference between the activation energy for diffusion and dissociation means that divacancies can travel large distances through a lattice without dissociating. The temperature at which divacancies begin to anneal is around 550K (Pichler, 2004) and therefore they are a highly stable defect at room temperature, which has allowed such extensive studies to be carried out.

3.5 –Extrinsic Point Defects

Epitaxial silicon contains high concentrations of impurities such as oxygen and carbon. The single lattice vacancies and self-interstitials created by impinging particles are highly mobile and will move through the lattice, often forming stable point defects with dopant or impurity atoms. With respect to charge transfer in CCDs the predominant defects of importance are the vacancy-oxygen defect, the vacancy-phosphorous defect and defects related to carbon.

3.5.1 – The vacancy-oxygen defect

The vacancy-oxygen defect (A-centre) is formed when a mobile single vacancy is trapped by an interstitial oxygen impurity. Oxygen is present throughout the silicon lattice in high concentrations as a remnant of the production process. As a single impurity interstitial it is inert however it is a highly efficient vacancy trapping site with the oxygen atom able to bridge a pair of silicon atoms which neighbour the vacancy, as shown in Figure 3.6 (Watkins, 1961). The formation of an A-centre allows for the migration of the usually immobile oxygen interstitial at room temperature.

The A-centre has two stable charge states; a neutral state and a singly negative state. This results in a single deep acceptor level, with an energy level which is reported as approximately $(E_c - 0.17)\ eV$ (Kimerling, 1975; Hallen, 1996; Eremin, 1999). The relatively close proximity of the level to the

conduction band edge results in a smaller emission time constant; this makes the A-centre of particular importance in n-channel CCDs when operating with high read-out frequencies or at very low temperatures, since defect emission time constants increase with decreasing temperature (see later discussion in this Chapter). It is possible for the defect to diffuse through the lattice and interact with other vacancies or vacancy-oxygen pairs to produce higher order defect complexes. The A-centre anneals away completely at approximately *650K* (Watkins, 2000).

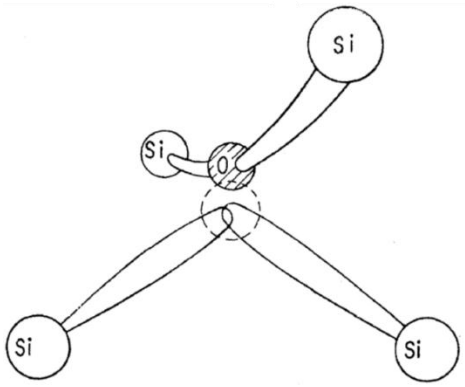

Figure 3.6 – A schematic of the structure of the silicon A-centre (Watkins, 1961).

3.5.2 – The vacancy-phosphorous defect

The silicon E-centre consists of a vacancy paired with a group-V substitutional impurity. In CCDs the E-centre of relevance is the vacancy-phosphorous pair. The phosphorous atom does not form any bonds due to the four dangling bonds created by the vacancy, since it has two paired electrons in its broken orbital. Instead two of the neighbouring silicon atoms form an electron-pair bond, leaving an unpaired electron in the orbital of the final silicon atom (Watkins, 1964). A schematic of the E-centre structure is shown in Figure 3.7.

The E-centre is stable in a neutral state and a singly negative state; corresponding a single acceptor level with energy *(E_c – 0.45) eV.* The close positioning of the level to the bandgap centre results in a

defect with a large emission time constant compared to the other predominant defects, making the E-centre of particular importance in n-channel CCDs when operating at slow read-out frequencies or high temperatures. As in the case of the A-centre the E-centre is mobile and can form higher order defects with other vacancies or phosphorous atoms. It anneals away completely at approximately *200K*.

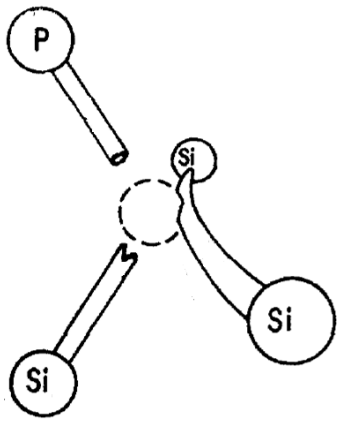

Figure 3.7 – A schematic of the structure of the silicon E-centre defect (Watkins, 1964).

3.5.3 – Carbon-related defects

Just as oxygen and group-V atoms represent efficient trapping sites for vacancies, carbon is a very effective trap for self-interstitial defects, and is present in any silicon material in concentrations as high as $10^{15}cm^{-3}$ (Newman, 1982). A substitutional carbon impurity can be removed by a silicon self-interstitial via the Watkins replacement mechanism (Watkins, 1964). The self-interstitial then occupies the lattice site as a native atom, leaving the displaced carbon atom as a highly mobile interstitial defect. The carbon interstitial defect is amphoteric, however the single acceptor level lies very close to the conduction band edge (~*0.1 eV*) and is not of concern in n-channel CCDs since it has an emission time constant many times faster than typical CCD line transfer times. The single donor level however is an important defect for p-channel CCDs, with an energy level reported as $(E_v + 0.28)\ eV$ (Mooney, 1977; Frederickson, 1989; Londos, 1989; Song, 1990; Mostek, 2010).

The high mobility of the carbon interstitial results in numerous interactions with other defects and impurities. Another defect of importance in p-channel CCDs is the carbon-oxygen interstitial; formed when the single carbon interstitial is trapped at the site of an oxygen interstitial defect. The C-O interstitial is stable in both a neutral and singly positive charge state, resulting in a single donor state with energy $(E_v + 0.34)\ eV$ (Mostek, 2010).

3.6 - Defect Kinetics

As discussed, silicon contains significant concentrations of various impurities which are introduced during crystal growth and device fabrication. These impurities can interact with the intrinsic Frenkel-pair defects (vacancies and silicon self-interstitials) which are produced by displacement damage. The theoretical framework for describing these interactions is defect reaction kinetics. A huge number of final defect centers are possible; of interest here are the point defects which are known to introduce deep levels into the silicon bandgap at energies which can be problematic for charge

transfer performance in both n- and p- channel CCDs. These have been introduced earlier in this chapter. Defect kinetics can be used to estimate the expected distribution of defects for a given set of conditions and impurity concentrations.

A defect reaction takes the form:

$$X + Y \rightleftarrows_{k_r}^{k_f} XY \tag{3.2}$$

The values k_f and k_r are the reaction rate parameters for the forward and reverse reactions respectively, such that:

$$\frac{d[XY]}{dt} = k_f[X][Y] - k_r[XY] \tag{3.3}$$

where [X], [Y], [XY] are the defect concentrations.

The defects featured in this thesis are formed by intrinsic vacancy and self-interstitial defects. Predominantly these are the silicon divacancy in n-channel CCDs and the silicon divacancy and carbon interstitial defects in p-channel CCDs. The divacancy defect can be formed either directly by displacement damage, or by agglomeration of two single vacancies.

$$V + V \rightleftarrows_{k_2}^{k_1} VV \tag{3.4}$$

In this case *k1* and *k2* represent the reaction rate parameters for the vacancy pairing and divacancy dissociation processes respectively.

The carbon interstitial defect is formed when a silicon self-interstitial kicks out a substitutional carbon impurity via the Watkins replacement mechanism (Watkins, 1964).

$$Si_i + C_s \rightleftarrows_{k_r}^{k_f} Si_s + C_i \tag{3.5}$$

The forward reaction rate parameter k_f is proportional to both the migration enthalpy of the self-interstitial and the capture radius of the carbon substitutional defect. The capture radius represents a distance below which the two defects are considered to form a pair.

The large number of potential defects means that there is a competition between many of the processes. For example a silicon self-interstitial can form a boron interstitial defect via the same process as for the case of carbon, with approximately equal values for the forward reaction rate parameter (Zhao, 1997). The two impurities compete as interstitial trapping sites in p-type silicon (Romano, 1977).

The defect introduction rates therefore depend on the various impurity concentrations. As an acceptor dopant boron is found in p-type silicon in concentrations around $10^{17}cm^{-3}$. Carbon is introduced during the crystal growth process and can be found in both float-zone and Czochralski silicon in concentrations up to $10^{15}cm^{-3}$ (Newman, 1982). In p-type silicon therefore we could expect a significantly larger density of boron interstitial defects than carbon interstitial defects. Fortunately however the born interstitial defect has two acceptor levels at approximately $E_C - 0.13eV$ and $E_C - 0.45eV$ but no donor level (Zhao, 1997). It therefore does not affect the charge transfer in a p-channel CCD.

3.7 – The Effects of Deep Levels in Semiconductors

3.7.1 – Carrier concentrations in an intrinsic semiconductor

For the case of an intrinsic semiconductor without the addition of mid-bandgap levels, the number of free electrons in the conduction band is given by (Grove, 1967):

$$n = N_C e^{\frac{-E_C - E_F}{kT}} \tag{3.6}$$

The number of free holes in the valence band is given similarly by:

$$p = N_V e^{\frac{-E_F - E_V}{KT}} \quad 3.7$$

where $E_{C,V}$ are the energies of the conduction and valence bands, E_F is the Fermi level, and $N_{C,V}$ are the effective densities of states in the conduction and valence bands respectively:

$$N_{C,V} = 2\left(\frac{2\pi m^*_{e,h} kT}{h^2}\right) \quad 3.8$$

where $m^*_{e,h}$ are the density of states effective masses for electrons and holes. The Fermi level in an intrinsic semiconductor is generally very close to the middle of the bandgap. The shallow levels introduced to a typical semiconductor by impurities from the production process or added through doping alter these equilibrium carrier concentrations. The deep-level states which are the study of this Chapter do not affect the charge carrier concentrations directly however they can still have a large effect on carrier dynamics since they provide transition states for movement between the valence and conduction bands.

3.7.2 – Defect occupation

In thermal equilibrium the electron occupation probability of a defect state is given by the Fermi-Dirac distribution function in the same way as for the occupation of any other energy level. For a total defect concentration N_t then the number of states occupied by electrons, holes is given by:

$$n_t = N_t F(E_t) \quad 3.9$$

3.10

$$p_t = N_t[1 - F(E_t)]$$

where the totality condition $N_t = n_t + p_t$ must be met. In other words all defects are occupied by either an electron or a hole.

3.7.3 – Shockley-Read-Hall (SRH) theory

The process of generation in a semiconductor refers to the creation of electron-hole pairs. The opposite process involving annihilation of electron-hole pairs is recombination. Silicon is an indirect semiconductor; therefore the dominant recombination process is a transition via localized states within the bandgap. This is known as Shockley-Read-Hall (SRH) recombination (Shockley, 1952; Hall, 1952). The states can act as generation (G), recombination (R) or trapping (G+R) centres. By providing a transition state within the bandgap they can greatly enhance recombination. Figure 3.8 shows the four basic SRH processes:

a) A neutral trap captures an electron from the conduction band.

b) An occupied trap emits an electron to the conduction band.

c) An occupied trap captures a hole from the valence band.

d) A neutral trap captures an electron from the valence band, leaving a hole.

i) Before:

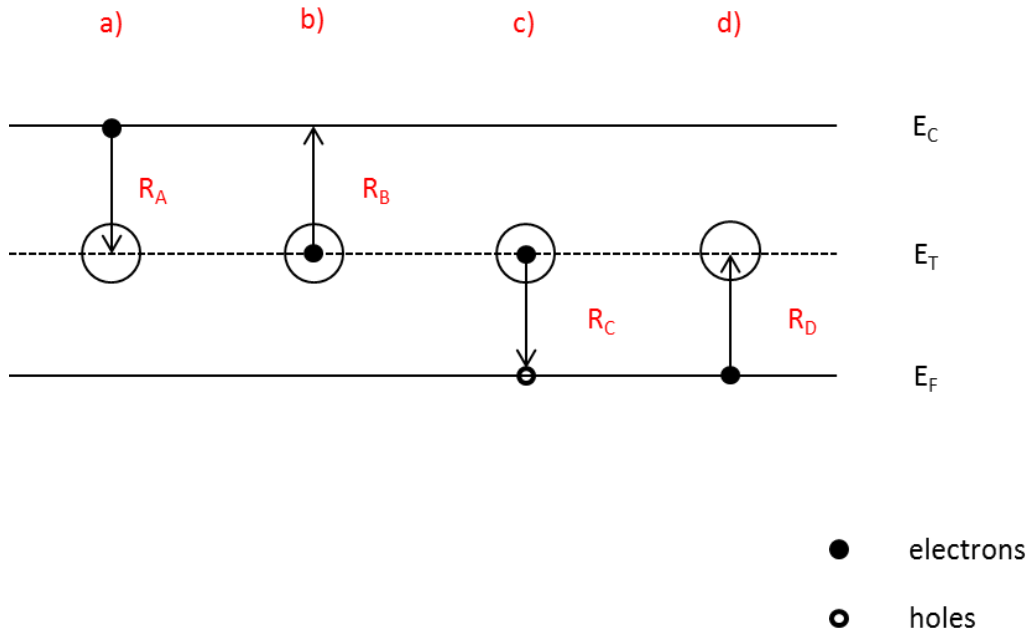

ii) After:

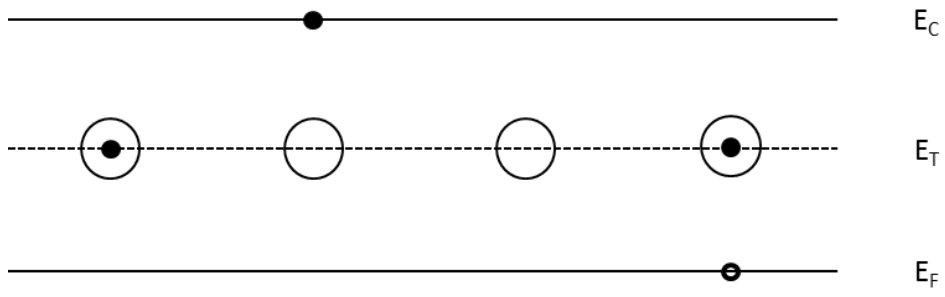

Figure 3.8 – A diagram of the four basic SRH processes with the resulting location of charge carriers given before (i) and after (ii) the process has taken place. The quantities $R_{A,B,C,D}$ are the rates for each process respectively.

For a defect energy level E_T the change in level occupation is given by:

$$\frac{dn_t}{dt} = R_A - R_B - R_C + R_D \qquad 3.11$$

Where $R_{A,B,C,D}$ are the rates for electron capture, hole capture, electron emission and hole emission respectively. For example the rate for electron capture is given by:

$$R_A = nc_n N_t(1 - F(E)) \qquad 3.12$$

Where N_t is the total defect concentration, n is the electron density and $c_{n,}$ is the capture coefficient for electrons. The process of electron capture from the conduction band therefore depends on the electron concentration, the capture coefficient and the number of available free defect states for the electron to occupy, which is given by the Fermi distribution function. Similar expressions exist for the other three processes, containing capture or emission coefficients as required.

The capture coefficients are usually expressed by capture cross-sections $\sigma_{n,p}$ which describe the probability of capture:

$$X_{n,p} c_{n,p} = \sigma_{n,p} v_{n,p} \qquad 3.13$$

where $v_{n,p}$ is the thermal velocity for electrons and holes in silicon. The $X_{n,p}$ term is called the entropy factor and is temperature independent (Hallen, 1996). The entropy factor accounts for the change in entropy accompanying electron emission from a defect level, and its value is usually taken as unity in silicon.

In the case of thermal equilibrium there is no net capture or emission and so R_A=R_B and R_C=$R_{D.}$ This means that the capture and emission coefficients can be related as follows (shown for the electron

case):

$$e_n = \frac{c_n(1-F(E))}{F(E)} \quad 3.14$$

Where e_n is the electron emission coefficient. The capture and emission time constants can then be expressed as the inverse of the capture rates. The two emission time constants for electrons and holes are therefore given by:

$$\tau_{e,electrons} = \frac{1}{N_C \sigma_n v_{th}} e^{\frac{E_C - E_T}{kT}} \quad 3.15$$

$$\tau_{e,holes} = \frac{1}{N_V \sigma_p v_{th}} e^{\frac{E_T + E_V}{kT}} \quad 3.16$$

where $N_{c,v}$ are the local density of states within the conduction and valence bands, as described in Equation 3.4. The electron and hole emission time constants are used extensively throughout this thesis to probe defects and study their properties and behaviour. The emission time constants are highly temperature sensitive and so a high level of temperature control is required throughout this work.

3.7.4 – Field effects on the emission time constant

The emission of charge carriers from a deep level can be enhanced or supressed by several effects related to the presence of a local electric field. Typically the electric field in a CCD pixel is complex; a signal charge cloud experiences a field due to the potential difference between clock phases, but also a self-induced field due to the electrical charge of the carriers themselves (Clarke, 2012). This is in addition to any fringing-field effects.

The Poole-Frenkel effect is one such process that can enhance emission from a defect level. The presence of an external electric field can lower the potential energy barrier for emission, decreasing the emission time constant. The Poole-Frenkel effect has been used extensively to determine defect charge states. However, since it is dependent on the interaction between an external field and the charge carrier it does not affect uncharged defect states. It is also possible for a charge carrier to be emitted through tunnelling effects, either directly or through phonon-assisted tunnelling, where vibrational modes within the lattice can provide additional energy. Tunnelling emission is possible for all defect charge states (Ganichev, 2000).

3.8 – Deep Level Transient Spectroscopy (DLTS)

DLTS is a technique which has been used extensively to study the properties of defects within the depletion regions of semiconductor devices (see for example Hallen, 1996; Eremin, 1999; Zangenberg, 2002; Auret, 2004). Typically DLTS is performed on a diode connected in reverse bias, which is given a voltage pulse allowing free carriers to flow across it and re-charge any defects which are present. Once the voltage pulse has passed, the defects will emit via the thermal emission process. The recovery of the defect charge states causes a transient capacitance within the depletion region, since the diode is essentially storing charge for a small amount of time within defect states. This capacitance can be measured in order to determine the defect energy levels.

The technique works by continually pulsing the voltage at a given rate, termed the “rate-window.” The transient capacitance is then measured repeatedly as the temperature is slowly varied. The change in temperature alters the defect emission time constants and a peak in the capacitance spectrum is obtained when the emission rate of carriers from a particular defect species matches the rate window and so those defects are being most efficiently charged and discharged. The process can then be repeated with a different rate-window, resulting in pairs of temperature and rate-window measurements for each defect species, from which the defect energy level can be deduced.

One disadvantage of DLTS is that you can only study the combined effects of all defects of a given species which are present within the diode. It is also not possible for a DLTS study of a CCD since they are much more complex devices. In this thesis we use the method of trap pumping to probe individual defects directly within the time domain, resulting in more accurate information in particular about the defect emission time constant.

More recently a higher resolution form of DLTS called Laplace DLTS has been developed. In using Laplace DLTS the capacitance transients are digitized and averaged at a fixed temperature, with numerical Laplace transformations then used to determine defect energy levels (see for example Evans-Freeman, 2000; Nyamhere, 2006).

3.9 - The impact of radiation damage on CCD performance

Several excellent summaries and reviews of the numerous detrimental effects of radiation damage in silicon detectors are available (see for example Hopkinson, 1996; Watts, 1997; Lindstrom, 2003). In this thesis we are concerned strictly with the effects of charge-trapping point defects and in particular the accurate analysis of defect emission time constants. These time constants are a key parameter in determining the impact a defect level will have on the final image quality. As the science requirements on CCD imaging sensors becomes ever more demanding, precise knowledge of defect emission time constants becomes vital, both for device optimisation and for the mitigation of radiation damage effects.

Charge-transfer inefficiency due to the effects of radiation-induced lattice defects leads to charge trailing in images, as seen in Figure 3.10 (Massey, 2010). Post-imaging algorithms have been used on images from the HST to reduce deferred charge trails and have shown to be successful, correcting up to 98% of the deferred charge trails (Massey, 2014). The algorithms work by simulating the charge transfer through a model of the radiation damaged CCD (i.e. a CCD containing a number of defects matching those present in the device in space at the time of image acquisition). The success of these

corrections is dependent on the accuracy of the defect distribution which is used in the charge transfer model. In the case of HST, exponentials are fit to the charge trails and the resulting values used in the correction algorithm. This has been proven to work for HST exposures however further progress is limited by factors such as read noise (Massey, 2014).

The implications of radiation damage induced CTI for the ESA GAIA mission have been thoroughly reviewed (Prod'homme, 2012) and were identified as a major challenge for the success of the mission. An analytical model of charge transfer was developed for post-image CTI correction which uses a sophisticated exponential summation of charge trails (Short, 2013). As an analytical model the trap parameters used are semi-physical; they must work within the model to correct the data but may not be entirely physically based. Again this has shown to be a successful approach for GAIA however moving forward models will be required which take accurate physical trap parameters, and therefore the work such as that in this thesis becomes vital for the success of such models.

As an example, the ESA EUCLID mission will aim to investigate the dark universe through weak gravitational lensing surveys of distant galaxies. This involves precise shape measurements to determine spurious ellipticities. Because of the highly sensitive nature of the lensing measurements, extremely detailed knowledge of the imaging system Point Spread Function (PSF) is required, where the PSF describes the response of an imaging system to a point source. It has been shown that approximately a 10x greater level of correction is required than for HST, if the mission is to meet requirements for its entire lifetime (Massey, 2013). To achieve this EUCLID will require trap parameters to be known to within a few percent, or even less in certain cases. Therefore much more detailed information is required than currently available, particularly with respect to defect emission time constants which, as outlined earlier in this Chapter, are not measured directly through techniques such as DLTS. The single-trap-pumping technique developed in the following Chapter provides a tool for probing the emission time constants of defects in a CCD directly and has the potential to provide data with the required levels of accuracy.

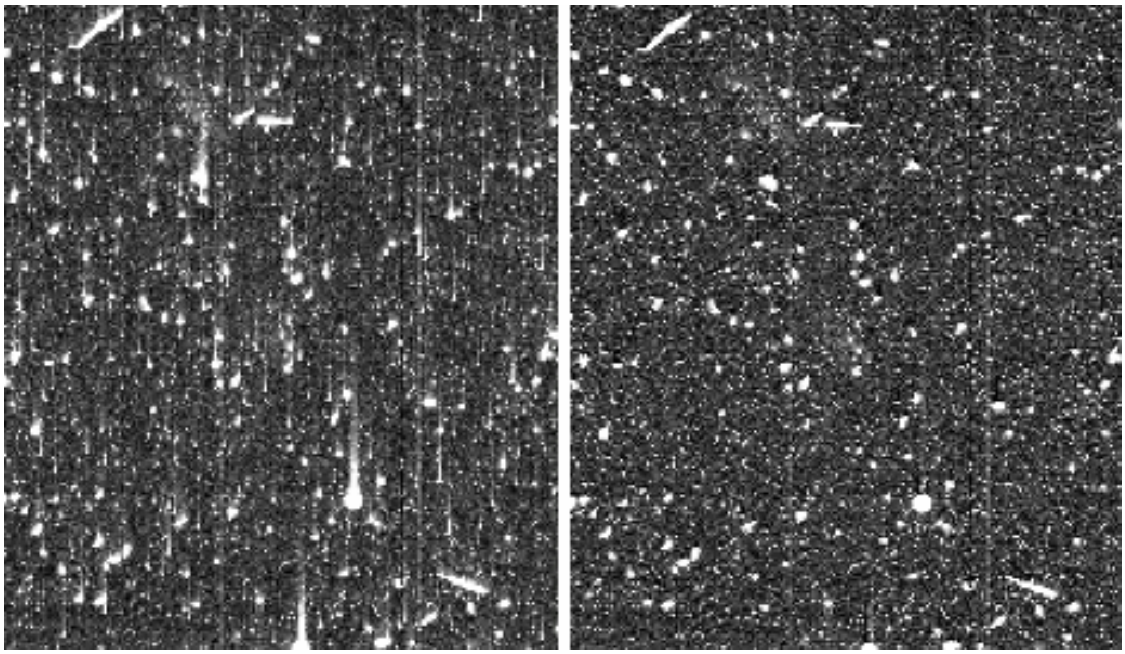

Figure 3.10 – LHS: a typical raw ACS/WFC science exposure from Hubble in early 2010 showing charge transfer trails. RHS: the same image following application of the correction algorithm, showing a large reduction in the charge trailing (Massey, 2010).

3.10 – Summary

One of the numerous effects of radiation damage in a semiconductor lattice is the displacement of host atoms from their lattice sites. The space radiation environment is capable of producing such damage, with protons of particular importance for space-based detectors. Displacement damage leads to the creation of a large number of possible stable defect centres which can introduce deep levels into the silicon bandgap. These levels can act as generation and recombination centres through the capture and release of charge carriers, which has a significant effect on the performance of a semiconductor device. The capture and emission process at a deep level is described by Shockley-Read-Hall theory which can be used to determine an expression for the defect capture and emission time constants. In particular the emission time constant is of great importance for the case

of image sensors since it governs whether or not a given level will affect charge transfer performance and so image quality.

A wide range of methods have been used extensively to study deep levels, in particular Deep-level Transient Spectroscopy. However, little work has been carried out on defects in image sensors specifically or with the intention of probing defect emission time constants directly. Within the context of CCDs as high-end image sensors (particularly for space-based imaging applications) such work is of increasing importance, as the science demands of the devices increases. Both for device optimisation and for radiation damage mitigation techniques, ever more precise knowledge of defect parameters are required.

Chapter 4 – Single trap-pumping

In Chapter 2 the theory behind CCD operation was briefly introduced. Figure 2.7 outlined the typical operating procedure of the clock phases of a CCD such as to read-out signal charge collected in the buried channel of the CCD imaging region. To probe any defects within this region of the device, the method of single trap-pumping is used extensively throughout this thesis. Trap-pumping (sometimes referred to in literature as "pocket-pumping") has been used to study various aspects of CCD performance (see for example Janesick, 2001; Kohley, 2009) and has been developed very recently into a powerful tool for the analysis of the location and properties charge-trapping defects (Murray, 2012; Murray, 2013; Hall, 2014). Presented here is significant further development of the technique for the purpose of the research goals of this work. This development is also one of the key outputs of the research study.

4.1 – The trap-pumping process

Trap pumping works by altering the clock phase sequence such that a signal charge packet is moved backwards and forwards between two adjacent pixels many times (the number of pumping cycles, denoted *N).* This amplifies the effect of any relevant charge-capturing defects within these pixels, allowing for the analysis of several key defect parameters. In particular trap-pumping allows for a direct measurement of defect emission time constants. To produce a trap-pumped image, first a flat-field exposure is taken. It is important to consider the integration time of the flat-field image, since if the background signal level is too low then the signal charge packet will be small in physical size, and is unlikely to encounter enough defects to generate good statistics. Equally, too high a background signal level can be problematic, particularly at high radiation doses where signal charge packets may encounter more than one defect in a pixel, increasing the difficulty of accurate analysis. The effect of background signal level on defect statistics is the focus of a study in Chapter 8. Once a flat-field

exposure has been taken, the signal charge is pumped over *N* cycles. During each pumping cycle there exists a probability that a defect may capture a signal charge from the charge packet within a given pixel and then release it into an adjacent pixel. This probability relates to both the length of the clock phase pulses (referred to throughout this work as the "phase time", t_{ph}) and to the emission time constant of the responsible defect (see Chapter 3).

The large majority of defects which capture charge will release it either much earlier than the next clock pulse (i.e. into the same charge packet from which it was captured) or at a time after the final image has been read-out (signal charge is lost). However any defects which (at the operating temperature of the device) have emission time constants comparable to the clock lengths can potentially capture a signal charge and release it into an adjacent pixel (see detailed discussion in Section 4.12 and Figure 4.3 later in this Chapter). Over many cycles, this leads to characteristic "dipoles" visible in the final image, where a darker than background level pixel neighbours a brighter pixel. An example of a typical signal dipole is shown in Figure 4.1.

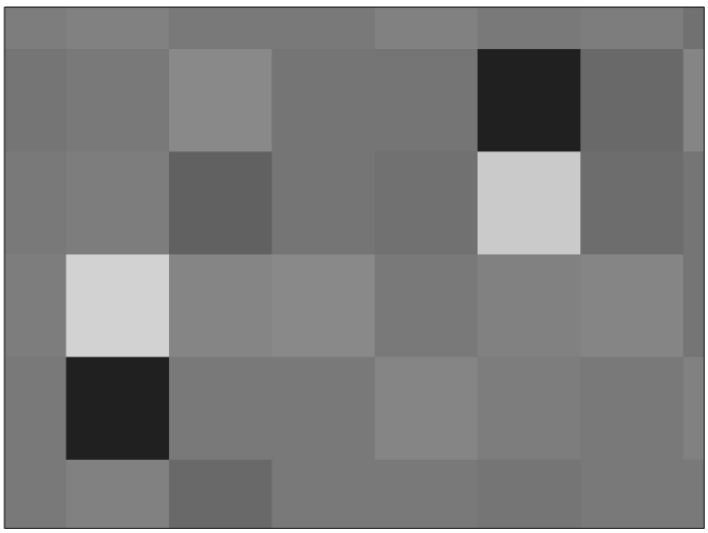

Figure 4.1 - Characteristic signal "dipoles" in a trap pumped image. Dipoles can be oriented either dark pixel first (RHS) or bright pixel first (LHS), depending on the sub-pixel location of the defect. This image was taken from a CCD47-10 which was used for the work in Chapter 5.

To probe defect parameters, the measured quantity is the signal dipole intensity, where intensity simply denotes the number of charge carriers transferred from one pixel to the other. This intensity clearly scales with the number of pumping cycles used, but is also dependent on both the clock timings and the emission time constant of the responsible defect. Since the clock timings are known and can be controlled, this gives a method for directly probing the emission time constants of single charge-trapping defects.

4.1.1 – Detecting signal dipoles

As discussed, the principle of the trap-pumping technique is that the defects which can be probed manifest as signal "dipoles" within a final image; where a dark pixel with respect to the background level neighbours a brighter pixel. An example of a typical signal dipole was shown in Figure 4.1.

The first step therefore in the analysis of defects is the accurate identification of signal dipoles. This was achieved through thresholding and a simple selection algorithm; with the emphasis being to select all single dipoles which appear whilst avoiding clusters of two or more dipoles which appear together. The reason for this is because the aim of this work is to probe defects directly in the time domain with a very high level of accuracy. There are a huge number of atomic lattice sites per pixel; and although multiple relevant charge trapping defects per pixel are not expected to arise often with the radiation fluence used there are still multiple possibilities for the defect distribution within a given pixel (see discussion later in this Chapter on multiple defects). This complicates analysis and so it was decided that including composite signal intensity curves adds another level of difficulty that is beyond the scope of this work, whilst increasing the uncertainty on any parameter measurements. The large number of defects present in the device post-irradiation still allows for good statistical analysis.

The first step in selecting signal dipoles for further analysis was to take the average background signal for each column in the image region. Throughout this work we are interested only in probing the image area of a device. It is possible to use trap-pumping in the serial register of a CCD, where faster defects can theoretically be detected due to the higher transfer frequency. However the serial register of a device is generally small and so numerous devices would be required. Therefore in our work each dipole will appear vertically due to the nature of the parallel CCD readout, and so the background signal for each column was taken individually. A signal level threshold is then set equal to $n\sigma$ where σ is the square-root of the column averaged background signal level and n is a constant to be determined for maximum efficiency in selecting dipoles. The upper and lower thresholds are then equal to $S \pm n\sigma$ where S is the background level and the image area is scanned pixel by pixel for instances where there exists four adjacent pixels that fulfil the following:

1st pixel – signal value lies between the upper and lower thresholds.

2nd pixel – signal value lies above the upper threshold or below the lower threshold.

3rd pixel – signal level lies below the lower threshold or above the upper threshold, i.e. the opposite of the 2nd pixel.

4th pixel – signal level lies between the upper and lower thresholds.

This simple algorithm will pick out single dipoles only, whether they are oriented as light pixel first or dark pixel first. An example of the selection procedure is shown in Figure 4.2 where for simplicity the background signal level has already been removed from each pixel.

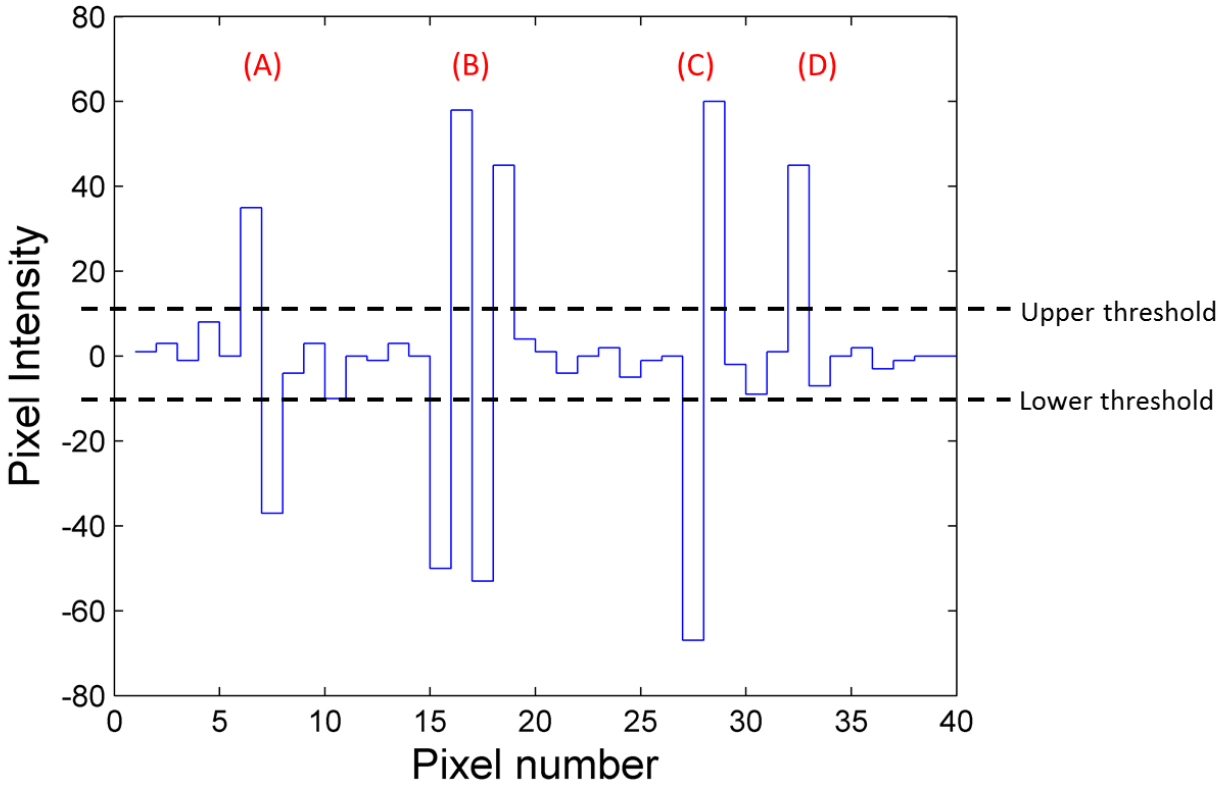

Figure 4.2 – An example of the dipole selection procedure as used on a CCD47-10 for the work described in Chapter 6. For case (A) the dipole will be selected as it fulfils the criteria, and will appear as a light-first dipole. For case (B) the dipole will not be selected since it is more complex than a single dipole. Case (C) will be selected and appear as a dark-first dipole. Case (D) will not be selected as it appears to be only a single bright pixel defect.

To determine the optimum value of *n* several images were searched at different temperatures whilst varying *n.* If the threshold is set too high then clearly it is possible to miss genuine dipoles, however setting the threshold too low also causes dipoles to be missed since it is less likely to find the "starting-point" pixels which lie between the lower and upper signal thresholds. From testing in this way it was determined that *n=3* is an optimum value for selecting single dipoles with maximum efficiency, and so this value was used unless otherwise stated.

4.12 – Determining the defect emission time constant

Along with the explanation given here, a very good description of the trap-pumping process as a tool for defect analysis is given in both (Murray, 2013) and (Hall, 2014). The method of trap-pumping as method for defect emission time constant analysis is best understood through an illustration. Figure 4.3 outlines the clocking process which has been utilised throughout this the work in this thesis. To generate the expression for the signal dipole intensity, an approximation is first made that if a charge carrier comes into contact with an empty trap its capture is instant (in other words the capture time constant τ_c is negligible compared to τ_e). As long as the signal level is sufficiently large then this approximation is valid, since the charge cloud will encounter an empty trap state almost instantly. The time of capture is therefore set as *t=0*. The clock pulse length (i.e. the time taken for the charge cloud to move from one pixel to the adjacent pixel) is referred to from this point onwards as the "phase-time" t_{ph}.

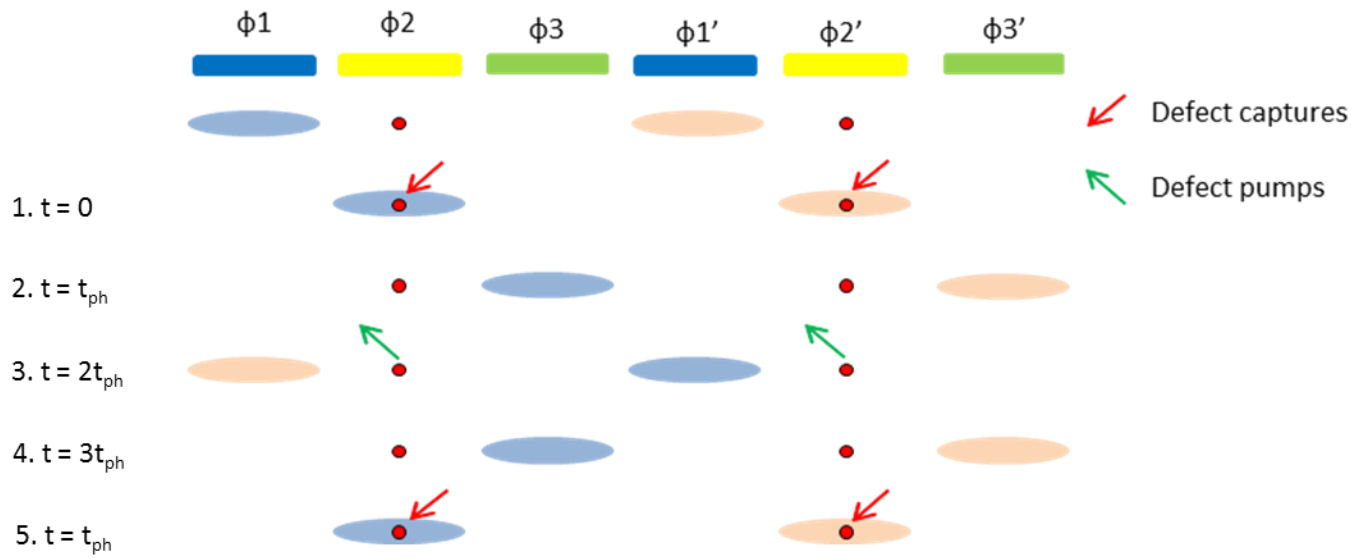

Figure 4.3 – The typical clocking process for the trap-pumping technique using a 3-phase device such as the CCD47-10, with a defect beneath phase 2. The time is set to t=0 at the time of capture, with t_{ph} the phase time. An important note is that the clocking scheme shown will only produce dipoles for defects in barrier phases during image integration. For defects beneath collection phases (i.e. phase 1 in this Figure) there is no net signal pumping effect. To generate statistics for every defect two runs would therefore be required, altering the phases held high during integration.

As outlined in Chapter 3, once a charge is captured by an empty defect level the process becomes a simple exponential decay, where the probability of release before a given time *t* is given by:

$$P_p = 1 - \exp\left(\frac{-t_{ph}}{\tau}\right) \quad 4.1$$

Where t_{ph} is the phase-time as previously defined (see Figure 4.3) and τ is the temperature dependent emission time constant of the level (see Equation 3.12). It can be seen from Figure 4.3 that if a charge is released when *t* lies within the range $t_{ph}<t<2t_{ph}$ then the nearest signal charge packet will not be the original charge packet and the charge will move into an adjacent signal charge packet. The probability per pumping cycle of this occurring is given by Equation 4.2. If a charge is successfully pumped over many cycles, then one charge packet will have lost a significant number of charges, whilst the adjacent packet will have gained them. Therefore a dipole is produced, such as those which were shown in Figure 4.1.

$$P_p = \exp\left(\frac{-t_{ph}}{\tau}\right) - \exp\left(\frac{-2t_{ph}}{\tau}\right) \quad 4.2$$

As previously stated, the dipole intensity is defined as the total number of signal charges "pumped" from one pixel to the next. It is clear therefore that this will be equal to the probability per cycle that a charge is pumped (Equation 4.2), multiplied by the total number of cycles *N*. This leads to Equation 4.3 which relates intensity to the phase-time and the emission time constant.

4.3

$$I = NP_p = N \exp\left(\frac{-t_{ph}}{\tau}\right) - \exp\left(\frac{-2t_{ph}}{\tau}\right))$$

In Equation 4.3 it has been assumed that the probability of capture is 100%. If this is not a valid assumption then the probability of capture is added as a simple scaling factor which accounts for the local field effects, lattice strain etc. An advantage of the technique is that since the capture probability scales the dipole intensity it does not provide a significant source of measurement uncertainty on emission time constant measurements, as it does not affect the peak of the curve (i.e. where the defect is pumping signal at maximum efficiency). It is important to note however that the capture probability is still likely to affect the overall spread observed in time constant distributions due to effects previously outlined.

4.1.3 – Intensity curve fitting

A method is therefore developed where tracking the dipole intensity across a set of images with varying phase-time results in a curve which can then be fitted with Equation 4.3 to give a value for the emission time constant of the underlying defect. Simple differentiation shows that peak of the curve should occur at a phase time equal to approximately $ln(2)\tau_e$ and therefore if the correct phase time range is chosen we can search for distinctive curves such as the example shown in Figure 4.4, where the intensity rises to a maximum before falling again.

Curve fitting is performed with the Matlab “ezyfit” package. This uses the Nelder-Mead method of a minimization of the sum of squared residuals, taking as an input a set of initial values for the unknown variables. An example of a fit is shown on the curve in Figure 4.4. A Pearson’s fitting parameter (r-value) defines the strength of the fit, with a value of unity indicating a perfect correlation with the data. In order to determine a suitable threshold r-value for inclusion of a curve

in the final statistics, testing was carried out in which the threshold was varied and both the number of fits above threshold and the spread of the resulting emission time constant distribution was recorded. With respect to the motives of this work and the large number of defects available for study it was decided to choose a relatively strict r-value threshold of r>0.85. This means that reported defect densities are likely to be underestimated, however it provides the most reliable method for highly accurate measurement of defect emission time constants, which is the principle aim of this work.

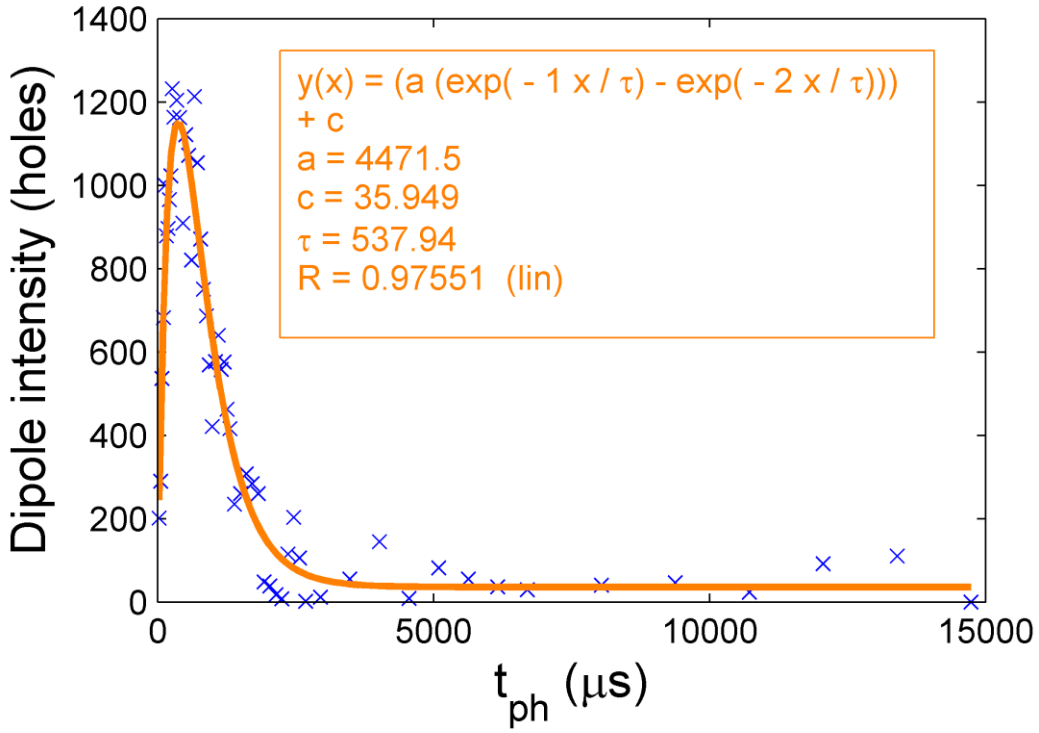

Figure 4.4 – An example of the characteristic dipole intensity curve produced by a single defect beneath a barrier phase in a 3-phase CCD. This image is an example of a carbon interstitial defect (see Chapter 5).

4.1.4 – Energy and cross-section analysis

Through the technique of single trap-pumping it is possible to accurately determine defect emission time constants at a given temperature. If it is possible to locate and analyse a given defect in this way at a number of different temperatures then using SRH theory it is possible to estimate the defect cross-section and energy level within the band. This is important as defect emission time constants are highly sensitive to a number of conditions and have a large uncertainty range when calculated theoretically. It can therefore be difficult to characterise a defect based only on this information. By fitting emission time constant vs. temperature curves we can get an estimate for both defect cross-section and energy level, which helps to identify the defect species. This also can help to explain any anomalous results in the emission time constant distributions, where there may for example be two defect species interfering with each other. As an example of the sensitivity of the emission time constant, Figure 4.5 shows a plot of the theoretical emission time constant over a 40K temperature range for a defect with an energy level of $(E_v+0.20)\ eV$ and a varying cross-section. As would be expected from Equations 3.12 and 3.13, it is observed that an order of magnitude difference in the cross-section values at these temperatures leads to around an order of magnitude difference in the theoretical emission time constant. The importance of this is realised when searching the literature for the cross-sections of deep-level defects, since often several very different values are quoted. This must therefore be considered when planning a trap-pumping study, as for example a defect with an expected emission time constant of around $5000\ \mu s$ is well within range of the technique; however a defect with an emission time constant of $50000\ \mu s$ is out of range. This will be discussed further at the end of this Chapter.

Determining the energy of a defect also allows for more direct comparisons to be drawn with a number of other studies, since typical methods of defect analysis such as DLTS (see Chapter 3) measure the energy level directly. Very little information is available on defect emission time constant analysis directly, particularly for the case of an image sensor. It is therefore one of the aims

of this work to introduce this technique and provide useful data which can supplement current understanding.

The emission time-constant curves are fit with Equation 3.12 or 3.13 depending on whether the defect level is an electron or hole trap. These equations are non-linear and have three temperature dependent terms. Since we have two unknown variables and only one equation relating them, this method can only be used to provide estimates of defect parameters since the values will remain inherently coupled. However, this process is still valuable because the number of defects which can be analysed using trap-pumping is high, and so distributions can be built meaning statistically it is possible to draw conclusions about defect species when the information used to supplement the accurate emission time constant data.

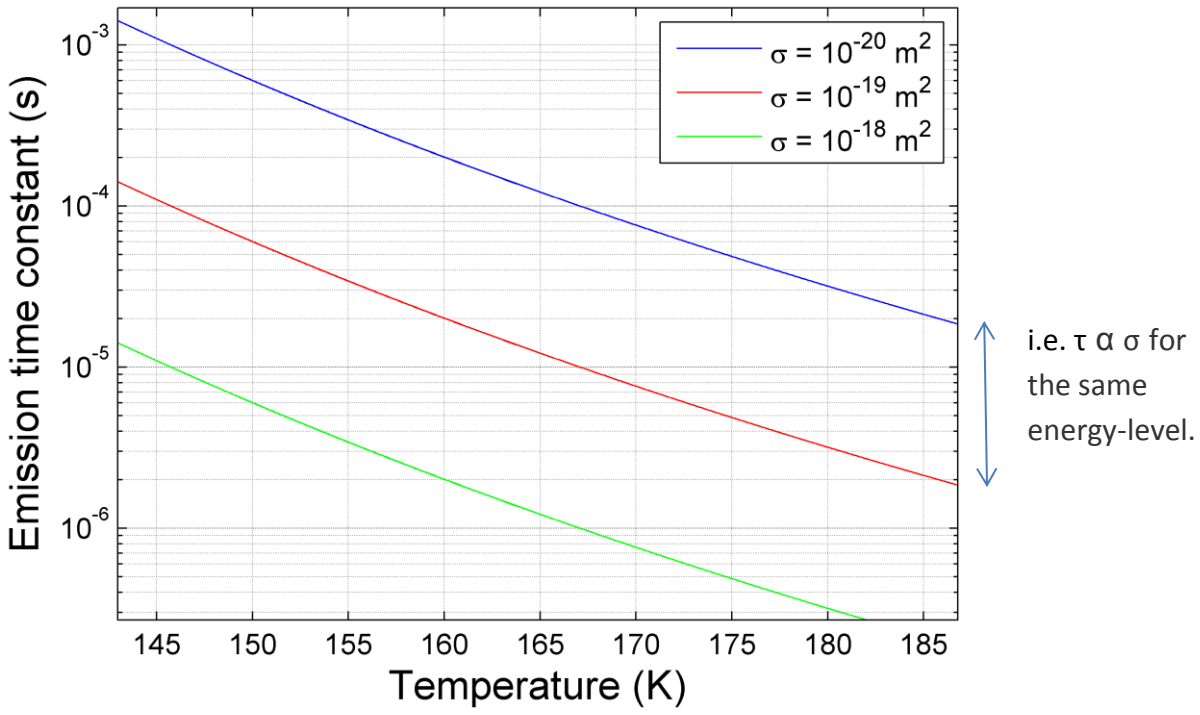

Figure 4.5 – The calculated emission time constant vs. temperature, for a defect level with an energy level of 0.20 eV above the valence band edge, and a range of cross-section values.

4.2 – Trap-pumping in a 4-phase device

The technique described so far in this Chapter has been designed to work for a typical 3-phase CCD with electrodes of equal width. This allows for the formation of Equation 4.3. However, the p-channel CCDs which are used throughout the course of this work are actually 4-phase devices, with unequal phase widths. In order to successfully use the technique with a 4-phase device, two phases were clocked together, in order to form a "pseudo 3-phase" device. This enabled defects to be studied with the technique as it has been outlined; however this leads to a number of possibilities for a single defect dipole intensity curve, depending on the sub-pixel location of the defect. Throughout this work we are focussed on the accurate analysis of single defects in the time domain. We are therefore searching for signal dipoles which show the characteristic shape seen in Figure 4.4. However it is important to discuss the possibilities for a 4-phase device to predict the dipole intensity curves that will be observed, so that only those which are desired can be analysed further. It is important to note that if there are multiple relevant defects in a single pixel (or in adjacent pixels) then the number of possibilities quickly becomes very large. Therefore we will focus our attention on the possible curve types for a single defect.

Phase 1 - The clock phases were connected as shown in Figure 4.6, with phases 1 and 2 clocked together. It can also be seen that phases 2 and 4 are twice the width of the other two phases. For a defect beneath phase 1 there are two possibilities depending on the location beneath that phase. If the defect lies beneath the LHS of phase 1 then it will pump signal charge into an adjacent charge packet if it has an emission time constant less than $2t_{ph}$. Because of the unequal phase widths, increasing the phase time only increases the probability of pumping since the nearest charge packet is always from the adjacent pixel. Therefore a "flat-level" dipole intensity curve is produced which reaches a maximum value and does not fall. An example of such a curve is shown in Figure 4.7. However if the defect lies beneath the RHS of phase 1 there will no net pumping effect regardless of

the emission time constant, since any signal pumped from one charge packet to the next is countered by the opposite effect within the same pumping cycle (i.e. the processes at stages 3 and 6 in Figure 4.6 are equal and opposite.)

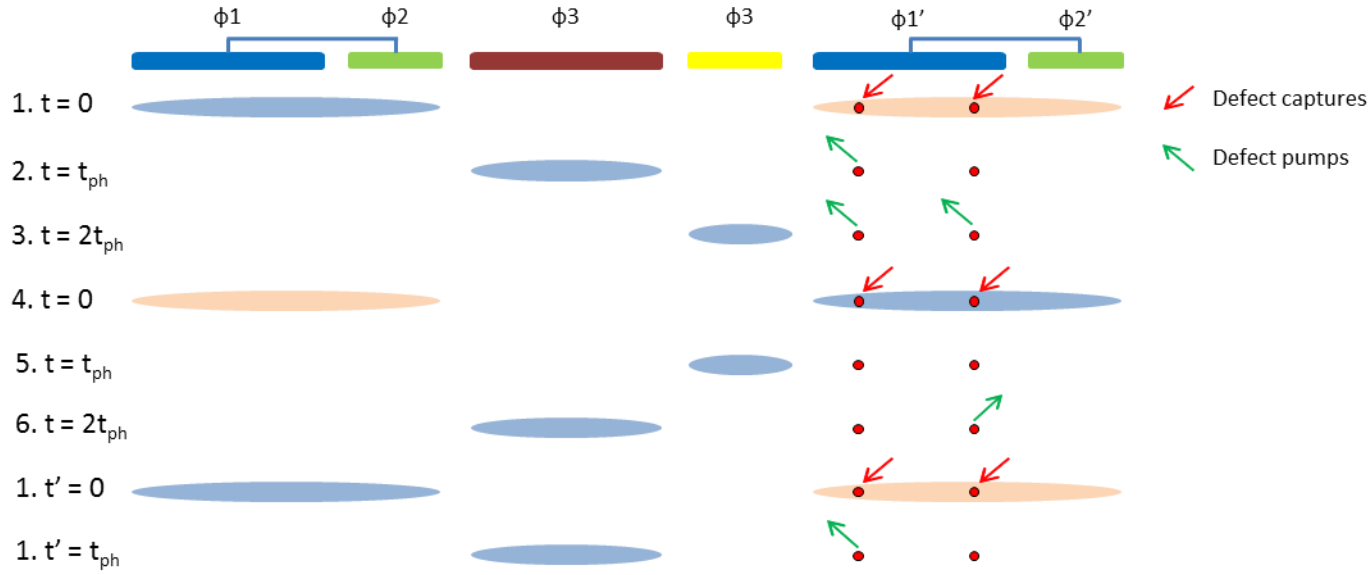

Figure 4.6 – The trap-pumping process for a 4-phase device such as those used throughout this work. Electrodes 1 and 2 are clocked simultaneously to give a pseudo 3-phase operation. This Figure shows the two possibilities for a single defect beneath phase 1, with no influence from any other defects. The red arrows indicate capture of a carrier and the green arrows indicate "pumping" where the carrier is released into a different charge packet from which it was captured.

Phase 2 - For a defect beneath phase 2 there are also two possible scenarios. A defect beneath the LHS of phase 2 is equivalent to the case for the RHS of phase 1; there is no net pumping effect regardless of emission time constant. A defect beneath the RHS is equivalent to a defect beneath the LHS of phase 1 and produces a "flat-level" intensity curve if the defect emission time constant is below $2t_{ph}$.

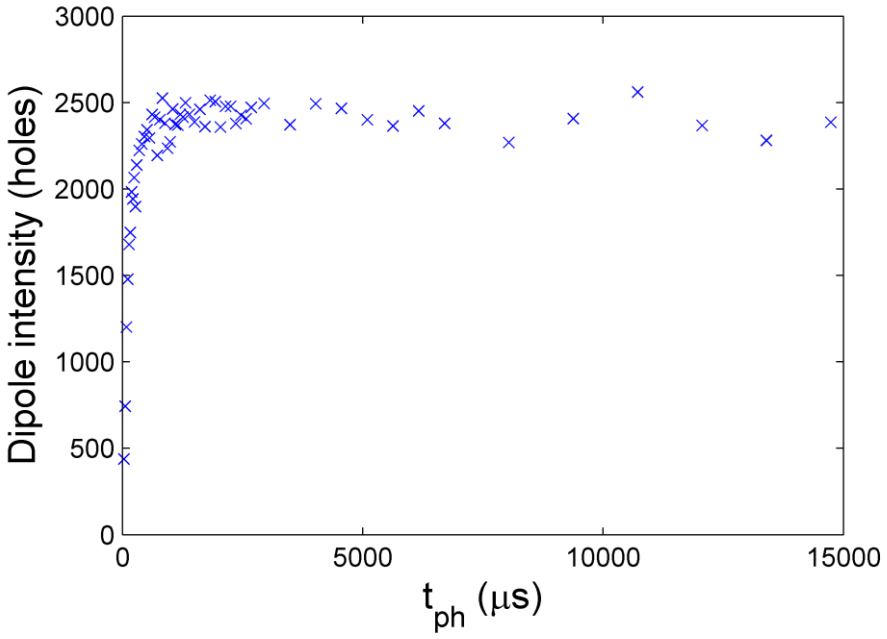

Figure 4.7 – An example of a typical "flat-level" curve produced by defects in certain positions within the pixel. This occurs due to the unequal phase widths.

Phase 3 – The case for a defect beneath phase 3 is shown in Figure 4.8. A defect beneath the LHS of phase 3 produces the "regular" dipole intensity curve that we are searching for in the case of defect parameter analysis. If the defect emission time constant is between t_{ph} and $2t_{ph}$ then pumping occurs. However for a defect beneath the RH quarter of phase 3 then the defect always pumps signal charge and a "flat-level" curve is produced if the emission time constant is less than t_{ph}. Note that this is a different condition than for the "flat-level" curves produced for single defects beneath phases 1 and 2.

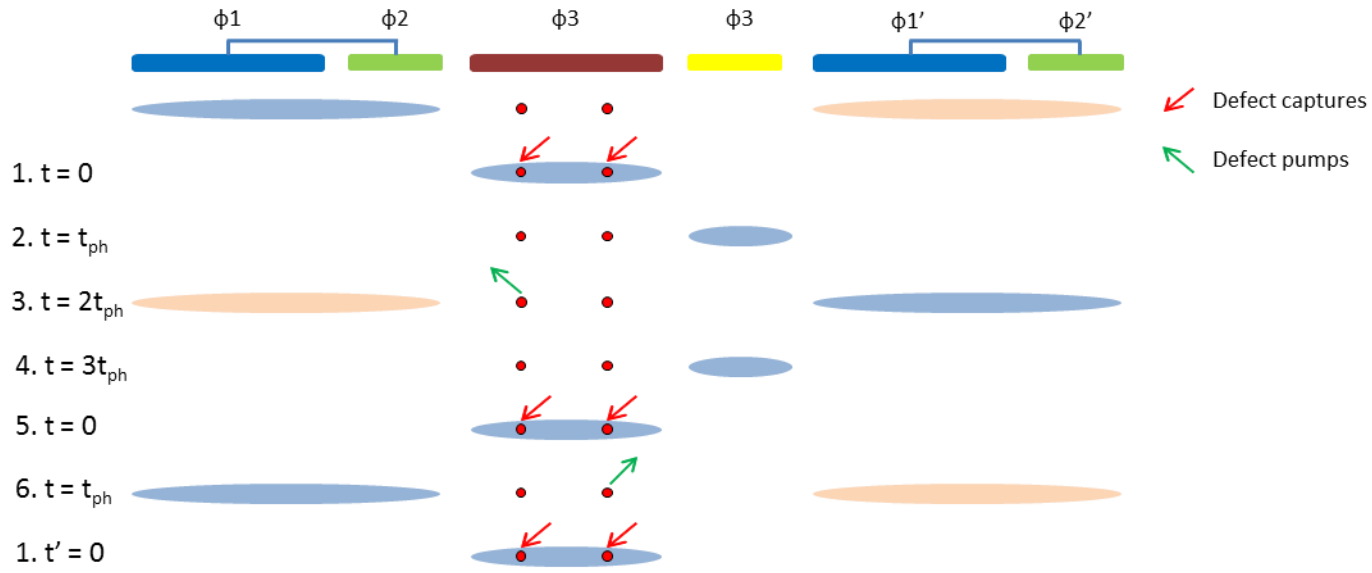

Figure 4.8 – The two possibilities for a single defect beneath phase 3 without the influence of any other defects. The red arrows indicate capture of a carrier and the green arrows indicate "pumping" where the carrier is released into a different charge packet from which it was captured.

Phase 4 - There is only one possibility for a single defect beneath phase 4, which is to produce a regular dipole intensity curve where pumping occurs when the emission time constant is between t_{ph} and $2t_{ph}$. This is analogous to a defect beneath a barrier phase in a 3-phase device, as in Figure 4.3.

In summary there are two possible intensity curves that can be produced by a single defect beneath a given pixel in a pseudo 4-phase operation. The first type is the "regular" intensity curve such as that produced in a 3-phase device for a defect beneath a barrier phase. These are the curves which are desired for analysis of defect parameters and occur for a defect beneath 5/12 of the total pixel area (3/4 of phase 3 and the entire area of phase 4). The second curve type is the "flat-level" curve, which is produced for a defect beneath approximately 3/12 of the total pixel area (1/2 of phases 1 and 2). A defect beneath the remaining 4/12 of the total pixel area gives no net pumping effect. Here however we have only considered the effects of a single defect. In reality there can be several charge-trapping defects within any given pixel, along with defects in the neighbouring pixels which can also have an effect since they are capturing from and emitting to the same charge packets, only

at different times. Therefore a whole range of compound intensity curves is possible, such as an "inverted" type curve produced by a flat-level defect and a regular defect working against one-another. These types of compound curves are seen frequently and for the work in this thesis they are to be avoided, since there are simply too many possibilities to accurately determine defect parameters from them.

4.3 – Limitations to the trap-pumping method

The trap-pumping technique is a powerful tool for analysis of charge-trapping defects in an image sensor. However, there are numerous considerations which must be taken into account for a trap-pumping study. Firstly, by definition the technique only probes defects which are electrically active and can capture a signal charge carrier. With respect to image sensors however this is unimportant as only these defects are of concern for the charge transfer performance; i.e. the defects not detected through trap-pumping do not affect charge transfer and so have no impact on image quality. Still it must be stated clearly that the technique will not show up every defect present in the device. Similarly, as has been previously mentioned only those defects with emission time constants comparable to the phase time range are detected. Therefore the phase time range must be carefully chosen; it is limited at the low end by the maximum clocking frequency, which restricts us to a minimum phase time of the order of $1\ \mu s$. Below this value the clock waveforms become unreliable as there may not be sufficient overlap for charge transfer. The maximum phase time is limited only by the amount of time for which you can run the CCD under constant conditions (dark-current etc.). The maximum value used in this thesis is of the order of $10^4\ \mu s$. This phase time range at the tested temperatures should be sufficient for analysis of the defects which are expected to dominate the CTI contribution under typical operating conditions.

Because of the above considerations the defect densities have not been studied closely throughout this thesis, since a number for density without the device conditions etc. would be generally meaningless. However it is possible to estimate *relative* defect densities using trap-pumping. This is discussed as part of the work in Chapter 6. Despite the limitations described above trap-pumping remains a very strong defect analysis tool in CCDs and has distinct advantages over other commonly used techniques. For example the previously discussed DLTS method uses diode structures and so trap properties are not studied under CCD conditions. DLTS also analyses the combined effects of all defects of a certain species present in the device, whilst trap-pumping in a CCD locates and studies the properties of individual defects. This is of importance with respect to the future radiation hardness of future space missions (see section 3.10) where trap properties are required to within a few percent for CTE correction.

Chapter 5 – Trap-pumping analysis of a proton-irradiated p-channel CCD

The technique of single trap-pumping was described in Chapter 4 as a method for probing the defect emission time constants within a CCD. To test the method and as an initial study into radiation induced deep-level defects, a proton irradiated p-channel CCD was analysed. The primary aim of the study was to probe the defect emission time constants within the CCD post-irradiation using the techniques described in Chapter 4. Currently n-channel CCDs are the standard for space-based imaging applications, however the use of p-channel CCDs is likely to grow in the future since it is has been shown that they are potentially more tolerant to radiation damage effects (Marshall, 2004; Dawson 2008; Lumb, 2009). This arises from the fact that the predominant charge-trapping defects for holes are expected to have emission time constants which lie further away from typical transfer times at operational temperatures than comparative electron traps. Accurate data on radiation-induced hole-trapping defect emission time constants is therefore required to support these claims.

5.1 – Introduction

For the case of a p-channel CCD, three defects are expected to be of most importance when considering CTI: the donor level of the divacancy, the carbon interstitial defect and the carbon-oxygen interstitial defect (Mostek, 2010). However, at typical CCD operating temperatures for a space mission (~150K) the carbon-oxygen defect has an emission time constant of the order of seconds and is therefore less of a concern with respect to the radiation damage effects which were discussed in Chapter 2. With such a long time constant the defect level also becomes very difficult to analyse using trap-pumping since a large number of pumps are used. Therefore focus is paid to the other two defect species. Figure 5.1 shows the expected defect emission time constants over the range 120-220K, as calculated using SRH theory (see Chapter 3). The energy level and cross-section

values used for the data in the plot are taken from the 2010 study by Mostek in which a variant of the trap-pumping technique was used to study defect energy levels in an irradiated p-channel CCD (Mostek, 2010). The upper and lower limits in Figure 5.1 were calculated using the respective upper and lower limits for energy and cross-section from the study by Mostek. Using this method the uncertainties in both quantities combine and it can be seen that for a relatively small range in energy and cross-section a large range of values are possible for the emission time constant at a given temperature, particularly for the case of the carbon interstitial defect.

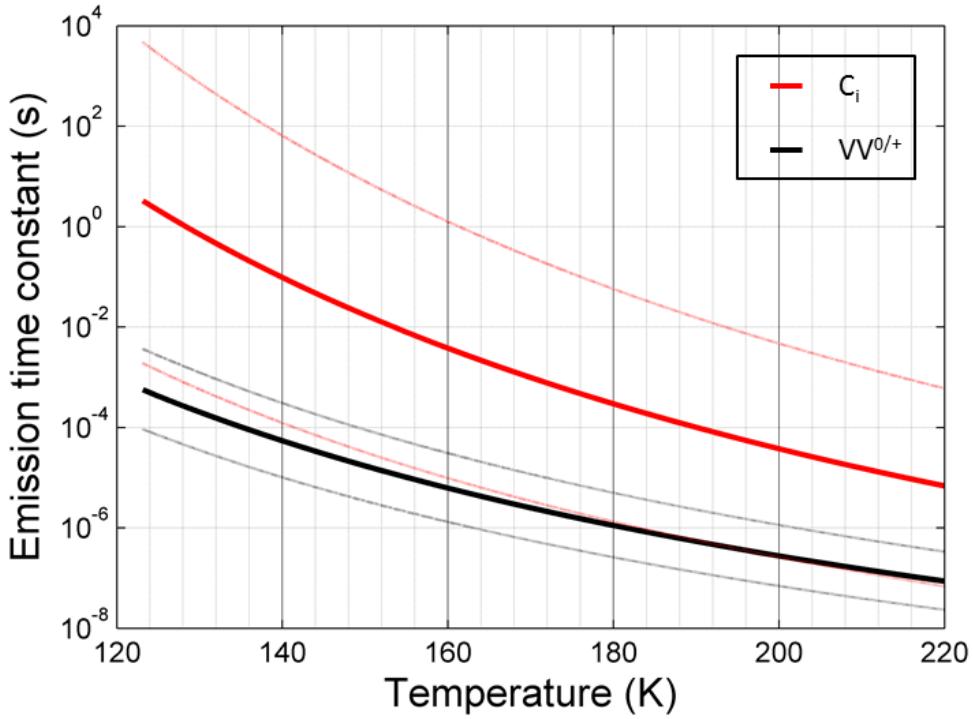

Figure 5.1 – Defect emission time constants for both the carbon interstitial defect and the donor level of the divacancy. The curves were plotted using SRH theory and the values of energy and cross-section as found in (Mostek, 2010). Note the large range for emission time constant (dashed lines indicate upper/lower limits) due to combining the uncertainties in energy and cross-section.

The aim of this study is to use the trap-pumping technique developed in Chapter 4 to probe defects within a proton irradiated p-channel CCD and measure defect emission time constants directly. With precise knowledge of defect locations and emission time constants it is possible to vastly improve effective device lifetimes in a harsh radiation environment through optimisation and post-image

correction techniques. This information is vital if the aims of upcoming space missions such as the ESA EUCLID mission are to be realised (see section 3.10). Such analysis of defect parameters is also of importance when analysing the potential for p-channel devices to exhibit a greater tolerance to radiation, which is thought to be possible because of the preferential properties of hole trapping defect levels as opposed to electron trapping defect levels.

5.2 – Device irradiation and initial testing

The data in this Chapter were taken as part of a wider study into an assessment of radiation damage for the EUCLID space observatory (see Gow, 2012). The device used for the work in this Chapter was an e2v p-channel CCD204, which is an earlier version of the baseline EUCLID device CCD203 (Endicott, 2012). The CCD204 is a 4-phase device with a charge injection structure and a split output register operation. The pixel pitch is 12µm, with an image area of 1k x 4k pixels. A schematic of the CCD204 design structure is shown in Figure 5.2.

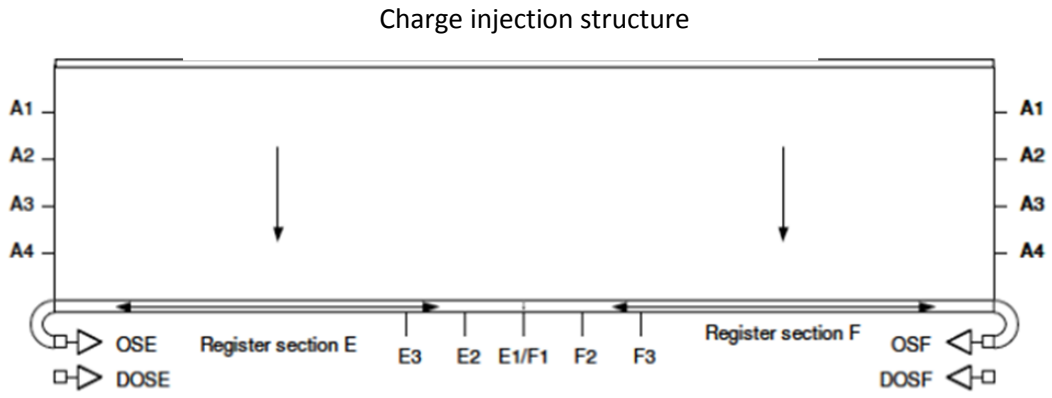

Figure 5.2 – A schematic of the CCD204 showing the split register design (Gow, 2012).

For this work one half of the total device image area was used (i.e. the output of one of the two nodes). This gives a 1k x 2k pixels image area, of which 50% was irradiated at room-temperature to a 10 MeV equivalent proton fluence of $4x10^{9} p\ cm^{-2}$ with the other 50% left as a control region. The fluence was chosen to represent the approximate expected end of life fluence for EUCLID (Murray, 2012). The area chosen for trap-pumping analysis (ROI) was a 500x500 pixel region of the irradiated section of the device. Both the irradiated area and the ROI are shown in an example image from the single output node in Figure 5.3, which also shows both the parallel and serial overscan regions. During CCD readout it is possible to "overscan" the device by adding more rows or columns to the readout than there are physical pixels. This creates overscan regions such as those in Figure 5.3 which can be used for correction of CCD bias, i.e. the unwanted signal generated by the electronics. Two temperature and phase time ranges were chosen for study, with the aim of probing both of the defect species within the limits set by the trap-pumping technique and device temperature. To probe for the divacancy level three temperatures between 149-159K were tested, with 100 images taken at each temperature covering phase-time values of approximately *1-200 µs*. Probing for the carbon interstitial defect three temperatures between 172-180K were tested, with between 57-130 images taken at each temperature, covering the phase time range ~*1-15000 µs*. The temperature of the device was monitored using a pt-1000 resistance thermometer which was attached to the CCD packaging as shown in Figure 5.4, and a Lakeshore temperature controller. The Lakeshore has a temperature stability of 0.2K. It could realistically be expected that a small temperature variance will be observed across the whole device, and therefore any significant temperature changes were always followed by a waiting period of several minutes to ensure temperature had stabilised sufficiently across the device. Since only a small region (the buried channel) is used for charge transfer, it can be assumed that the temperature variation across it in a given run is negligible. The maximum total deviation in temperature across a single trap-pumping run was found to be 0.5K. Figure 5.5 shows an image of the experimental set-up; the CCD was contained within a vacuum chamber and cooled using a Polycold compact cooler and Cryotiger cold-end system. An XCAM

camera system was used to control the CCD basing and clocking voltages as well as the CCD output. The XCAM system also has a USB interface to allow images to be read directly into Matlab or another suitable software package.

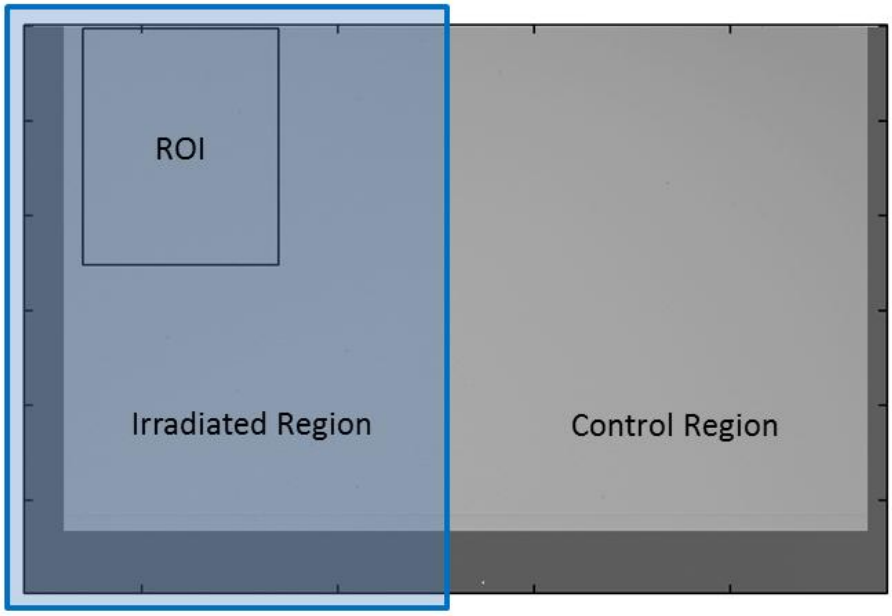

Figure 5.3 – A sample image from a single node of the CCD204 showing the region irradiated with protons (blue area) and the parallel/serial overscan regions. Also shown is the ROI chosen for signal dipole analysis, which is 500x500 pixels in size.

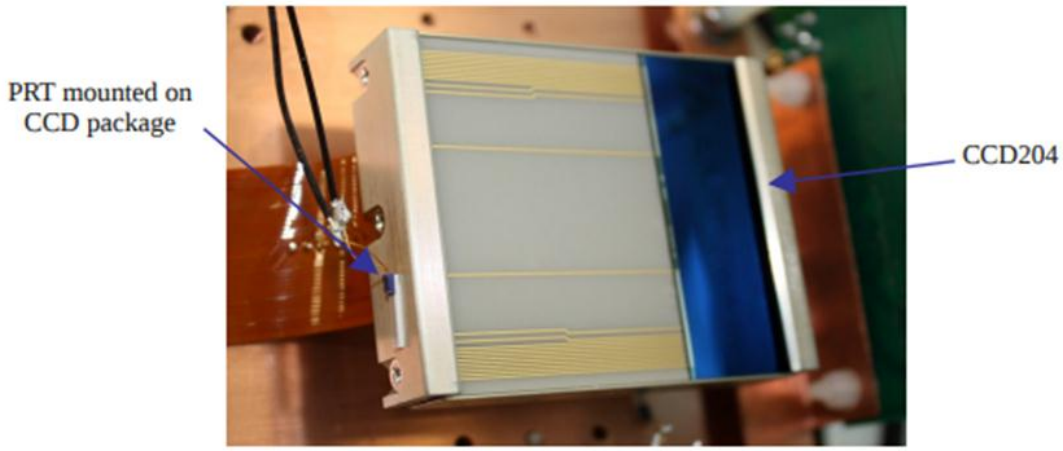

Figure 5.4 – A photo of the CCD204 showing the position of the pt-1000 resistance thermometer attached to the CCD packaging (Gow, 2012).

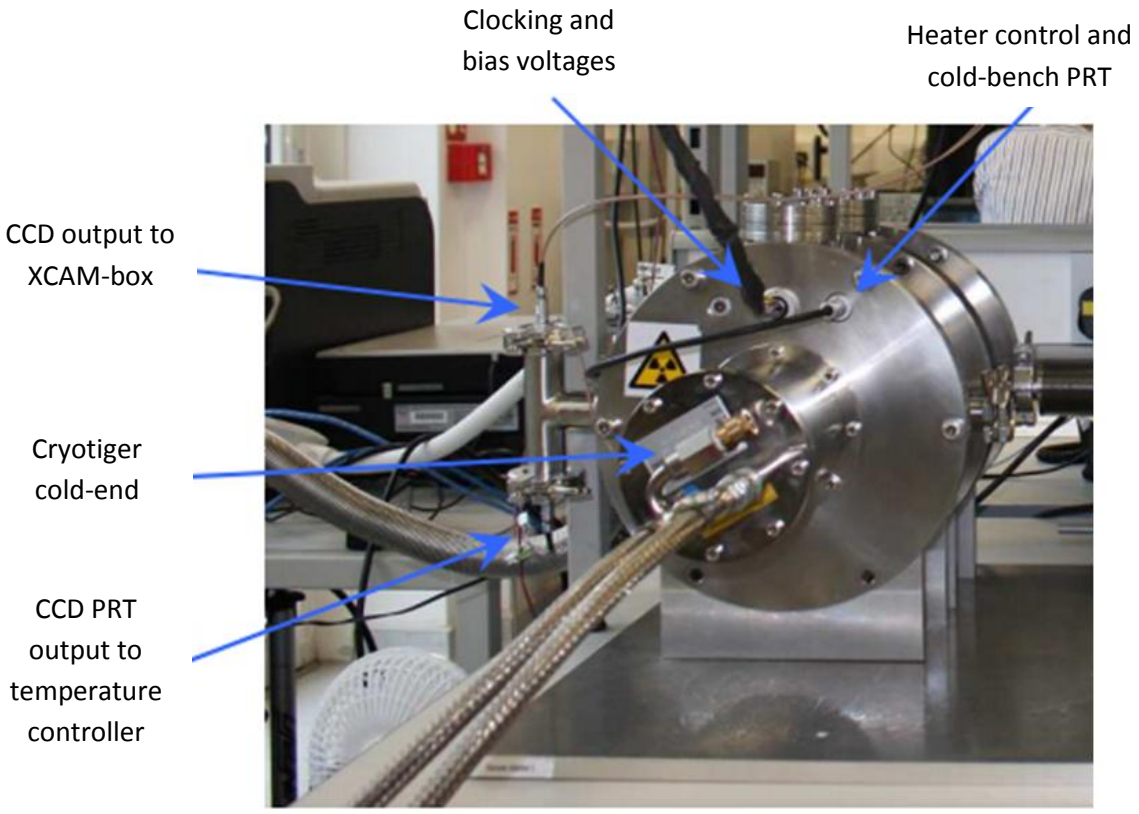

Figure 5.5 – A photo of the experimental set-up showing the vacuum chamber, Cryotiger cold end and CCD input/output connections. Note that this image was taken during an X-ray source experiment (as part of a wider p-channel CCD study) and so the source chamber has been removed from the image (RHS) since this was not required for the data taken as part of this work (Gow, 2012).

The CCD204 is a 4-phase operation device and so was connected in the pseudo 3-phase operation as described in Chapter 4. The number of pumps used for each image taken was *N=4000*. For dipole detection, a threshold of 3σ was used for the signal level background during dipole detection, as described in Chapter 4. Since the desired signal dipoles are detectable over a range of images, not all images were searched for dipoles and instead a selection of images covering the entire phase-time range was chosen for each temperature set. This reduces the time taken to gather all of the data without compromising the number of signal dipoles available for analysis.

At all six tested temperatures operation of the CCD produced images containing signal dipoles for detection and further analysis. An example of signal dipoles in a trap-pumped image from the dataset taken at 172K is shown in Figure 5.6. Both light pixel first and dark pixel first signal dipoles were observed as expected. As described in Chapter 4 only single dipoles for which both the light and dark pixel values lie outside the signal level threshold were selected for tracking of the dipole intensity curve across the phase time range. A selection of observed dipole intensity curves is shown in Figure 5.7. Note that from work as part of the wider study into p-channel CCDs the gain of the device was known and so dipole intensities could be given in units of holes, as opposed to Digital Numbers (DN). However this does not affect the position of the emission time constant peak and therefore does not affect the measured emission time constant (curves in later Chapters of this work are given in units of DN). As well as the “regular” intensity curves which are desired for emission time constant analysis, a number of other curves are observed including those as expected when considering the possible scenarios for a single defect beneath a particular phase (see Chapter 4). Other curve types likely arise due to the interaction of multiple charge-trapping defects within either a single pixel or neighbouring pixels. The intensity curves are fitted with Equation 4.3, which is for the case of a single charge-trapping defect, using the “ezyfit” package for Matlab. The goodness-of-fit is quantified using the Pearson correlation coefficient (r-value) which provides a fast, simple check for the strength of a model and for comparing models. Throughout this work, only those curves displaying an r-value greater than 0.85 are accounted for in any final analysis. Along with a simple procedure for discounting any “flat-level” curves, which is based on the phase-time value at maximum dipole intensity, this was shown to be a reliable method of excluding unwanted intensity curves without significant loss of genuine data. For all signal dipoles which were successfully detected and fit the emission time constant of the responsible defect was deduced. With the analysis of many such defects this allowed for the construction of emission time constant distributions. For those defects which were successfully detected and fit at all three temperatures in

a particular temperature set 149-159K or 172-180K energy levels were estimated using the method described in Chapter 4.

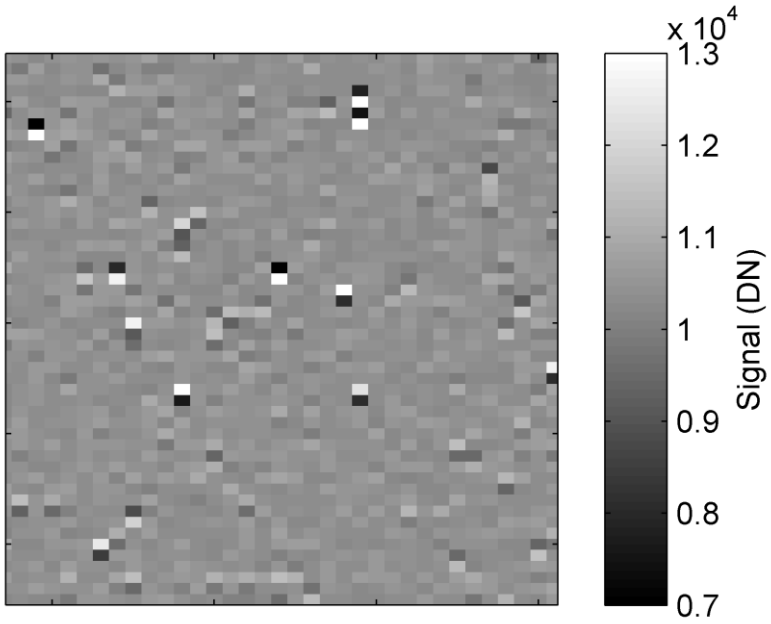

Figure 5.6 – An example of signal dipoles in a trap-pumped image from the CCD204 at 172K.

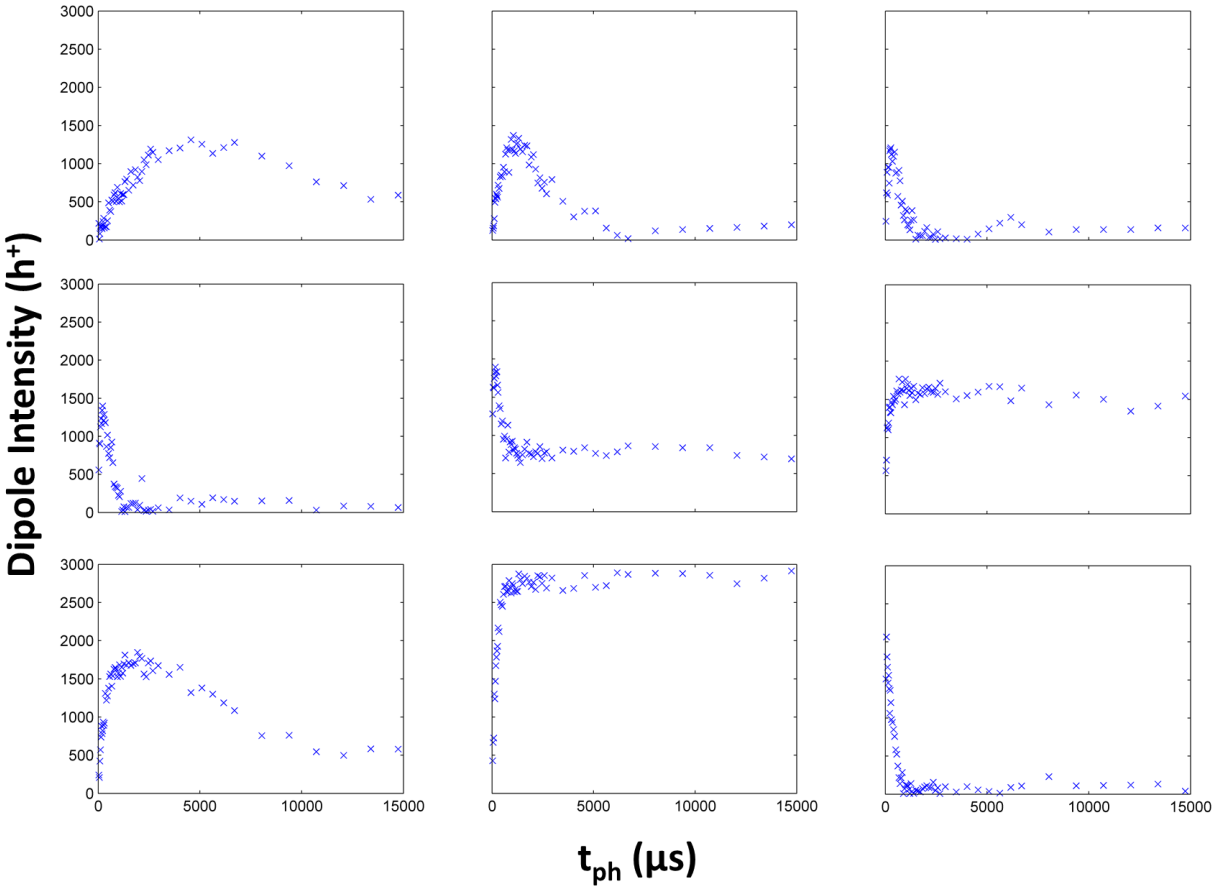

Figure 5.7 – A selection of the observed signal dipole intensity curves. The top middle curve represents a good example of a "regular" curve as expected from a single defect beneath a particular clock phase.

5.3 – Trap properties in a proton irradiated p-channel CCD

The overall results (including measured emission time constants and estimated energy levels) are summarised in Table 5.1. The emission time constant distributions are shown in Figures 5.8 and 5.9 for the two temperature sets 149-159K and 172-180K respectively. Note that in Figure 5.8 and all emission time constant histograms throughout this thesis the binning is logarithmic. The results at each temperature will now be discussed in greater detail.

Temperature (K)		No. of defects		Main τ peak (μs)		Secondary τ peak (μs)		Energy (eV)
149		14716		40-100				0.19-0.23
154		14065		25-65				0.19-0.23
159		13324		12-35				0.19-0.23
172		1818		150-450		2000		0.29-0.33
176		1646		120-290		1250		0.29-0.33
180		1349		80-170		750		0.29-0.33

Table 5.1 – Summary of the results from the trap-pumping analysis at each temperature.

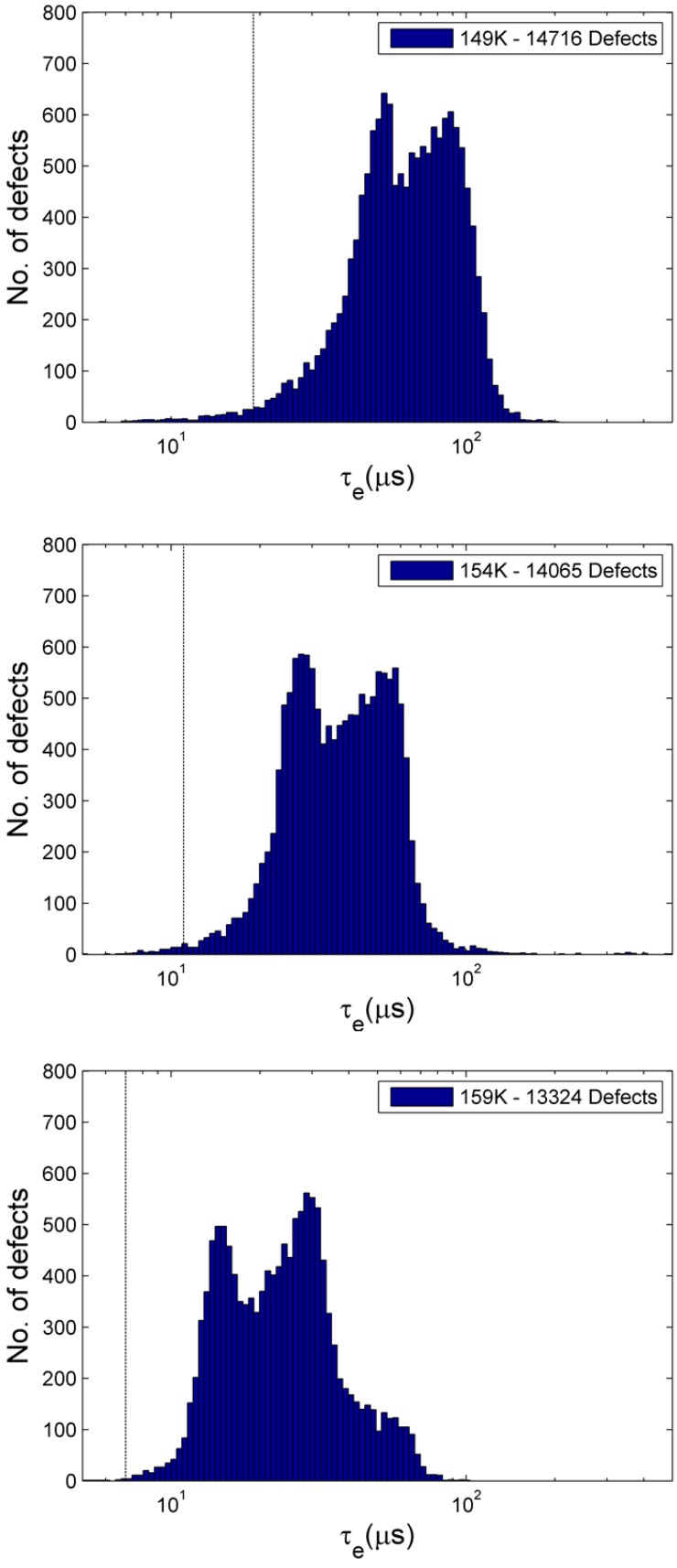

Figure 5.8 – Defect emission time constant distributions at 149, 154 and 159K (top to bottom). The black line shows the expected divacancy emission time constant at each temperature as from Figure 5.1

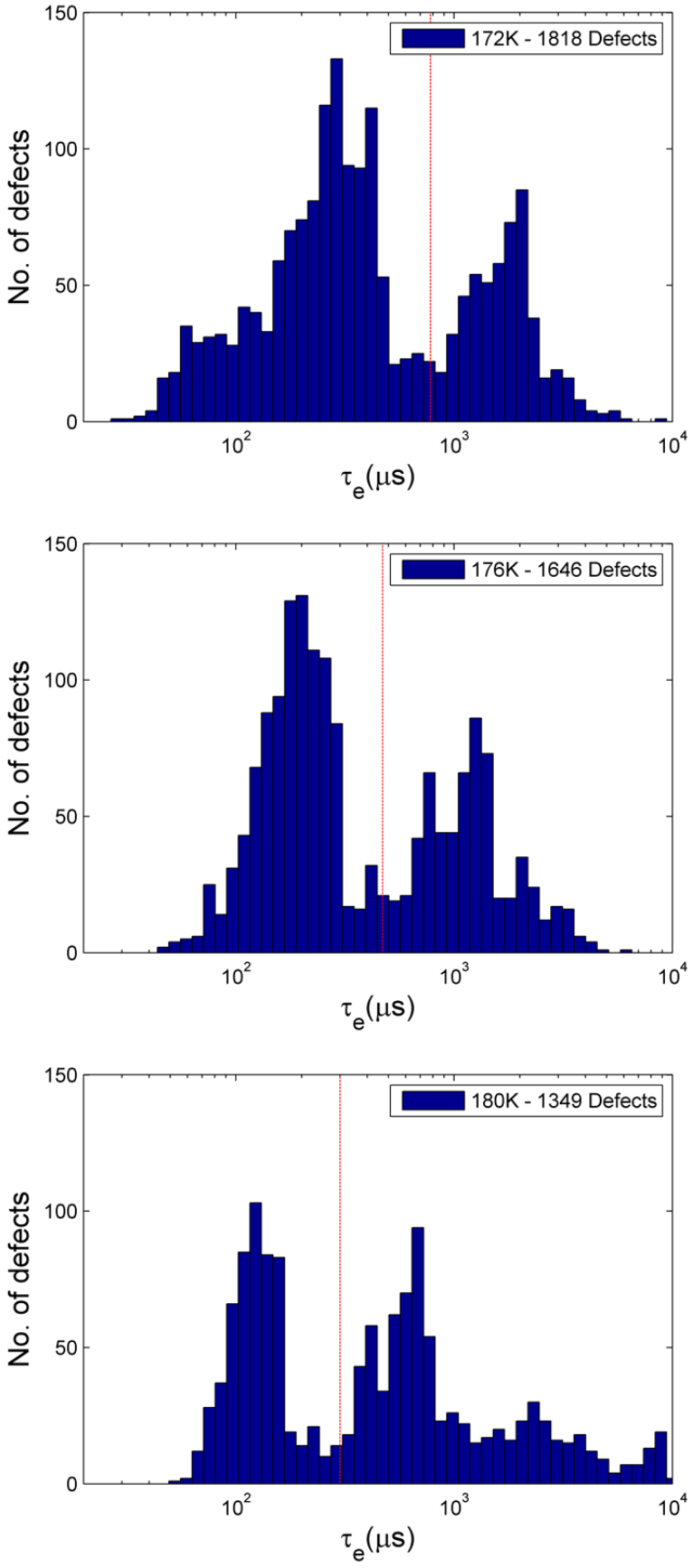

Figure 5.9 – Defect emission time constant distributions at 172, 176 and 180K (top to bottom). The red line shows the expected emission time constant for the carbon interstitial as from Figure 5.1.

5.3.1 – The donor level of the divacancy (149-159K)

By producing images using a phase time range of around *1-200 μs* over the temperature range 149-159K the donor level of the divacancy can be probed, since it should produce signal dipoles under these conditions. Figure 5.10 shows an example of the signal dipole intensity curve for the same defect at each tested temperature. The effect of temperature on the shape of the curve and the emission time constant can be seen clearly, with the peak in the dipole intensity curve decreasing in time as the temperature rises. For each defect producing curves such as those in Figure 5.10 the emission time constants were analysed from the SRH fit.

At 149K a total of 14716 defects were found and fitted successfully. It can be seen in Figure 5.8 that the emission time constant distribution at 149K has a split peak, with two approximately Gaussian distributions which overlap. The two peaks are found at around *53 μs* and *89 μs*, with the overall range at FWHM *40-100 μs*. At 154K there are 14065 defects found, suggesting that as temperature has increased some of the fastest defects have moved out of the range of the technique. The emission time constant distribution shows the same shape as the distribution at 149K, with two discernible peaks at around *54 μs* and *28 μs*. The emission time constant distribution at 159K again shows a similar shape to the other temperatures, with an even more pronounced split-peak structure. The overall emission time constant range is approximately *12-35 μs* with peaks at around *15 μs* and *29 μs*. The trend of fewer defects with rising temperature is continued, with 13324 within the tested range. As a comparison with literature, a study by Gow found that for a p-channel CCD204 at 153K the CTI falls as the transfer time rises from *10 μs*, before falling to almost zero as the transfer time reaches *100 μs* (Gow, 2012). If it is assumed that defects with emission time constants of the order of several transfer times are the worst case for CTI (Massey, 2010) then the distribution seen in this study at 154K would appear to generally support this. There is a peak in the distribution at around *55 μs* with the number of defects falling away quickly after this point.

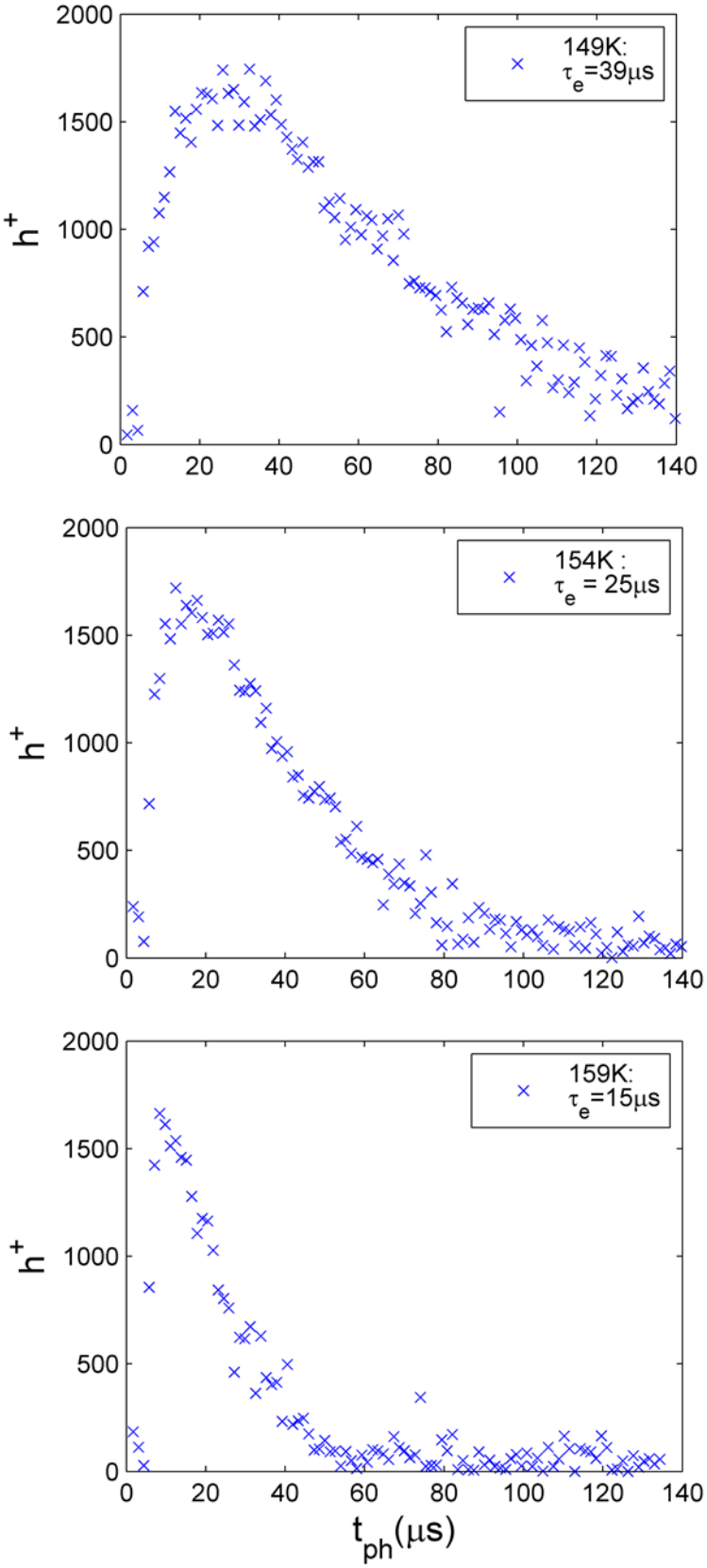

Figure 5.10 – The signal dipole intensity curve for the same defect at 149, 154 and 159K (top to bottom). The effect of temperature increase can be seen, with the peak in the intensity moving from right to left (indicating the defect getting faster).

The shape of the emission time constant distributions is interesting since at all three temperatures there is considerable spread and the existence of two clear individual peaks. As discussed previously at several points throughout this thesis a spread in the measured values is expected from the effects which are contained within the capture probability; such as local field variations, lattice strain, sub-pixel positioning of the defect etc. However again it is stressed that these are genuine effects and that the measurement uncertainty is negligible in comparison (see Chapter 8 work on emission time constant stability with repeat measurements). The existence of such a consistently large spread is an interesting result with potentially important consequences for device optimisation and damage mitigation. With respect to the observation of a split-peak distribution this is an important finding of this work albeit one which at the time of writing was not yet fully explained. This effect is seen in some form for both p-channel and n-channel (see Chapter 7) devices as well as for several different defect species. One would not expect to find defects with such comparable emission time constants at a given set of experimental conditions; all known defect levels which hinder charge transfer in CCDs are spaced far apart in the bandgap (see Figure 5.1 as an example). The energy and cross-section analysis outlined in the next section also refutes the possibility of two separate defects. One possibility which was discussed was a link between dipole orientation (light or dark pixel first) and emission time constant, however when analysed individually both the distribution of light-pixel first and dark-pixel first signal dipoles showed split-peak behaviour and so this was ruled out. Other potential sources of a split-peak are the combining effects of other defect species (either non-charge trapping or too fast/slow to affect CCD readout directly, or the interaction of the electric fields present within the CCD.

Since the writing of this thesis further work has been carried out to describe the split-peak distribution, and it observed that it arises due to the capturing of charge in the interphase regions of a CCD during readout. It had been assumed that the transfer of charge from one phase electrode to the next occurred quickly enough for trapping in interphase regions; however this does not appear

to be the case. A model has been developed (Skottfelt, 2018) which successfully explains the observed defect distributions and can lead to an improved methodology of trap-pumping in CCDs.

A total of 7211 defects were detected at all three temperatures. The top half of Figure 5.11 shows for each defect the emission time constant vs. temperature, along with the line from Figure 5.1 for the donor level of the divacancy. Again the large spread in the distribution is visible but the parallel nature of the individual lines (one line represents one defect tracked across the three temperatures) shows that measurement uncertainty is low and not the cause of the observed spread. This is seen more clearly in the lower half of Figure 5.11 in which the emission time constant lines for 100 random defects are plotted. Each of the lines in Figure 5.11 was fit based on SRH theory to give an estimate for the defect energy level and cross-section. The corresponding distributions are shown in Figures 5.12 and 5.13 respectively. The energy distribution shows a single Gaussian peak, which indicates the presence of a single defect species, despite the double peaks observed in the emission time constant distributions. The energy level is observed as:

$E = (E_v + 0.21 \pm 0.02)\ eV$

Where the uncertainty comes from the width of the overall distribution. The uncertainty on each individual energy measurement is low, of the order of *0.005 eV*, since the emission time constants are found to a high degree of accuracy and the fluctuation of the temperature is minimal. With reference to the divacancy with oxygen, which is expected to demonstrate an energy level of *E=(Ev + 0.24) eV*, no evidence can be found of any grouping about this point. We therefore state that at temperatures of 149-159K the single defect of importance in the transfer time range up to several hundred microseconds is the donor level of the silicon divacancy, with an energy level of:

E = (Ev + 0.21±0.02) eV.

A similar situation is found for the cross-section, where again the distribution shows a Gaussian peak with following range:

$\sigma = (0.2 – 2)\ x10^{-19} m^2$

Both the energy and cross-section distributions show considerable spreading. Again this could be in large part due to the CCD conditions such as the local electric field, or due to small structural differences around a defect within the lattice. It is an interesting result in the context of defect characterisation for image sensors that certainly for the case of the CCD at least, defect parameters show a large spread around a mean value which is genuine and not the result of any measurement uncertainties. This has the potential to limit the effectiveness of correction techniques requiring precise defect knowledge. Comparing the energy and cross-section results with the values found in Mostek, both agree within uncertainties. However the energy level of *0.184±0.012 eV* found by Mostek is at the low end of the range found in this study. One possible explanation is that the fastest defects (and so those with energy closest to the band edge) are too fast to appear at the highest temperature tested, and so the energy level observed is a slight over-estimation. The energy and cross-section values are a in general agreement with the values found by DLTS studies outlined in Chapter 2 (Kimerling, 1977, Hallen, 1996, Eremin, 1999).

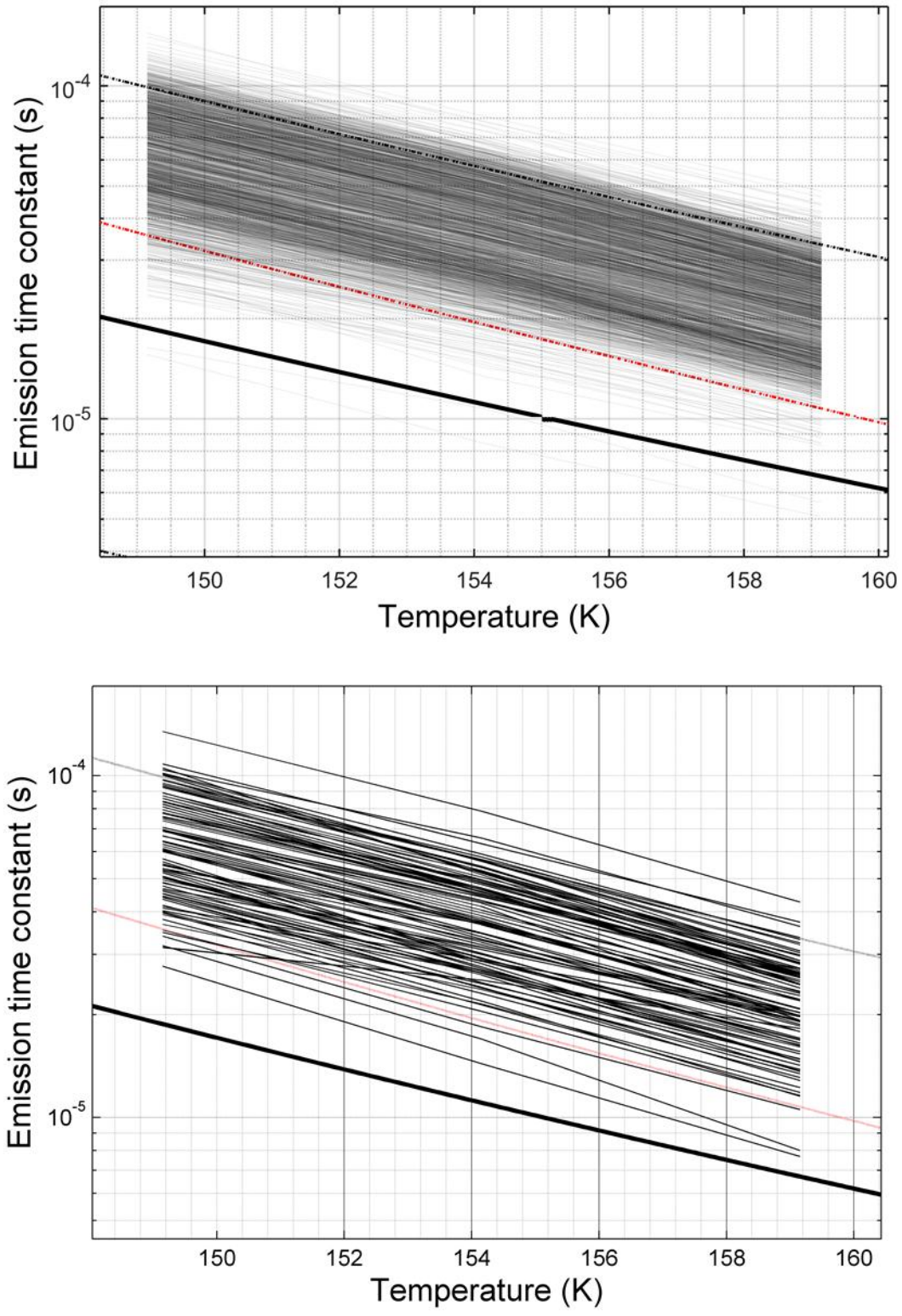

Figure 5.11 – The defect emission time constant vs temperature for defects found at all three tested temperature 149-159Ks, along with the theoretical emission time constant curve from Figure 4.1. Top: all defects. Bottom: a selection of 100 random defects. The parallel nature of the lines for each defect suggests a low measurement uncertainty.

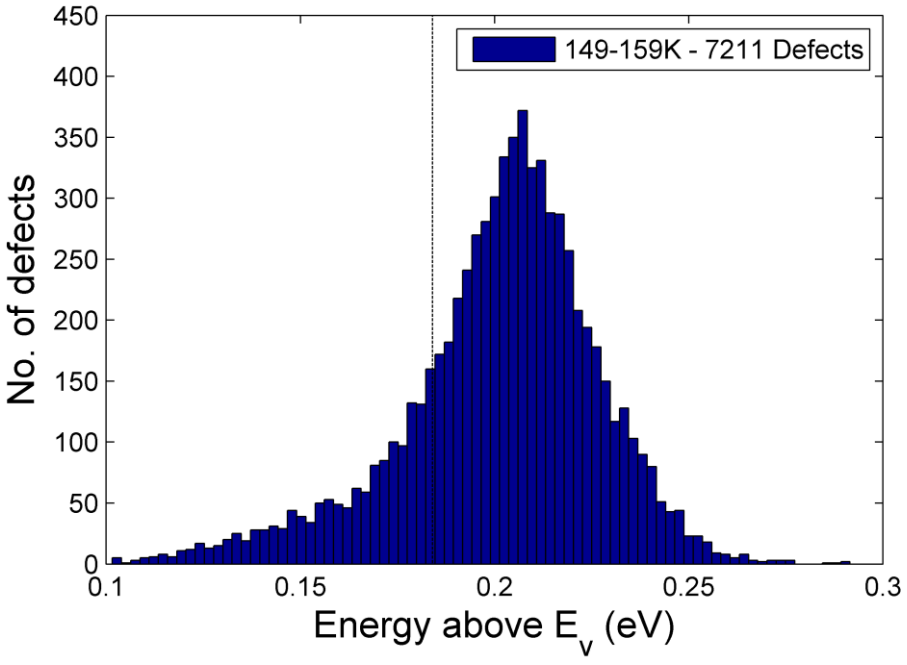

Figure 5.12 – The energy level distribution for defects which were observed at all three temperatures between 149-159K. Also shown is the value for the donor level of the silicon divacancy from (Mostek, 2010).

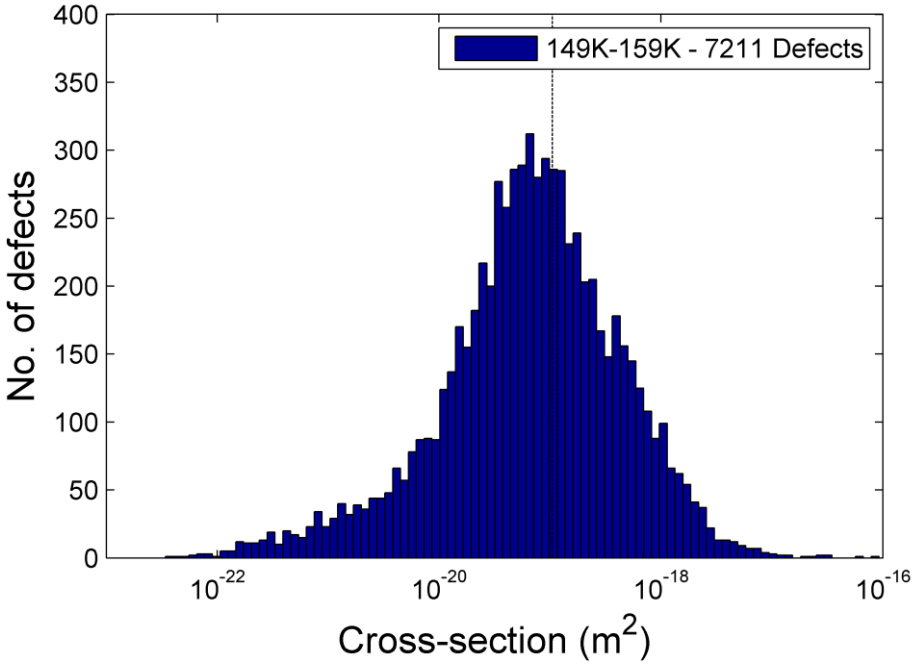

Figure 5.13 – The cross-section distribution for defects which were observed at all three temperatures between 149-159K. Also shown is the value for the donor level of the silicon divacancy from (Mostek, 2010).

5.3.2 - The carbon interstitial defect (172-180K)

A temperature range of 172-180K was chosen to probe the carbon interstitial defect. The phase-time range was increased to approximately *1-15000 μs* over a range of between 57-130 images, providing enough data-points and resolution for successful fitting of the slower carbon defect curves. At these temperatures the divacancy defects should be too fast to interfere with the signal charge. Exactly the same process was carried out as for the temperatures 149-159K, with again a selection of the images used for dipole detection in order to cover the entire phase-time range.

The first noticeable difference between the results from 172-180K are that there were fewer defects found at each temperature than for the range 149-159K. In total 1818 defects were found at 172K, 1646 defects were found at 176K and 1349 defects were found at 180K.

At 172K the emission time constant distribution shows two clear, separate, approximately Gaussian peaks, at around *290 μs* and *2000 μs*. The ratio of the number of defects in each peak is around 2:1. Overall there is a broad range of defect emission time constants across the whole phase-time range. At 176K the two peaks are at *200 μs* and *1250 μs* again with a ratio of 2:1. At 180K the two peaks are at *120 μs* and *700 μs*, with a ratio closer to 3:2 as some of the fastest defects move out of range. The overall shape of the distributions is similar to that of the divacancy distributions; however there is now a clearer gap between each peak.

A total of 880 defects were found across all three temperatures. The emission time constant vs temperature for each defect is shown in Figure 5.14. Again there is a large spread in the overall distribution, however the lines for each individual defect do not show much fluctuation and run mostly parallel to each other suggesting that the measurement uncertainty is negligible in comparison to the overall spread of the distribution. For each of the 880 defects, energy and cross-section values were calculated from a SRH fit of the lines in Figure 5.14. The distributions are shown

in Figures 5.15 and 5.16. Both display a single Gaussian peak, indicating the presence of a single defect species.

The energy level is given as:

$E = (E_v + 0.31 \pm 0.02)\ eV$

and the cross-section as the range:

$\sigma = (1 - 4)\ x10^{-18}\ m^2$

Both of these values are consistent within uncertainties with the carbon interstitial defect, as found by Mostek as well as several DLTS studies (Mooney, 1977, Frederickson, 1989, Londos, 1989). The energy level found is slightly high in comparison to the literature value which is again possibly due to the omission of some of the fastest defects as in the divacancy case. However the method has shown to produce accurate emission time constant results and reasonable values for both defect energy levels and cross-sections in the context of a CCD. It is shown that the single dominant defect species of relevance over the time range up to several thousand microseconds at 172-180K is the carbon interstitial defect.

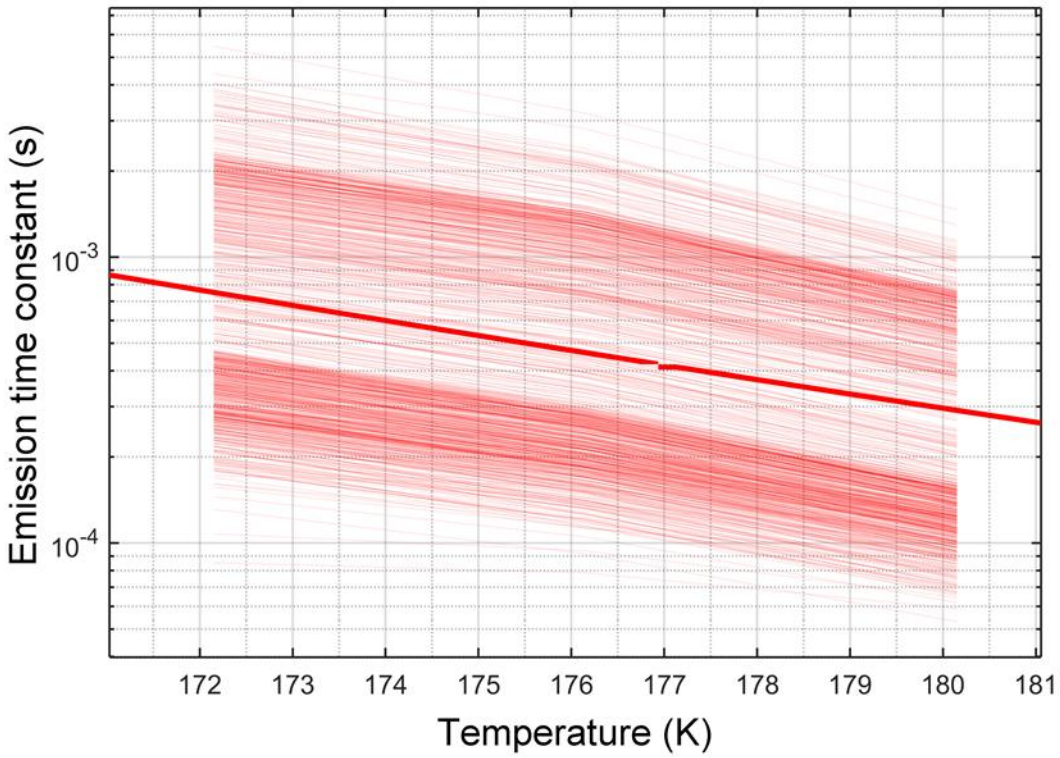

Figure 5.14 - The defect emission time constant vs temperature for defects found at all three tested temperatures 172-180K, along with the theoretical emission time constant curve from Figure 4.1.

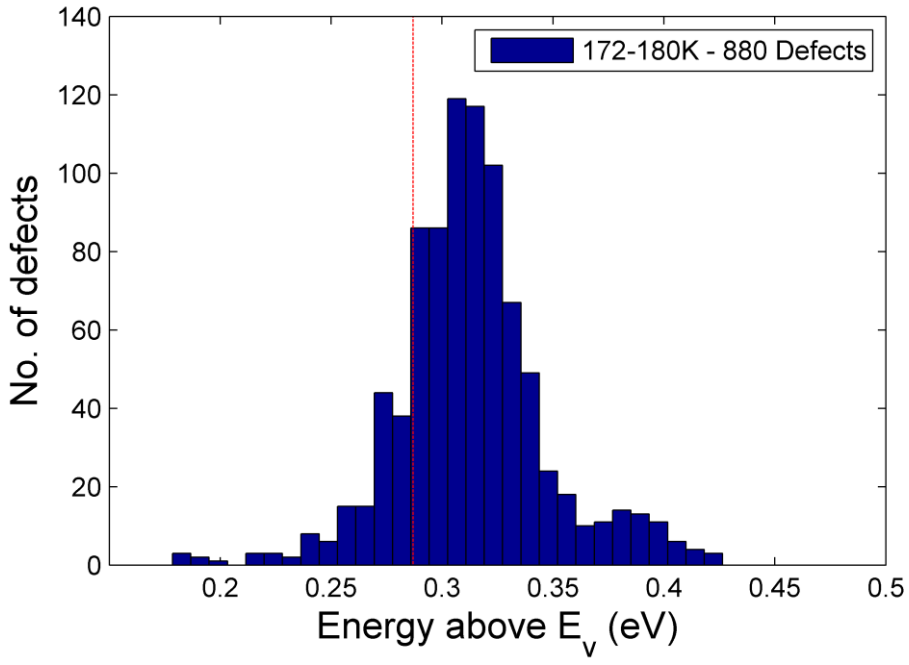

Figure 5.15 – The energy level distribution for defects which were observed at all three temperatures between 172-180K. Also shown is the value for the carbon interstitial defect from Mostek (2010).

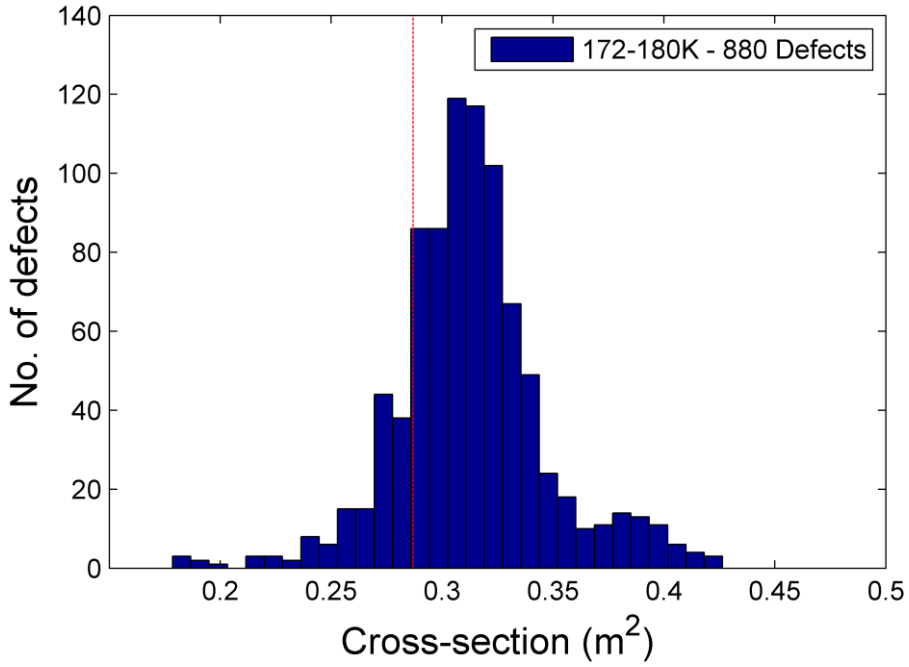

Figure 5.16 - The cross-section distribution for defects which were observed at all three temperatures between 172-180K. Also shown is the value for the carbon interstitial defect from Mostek (2010).

5.3.3 – Comparison of defect parameters

The results for both temperature sets indicate that a single defect species was observed, with the energy level and cross-section distributions showing a single Gaussian peak. The defect emission time constant distributions however showed more complex shapes, with two clear peaks often visible due to the capture of charge in the interphase regions of the CCD (Skottfelt, 2018). Figure 5.17 shows for each temperature set a 2d histogram of the emission time constant for a given defect against the calculated energy level for that defect. For both defect species the grouping of the emission time constant data can be seen, however no such groupings are observed in the defect energy levels.

The spread in energy levels seen for defects within a CCD can have important consequences for device performance. In work by Maneuski the CTI was modelled as a function of defect energy, and it was shown that for a given clocking rate an energy level difference of *0.1 eV* can have an order of

magnitude effect on the CTI at certain temperatures (Maneuski, 2008). In this study we see a FWHM energy range of around *0.05 eV* so this has to be accounted for. The dependence of CTI on defect energy level will depend on temperature and clocking rate; however it is further evidence that in the case of a CCD there are "worst case" defects for a given set of operational conditions, and that methods such as trap-pumping are important for identifying optimum conditions.

5.4 – Summary

A p-channel CCD irradiated with protons to a 10 MeV equivalent fluence of $4x10^{9}\ p\ cm^{-2}$ was analysed using the method of single trap-pumping with the aim of studying two important hole-trapping defects in CCDs; the donor level of the silicon divacancy (across the temperature range (149K-159K) and the carbon interstitial defect (across the temperature range 172-180K). A large number of defects were observed for both temperature sets and defect emission time constant distributions were constructed. A large spread in emission time constant distributions was observed for both defect species which does not arise from measurement uncertainty, as indicated by the stability of the emission constant relationship with temperature for each individual defect. The effects of local variations in temperature, electric field and stress/strain all likely contribute to this spread, which is observed consistently at all temperatures. Also observed was the presence of a split-peak in the distributions, despite strong evidence from the energy level estimates that only a single defect species was observed across each temperature range. Since defects are studied under CCD conditions it was assumed likely that this was a CCD effect, however the true explanation was unknown until after the writing of this thesis, when further work has shown it to be an effect of charge trapping in the interphase regions of CCDs (Skottfelt, 2018). This can leads to improved trap-pumping and damage mitigation models for CCDs.

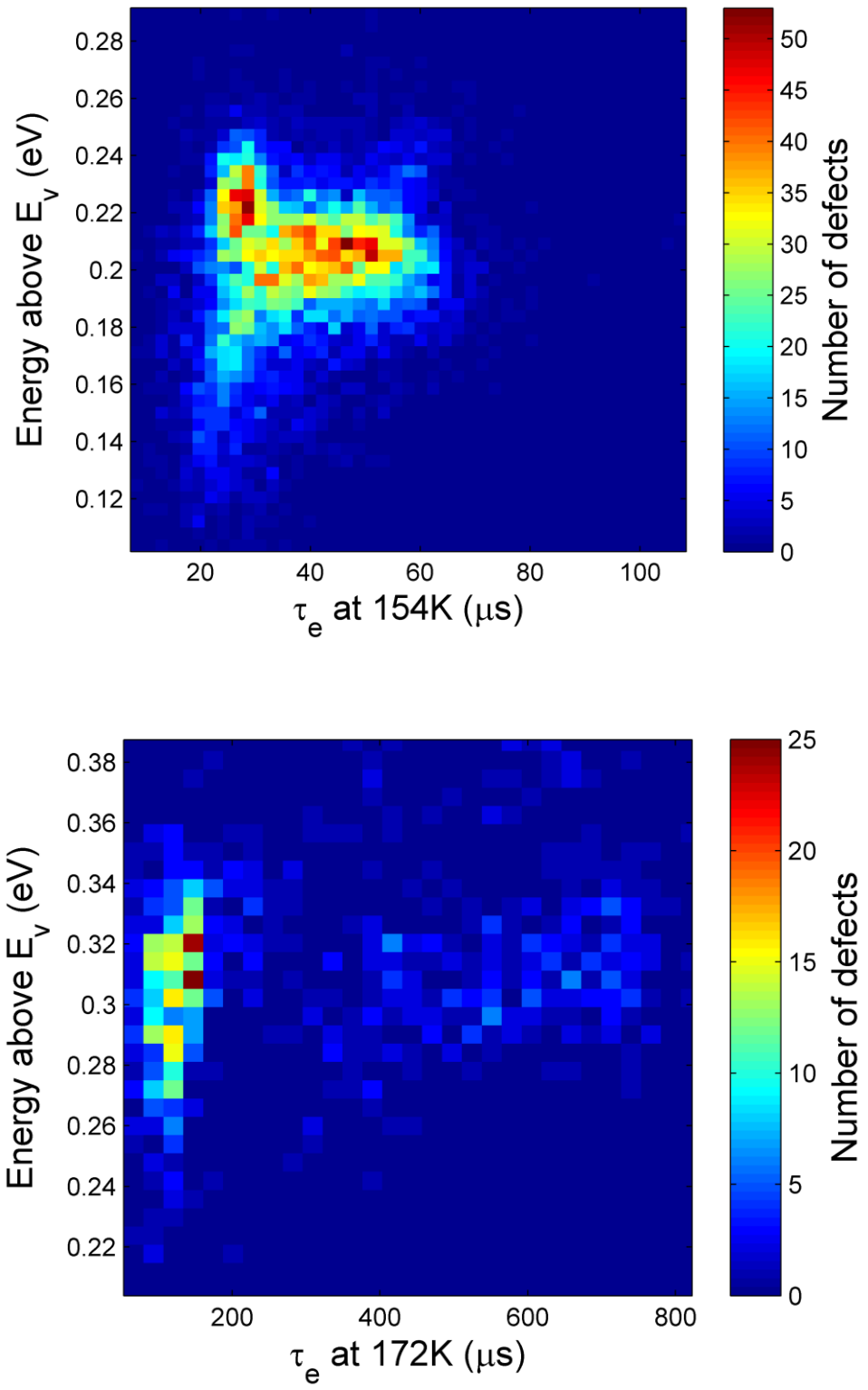

Figure 5.17 – A 2D histogram showing the measured defect emission time constant against the calculated energy level for all defects found at 154K (top) and 172K (bottom). The grouping of the emission time constants can be seen more clearly.

From the energy level and cross-section estimates the two observed defect species are those which were expected; the donor level of the silicon divacancy with an energy level of $E = (Ev + 0.21 \pm 0.02)\ eV$ and the carbon interstitial defect with an energy level of $E = (Ev + 0.31 \pm 0.02)\ eV$. Both of these results are consistent within uncertainties with the values quoted in the literature from various DLTS studies. Overall the trap-pumping technique has shown to be a reliable method of obtaining the accurate defect emission time constant data which is required if the science goals of future space-based CCD detectors are not going to be compromised by radiation damage effects. It has also provided good enough resolution to demonstrate the presence of a consistently large spread in the emission time constant data, as well as to uncover unexpected effects such as the split-peak distribution. Moving forward with the aims of this thesis this gives strong confidence in the technique and the results that it produces.

Chapter 6 – Cryogenic irradiation and subsequent room-temperature annealing of a p-channel CCD

In Chapter 3 the process of the formation of a defect state in an otherwise perfect crystal structure was described. The defects which are studied in this thesis are those which have been shown to affect the performance of silicon image sensors; however in general there exists a huge number of possible defect states of crystalline silicon, each with different properties and values of formation and activation energies. It follows that there is more than one distinct radiation-induced defect distribution possible within the same crystal; and so the properties of the silicon as it is irradiated become important. In this Chapter we focus specifically on the effect of the temperature during irradiation on the final defect distribution. Temperature is expected to have a significant effect on defect formation since it affects both the lattice energy (i.e. phonon energy) and defect mobility (Grove, 1967; Pichler, 2004).

The effect of temperature during irradiation is tested in this study on a p-channel CCD in the context of its use as a space-based detector. At present the standard process for determining the effects of radiation damage on a specific detector are to identify the likely radiation fluence it will receive during the mission lifetime (using tools such as SPENVIS) and then to test several comparable sensors by irradiating them with that same fluence over a much shorter-time period. This has shown to be an effective method in approximating the extent to which radiation damage is a concern for a given mission and whether further radiation hardening steps are required. However currently all pre-mission irradiation testing is carried out at room-temperature due to the cost and logistical difficulties of performing a cryogenic irradiation. As most space-based detectors operate at well below room-temperature there is a clear difference between the physical condition of the actual sensor as it receives radiation during operation and the sensors tested at room-temperature during development. Little has been done to study the effects of this difference within the context of the detector performance over time. In this Chapter we analyse a p-channel CCD irradiated at 153K and

then following several room-temperature anneal stages.

Much of the analysis in this Chapter was again performed using the method of single trap-pumping as discussed in Chapter 4. The advantages of this technique as a method of defect analysis have been outlined previously and make it a particularly valuable tool for investigating the evolution of defects over time since they can be studied on an individual basis. It is important however to again state the caveats of using this technique in the context of this experiment and its aims. Trap-pumping detects the defects which are interacting with a signal charge cloud as it moves through a CCD. Those defects which do not interact with the signal charge are not detected or analysed. This means of course that the charge cloud size and so the background signal level has an effect on the number of defects which are found; this is the subject of an investigation in Chapter 8. This also means that defects with emission time constants which are either too fast or too slow relative to the CCD pixel transfer rate are not detected. The consequences of this have been outlined previously however for the sake of this Chapter it is re-iterated that the analysis carried out subsequently is of those defects which affect signal charge (holes in the p-channel CCD case) as it is transferred through the CCD. For the purpose of radiation damage studies of imaging sensors for space applications and the potential radiation hardening of those sensors this is the vital information required; highly accurate defect parameter analysis of the defects affecting signal charge. However it does not present a comprehensive study of the process of defect evolution in silicon in general; since there will exist many defects which are not detectable for a given set of conditions.

6.1 – Cryogenic test campaign

The CCD model used for this study was a p-channel e2v CCD204, which was described in Chapter 4. The CCD204 is a variant of the original baseline sensor for the ESA EUCLID mission, the e2v CCD203. It consists of the same pixel and register structure with an added charge injection capability (see

Figure 5.2). A single CCD204 (referenced as the cryogenic device throughout this Chapter) was irradiated at a temperature of 153K using *7.5 MeV* protons at the Synergy Health *5 MV* Tandem accelerator facility in the UK. The device was partially irradiated to a total 10 MeV equivalent fluence of 1.24×10^9 *p cm*$^{-2}$ with a further area left unirradiated as a control. The device was biased and operational during the irradiation in order to reflect typical conditions in a space-based detector. A second CCD204 was partially irradiated at room-temperature (referenced as the RT device) at the same facility, to a 10 MeV equivalent fluence of 2.0×10^9 *p cm*$^{-2}$ and also contained a control region. It is important to note that this is not the same device that was tested in Chapter 5. These irradiations were performed as part of a larger study into a cryogenic irradiation of a CCD and only one section of each device was irradiated with the fluences given above. However these were the regions of the devices used for all of the work in this Chapter and so details of the other irradiation fluences are omitted here. A full explanation of the both the room-temperature and cryogenic irradiations is given in (Gow, 2015).

The predominant reason that cryogenic irradiations of CCDs are seldom performed is that they present a logistical challenge and the benefits have not previously been thought to outweigh the increased time and cost required. For the irradiation of the cryogenic device used for this work, a modified version of the vacuum chamber facility shown in Figure 5.5 was mounted to the beamline, as shown in Figure 6.1. The device was cooled using a Cryotiger cold end, with the temperature measured by a pt-1000 resistance thermometer attached to the CCD packaging and connected to a Lakeshore temperature controller. All biasing and clocking was performed with an XCAM camera system which also controlled the CCD output.

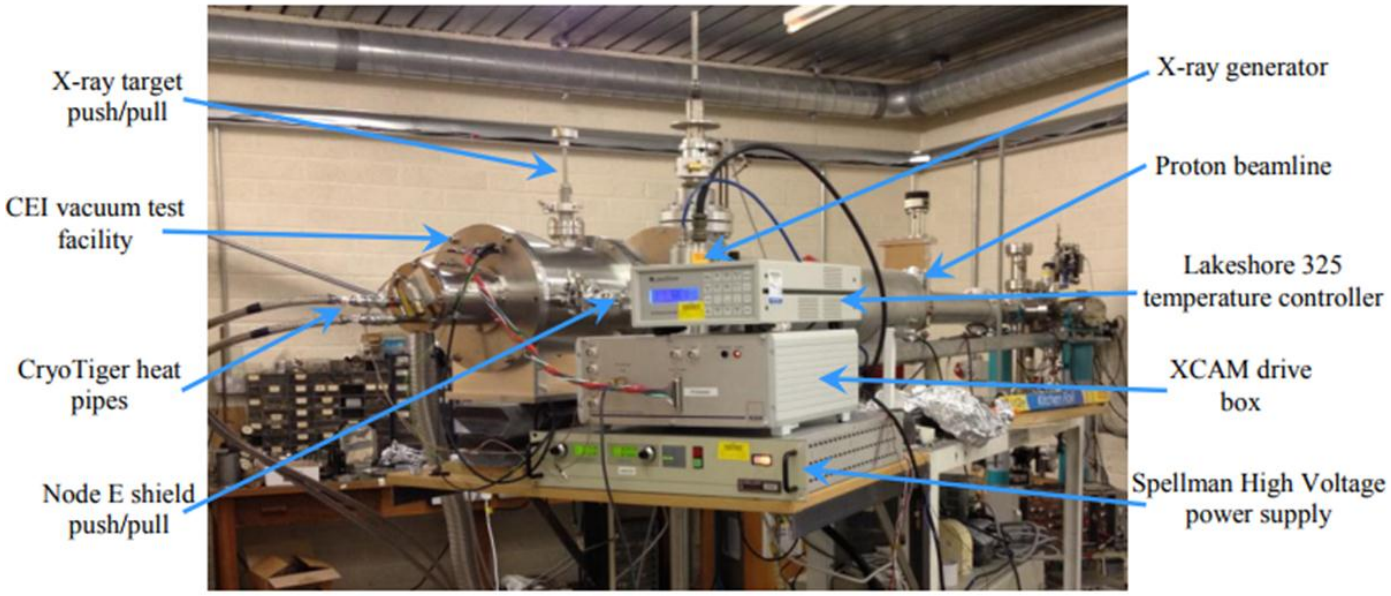

Figure 6.1 – A photo of the modified vacuum chamber test facility used for the cryogenic irradiation at Synergy Health 5MeV tandem accelerator facility in the UK (Gow, 2015).

Testing of the cryogenic device was carried out at 153K over a period of 7 days, before the first room-temperature anneal stage of 26 hours was performed with the device unbiased. This was followed by several further stages of testing and annealing as will be reported throughout this Chapter. A flow-chart is shown in Figure 6.2 outlining the timeline of the test campaign for the cryogenically irradiated device. All testing was carried out at 153K unless otherwise stated, and the device was held at 153K whenever it was not being annealed at room-temperature. The trap-pumping analysis was performed in much the same way as for the work in the Chapter 5, using the process which had been developed and shown to work reliably for single defect analysis. A threshold of 3σ either side of the background was used for dipole identification, with a fitting parameter limit of r>0.85 and flat-level curve removal as in the work of the previous Chapter. Each dataset consists of 160 trap-pumping frames, covering a large phase time range of approximately *3-30000* µs. This should allow for both divacancy and carbon interstitial defects to be detected if present at 153K. The images searched for signal dipoles corresponded to phase time values of approximately *30, 50, 100, 300, 500, 1000, 2000, 3500* and *5000 µs*. This covered the entire phase time range and allowed for

analysis of both defect species whilst keeping the time taken to run the analysis to a suitable level. The ROI selected for signal dipole detection and analysis was a 600x400 pixel region and is shown in Figure 6.3 which is a sample image from the cryogenic device at 153K. Signal dipoles were observed in both devices post-irradiation and an example of a number of the observed dipoles is shown in Figure 6.4 which is a section of a trap-pumped image from the room-temperature device at 153K.

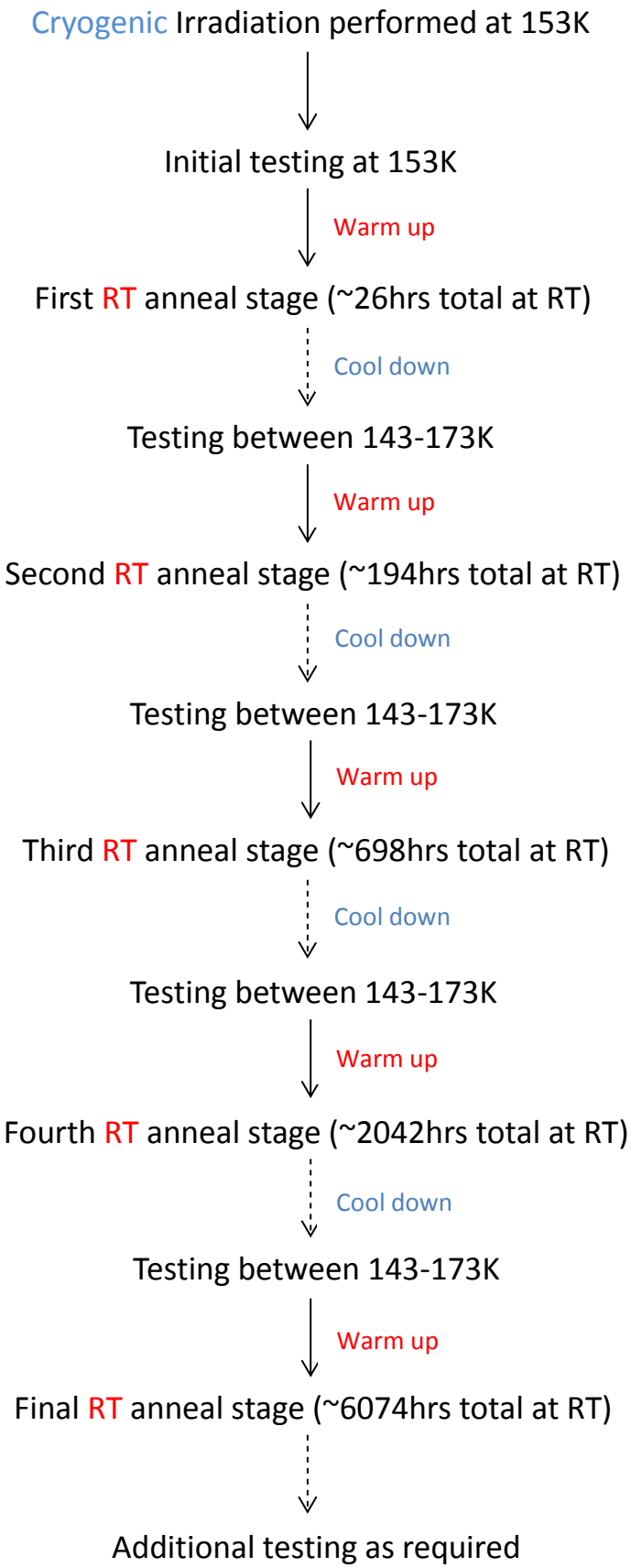

Figure 6.2 – A timeline of the test campaign for the cryogenically irradiated device. Initial testing occurred over a period of approximately two days after the irradiation, with the device maintained at 153K throughout.

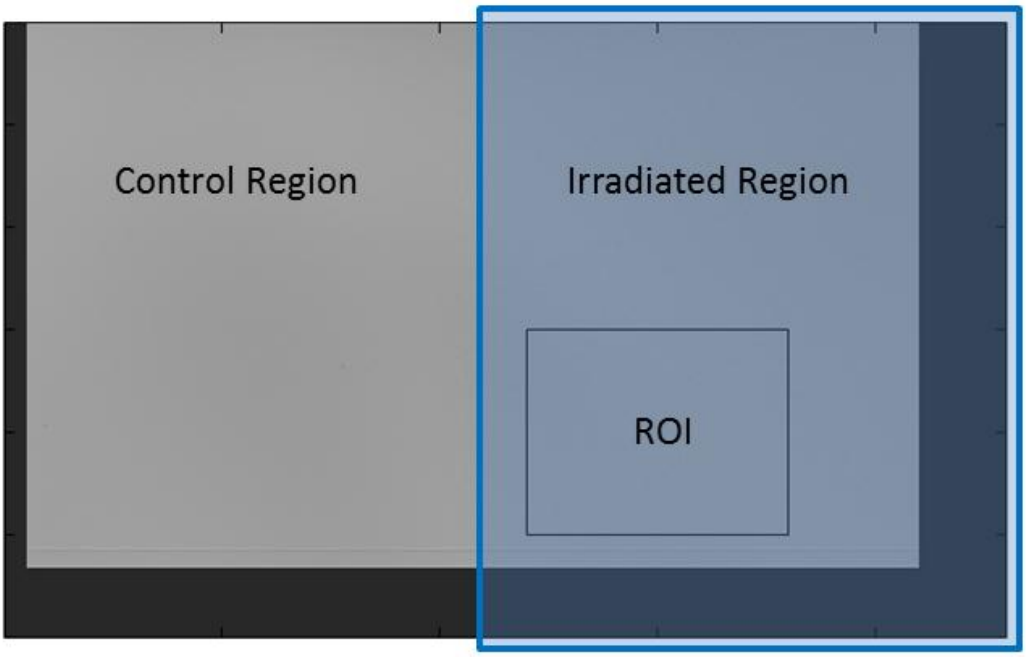

Figure 6.3 – An image from the a single node of the cryogenic device at 153K showing the irradiated region (blue area) and the 600x400 pixel ROI which was used for analysis. The same ROI was used for both devices.

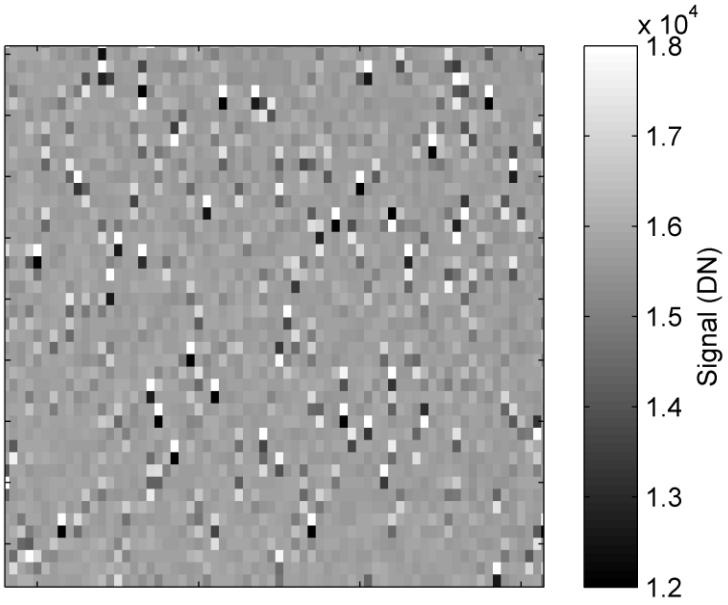

Figure 6.4 – An example of signal dipoles observed in the room-temperature device at 172K

6.2 – Room-temperature irradiated device

Analysis of the RT device was first completed at 153K, to provide a direct comparison to the cryogenic device. Added to the work of the previous Chapter this gives a large amount of information on the defects present in a RT irradiated device when tested at 153K. Analysis of the RT device was also carried out at 143K and 163K, giving enough data for an estimate of defect energy levels using the method outlined in Chapter 3. Figure 6.5 shows an array of typical signal dipole intensity curves from the RT device, including both the regular type curves which are desired for analysis and some of the other curve types which are as a result of the pseudo 3-phase pumping process with unequal clock phase widths. It can be seen from Figure 6.5 that many of the intensity curves correspond to a relatively fast defect species, indicating the likely presence of the donor level of the divacancy at this temperature.

The defect emission time constant histogram for the RT device at 153K is shown in Figure 6.6. It is dominated by a single peak at approximately *37 μs*. This corresponds to the donor level of the divacancy which is expected to be present at these temperatures (Zangenberg, 2002; Mostek, 2010). The emission time constant for both the donor level of the divacancy and the carbon interstitial defect, as taken from the energy levels and cross-sections reported by Mostek, is also shown in Figure 6.6 for comparison. Following similar analysis of the defect distribution at 143K and 163K, 3012 defects were found to appear at all three temperatures. This allowed for an estimate of the energy distribution, which is shown in Figure 6.7 along with the values reported by Mostek. A broad peak is seen ranging from around *0.15* to *0.25 eV* above the valence band edge. This could potentially correspond to a number of defect species however the distribution is grouped around the expected level for the donor level of the divacancy of *0.20 eV*. Therefore it is concluded that the defects seen are divacancy defects. There is no obvious second peak corresponding to a second defect species, particularly with respect to the carbon-oxygen defect at *0.24 eV*, and so we conclude

that for a device irradiated at RT by far the most predominant defect within the tested time range at 153K is the donor level of the divacancy.

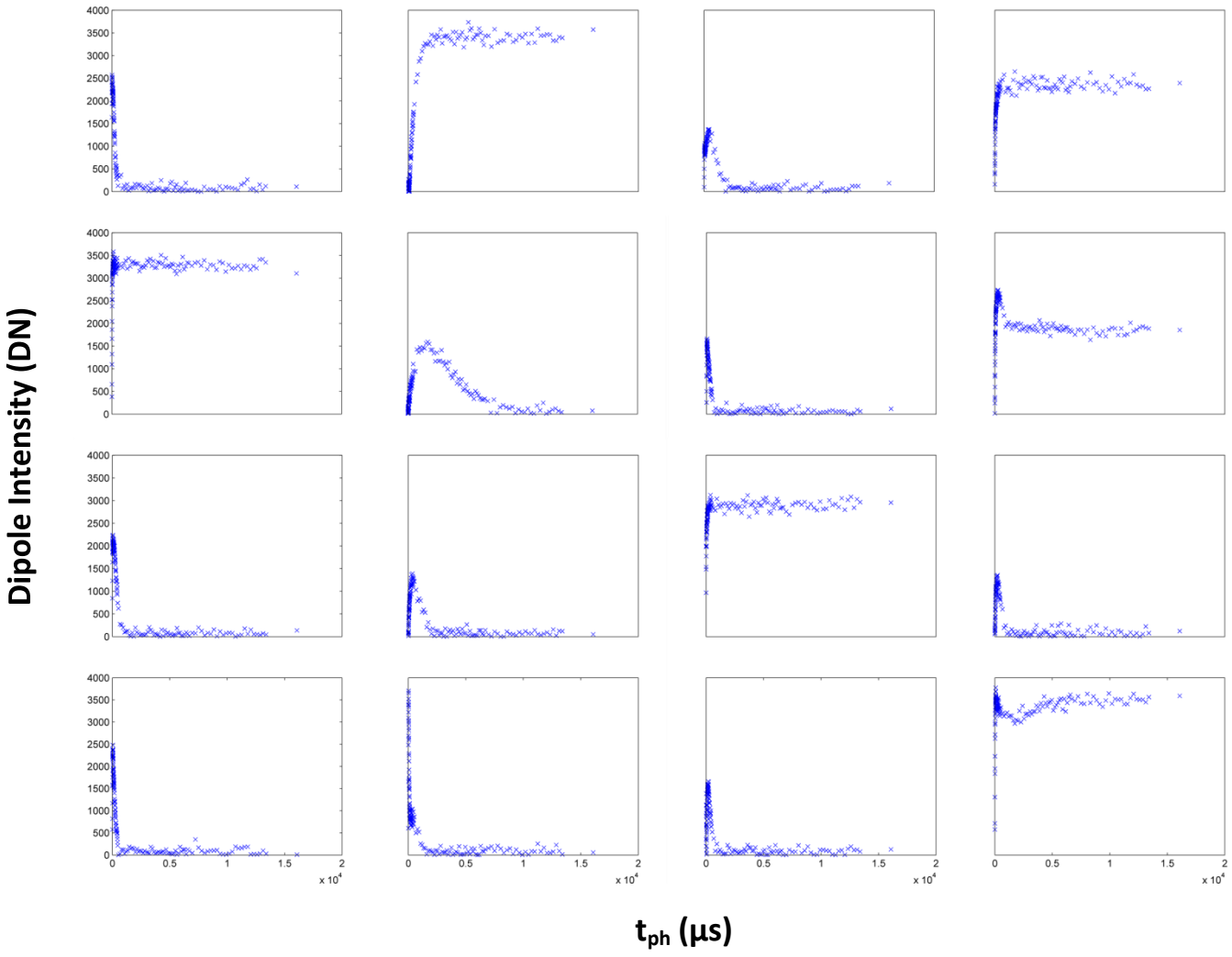

Figure 6.5 – A selection of typical dipole intensity curves at 153K from the RT irradiated device. The axes have been fixed to allow for comparison. A typical regular type curve is shown for example in the top left corner, and a typical flat-level curve is shown in the top right corner.

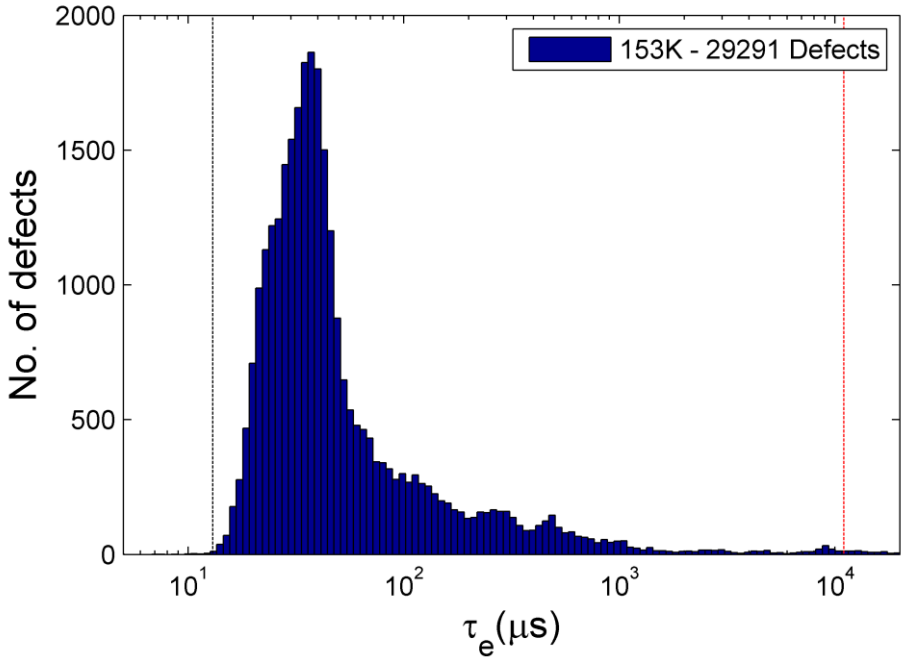

Figure 6.6 – The defect emission time constant distribution at 153K for the RT irradiated device. Shown also are expected values at 153K for the donor level of the divacancy (black line) and the carbon interstitial (red line).

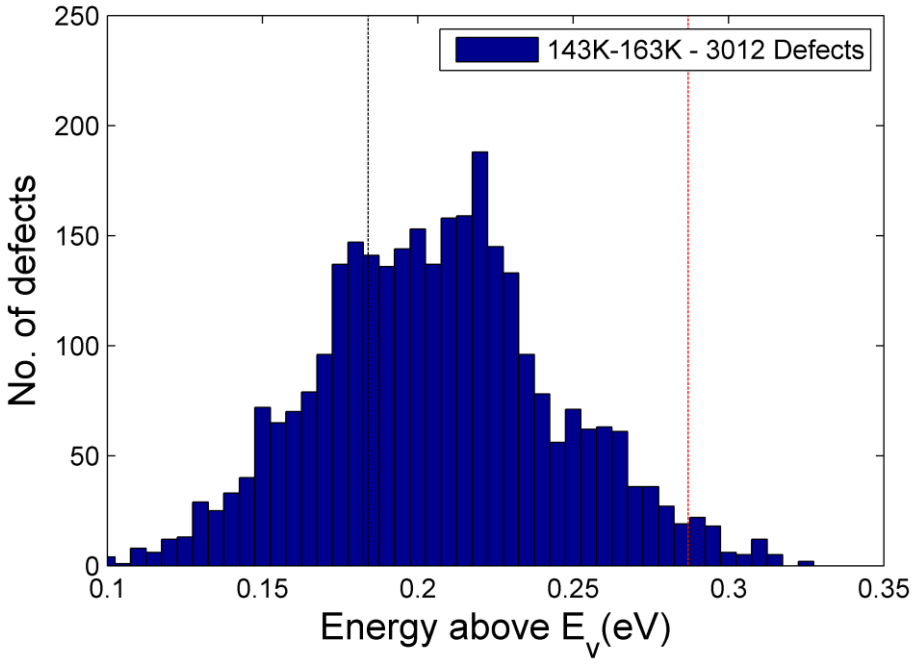

Figure 6.7 – The energy level distribution for all defects which are found to appear at 143, 153, 163K. Shown also are the theoretical values for the donor level of the divacancy (black line) and carbon interstitial defect (red line).

6.3 – Cryogenically (153K) irradiated device

Pre-anneal testing of the cryogenic device was carried out for the first few days after irradiation, with the device always held at 153K. As in the case for the RT device, a selection of the typical dipole intensity curves is shown in Figure 6.8. An initial observation from the selection of curves seen was a reduction in the number of flat-level or inverted curves in comparison to the RT device. Many of the curves also appear to peak at longer phase-time values, indicting an increase in the number of slower defects. The complete defect emission time constant distribution at 153K immediately post-irradiation is shown in Figure 6.9. Initial observations are a reduction by approximately a factor 4 in the number of defects overall, as well as the absence of a peak at the expected emission time constant for the divacancy. This is an important result, showing that the temperature during irradiation has significantly affected the defect formation. Again it is stressed that an overall reduction in defects is not certain, however it is observed for the tested phase-time values and so the range of importance when considering charge transfer in a CCD.

There are two small discernible peaks in the emission time constant distribution at approximately *60 μs* and *100 μs*, which suggests that there are still some divacancy defects present, in much reduced numbers. It is possible that these defects were present pre-irradiation, however fewer would be expected than are observed, going by the density in the device control region (see section 6.6). There are also a number of defects at slower time constants, with no real clear peak in the distribution. It is likely therefore that the situation is still dynamic at this stage, with no single stable defect species within the tested phase-time range. The reduction in the number of flat or inverted curves is explained by the lower defect density, since it is less likely to have multiple defects per pixel which interact with each other during the trap-pumping process. Due to time constraints with the wider study no additional temperatures were able to be tested prior to the first anneal. This would be an obvious inclusion for any further work, to allow for an estimate of the energy distribution. It is

however clear that the RT and cryogenic cases differ significantly at 153K, which is of importance when considering radiation testing and optimisation of CCD detectors for use in space and other harsh radiation environments.

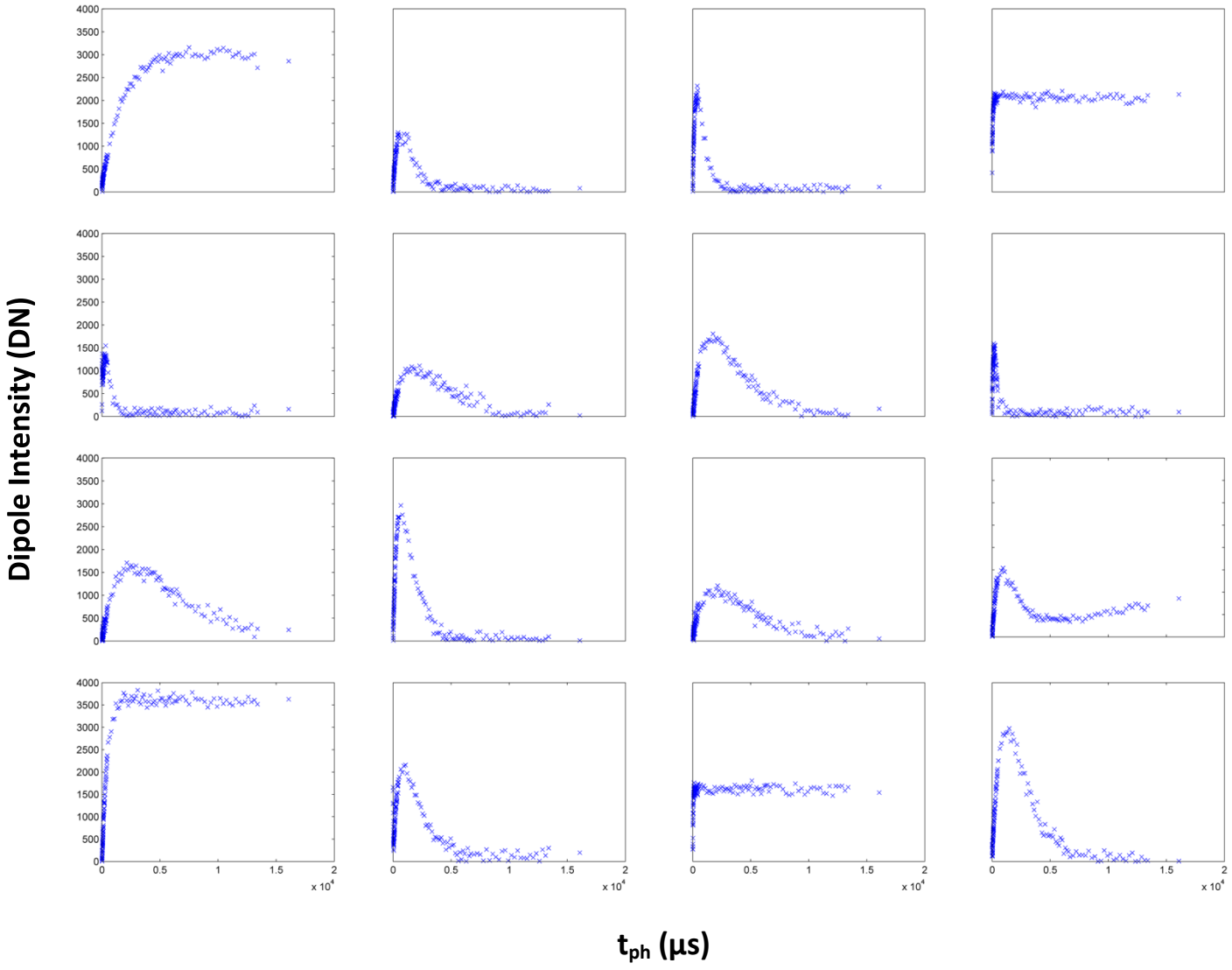

Figure 6.8 – A selection of typical dipole intensity curves at 153K from the cryogenically irradiated device. The axes have been fixed to allow for comparison.

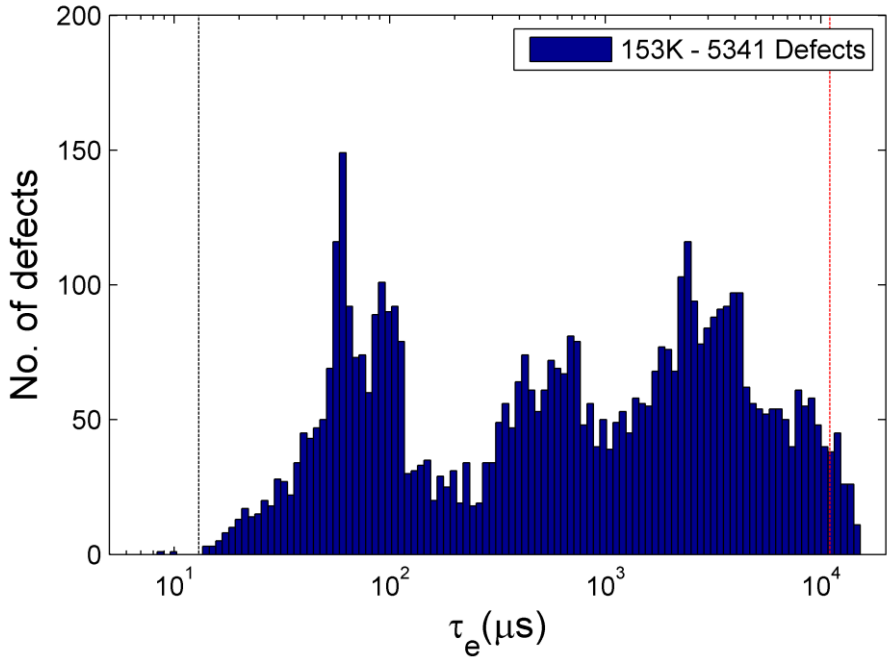

Figure 6.9 – The defect emission time constant distribution at 153K for the cryogenically irradiated device. Note the y-axis values are much smaller than for the RT device at 153K.

6.4 – Annealing (RT) studies

As outlined previously, the cryogenically irradiated device was annealed at RT over several stages, resulting in a cumulative total time of approximately 10 months. Table 6.1 outlines the anneal stages which were chosen and gives the approximate cumulative number of hours spent at RT by the device following each stage After each anneal a full trap-pumping analysis was performed, to analyse the effect of the temperature change on the defect emission time constant distribution. Each distribution will be presented and discussed individually, however Figure 6.10 shows in one figure all of the defect emission time constant distributions at 153K, with identical axes and binning. This allows for a clear observation of the defect evolution through each anneal stage. For comparison, the results from both the RT device and the cryogenic device post-irradiation are also included. The RT device results have been scaled by a factor 1.24/2 in order to account for the slightly higher proton fluence

received by this device. The results are also summarised in Table 6.3 at the end of this Chapter. The observations and results following each stage will now be discussed in detail.

Stage	Total time at RT (hrs)
Cryo PI	0
1 Day	26
1 Week	194
1 Month	698
3 Month	2042
10 Month	6074

Table 6.1 – The approximate total number of hours spent at RT for the cryogenic device at each testing stage.

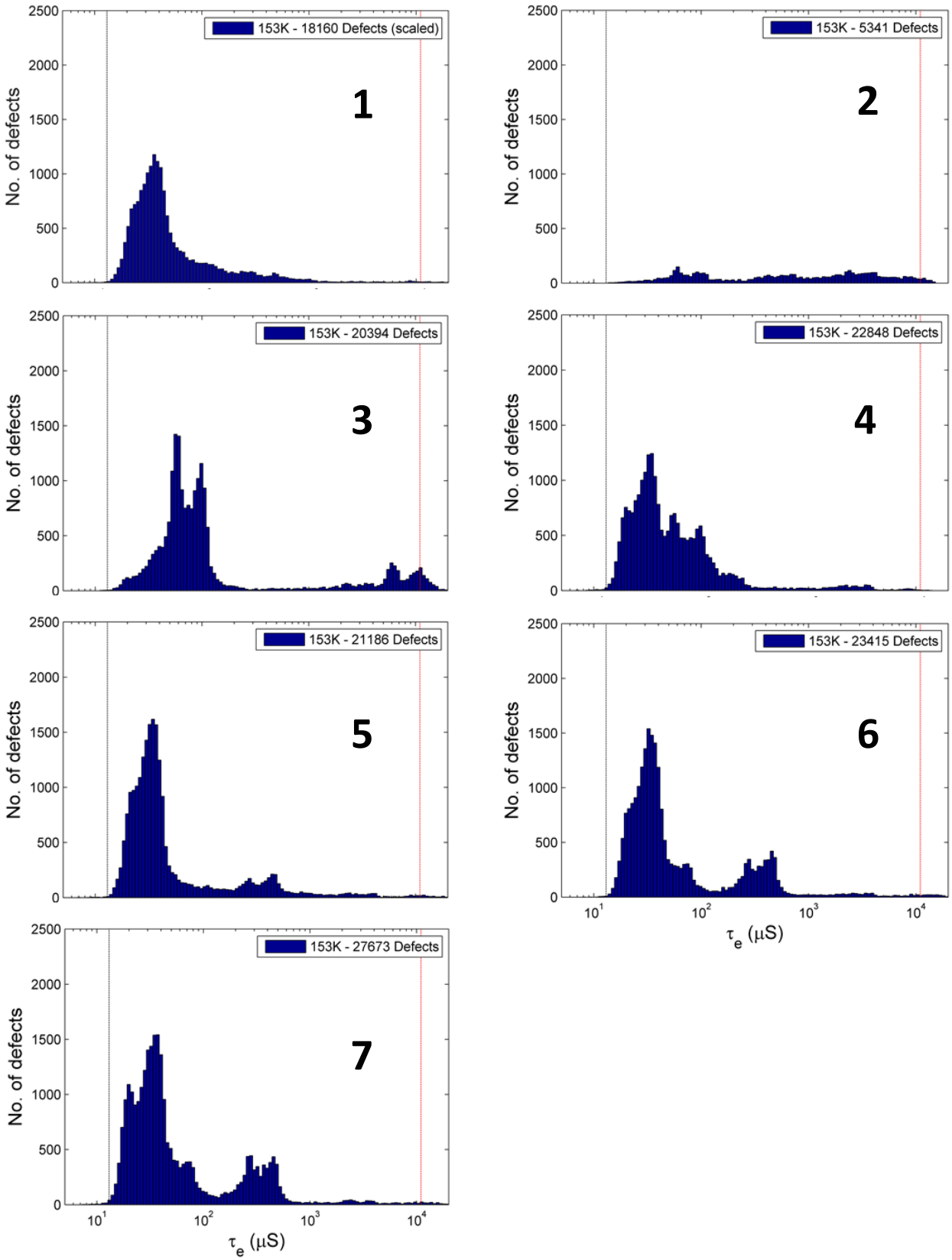

Figure 6.10 – The defect emission time constant distributions at 153K for every tested anneal stage. 1 - RT device (scaled to cryogenic fluence). 2 - Cryogenic device post-irradiation. 3 - 1-day anneal stage. 4 - 1-week stage. 5 - 1-month stage. 6 - 3-month stage. 7. – 10 –month stage. Also shown are the expected time constants at 153K for the divacancy (black) and carbon interstitial (red).

6.4.1 – 1 day (26-hr) RT anneal

Following the first anneal stage of 26 hours the device was cooled down to 153K and the defect distribution was analysed. The emission time constant distribution is shown in Figure 6.11. The total number of defects has increased by around a factor of 4, and there is now a clear peak around the expected divacancy emission time constant, although it is a split peak at around *57 μs* and *100 μs.* This corresponds to the small peaks seen in the distribution from the device post-irradiation in Figure 6.9; however there are now many more defects. This split emission time constant peak is also similar to that seen in the work of the previous Chapter. There are also two small peaks at around *10000 μs* which corresponds to the expected range for the carbon interstitial defect. It therefore appears as though both defects are present within the tested range after the first anneal. If we approximate all defects appearing found within the range *10-300 μs* as donor levels of the divacancy, then there are approximately 1900 present following the cryogenic irradiation and 17000 present following the first anneal stage. This increase of around 9x supports the result observed by Mostek. of an approximate 10x increase in serial CTI at 140K after RT anneal, using a serial transfer time of *1 μs* (Mostek, 2010). Under such conditions the donor level of the divacancy would be expected to be the dominant cause of CTI. Another study (Makarenko, 2009) using DLTS also observed an increase of the donor-level of the divacancy following anneal stages up to 280K after electron irradiation at 78K.

At this stage it was possible to test at three additional temperatures of 143, 163 and 173K. Every distribution for every temperature at each stage will not be presented as a Figure, however the four emission time constant distributions at the 1d stage are shown together in Figure 6.12, with fixed axes and binning. This has been included to show clearly the effect of temperature on emission time constant, as the peaks in the distribution can be seen moving to the left (i.e. defects getting faster) as temperature increases and emission from a defect level becomes more probable for a given time limit. It can be seen from Figure 6.13 that almost no defects appear at all four temperatures. The emission time constant is highly sensitive to temperature, with a complete removal of almost all

defects within a given time range possible for an increase of only a few Kelvin. This outlines the importance of correct optimisation for a given set of conditions, and the role that analysis methods such as trap pumping can play in such optimisation.

To generate energy level estimates, two separate three-temperature datasets were analysed. The energy level distributions for the 1d anneal stage are shown in Figure 6.13. A total of 8944 defects were found at all temperatures between 143-163K, and shows a dominant Gaussian peak with the energy level given as:

E = (Ev + 0.19±0.01) eV:

There is also a small number (~few 100) defects found with an energy level around *0.28 eV*. The second set of temperatures searched was 153-173K, with 3247 defects found at all three. The distribution shows large Gaussian peak with a value of:

E = (Ev + 0.29±0.02) eV

The two energy level values correspond to the values for the donor level of the divacancy and the carbon interstitial defect respectively, showing good agreement with both the work in the previous Chapter of this thesis and the results of DLTS studies. It is concluded that for a 1-day RT anneal of a p-channel CCD following cryogenic irradiation at 153K, both expected defect species are present, with the divacancy level dominant for the given phase-time range at temperatures up until around 170K. A large increase in the number of divacancy defects has been observed following the first anneal, demonstrating that they appear to be unable to form in large number over the timescale of a few days at 153K. It may be that the mobile monovacancies created by displacement damage do not on average have sufficient energy to form divacancy defects at this temperature and either remain or form other, less stable defects which do not affect readout at these operating speeds. This outlines

the significant effect of temperature on defect production and also immediately leads to a potential further study in analysis of a device irradiated cryogenically and then maintained at low temperature without subsequent anneal. It would be expected that the defect distribution in this case would eventually reach the same state as for the RT case, but the difference in timescales and any permanent differences would be of large importance particularly for space missions, where devices are usually operating at cryogenic temperatures constantly, but are characterised for radiation damage studies using RT irradiations.

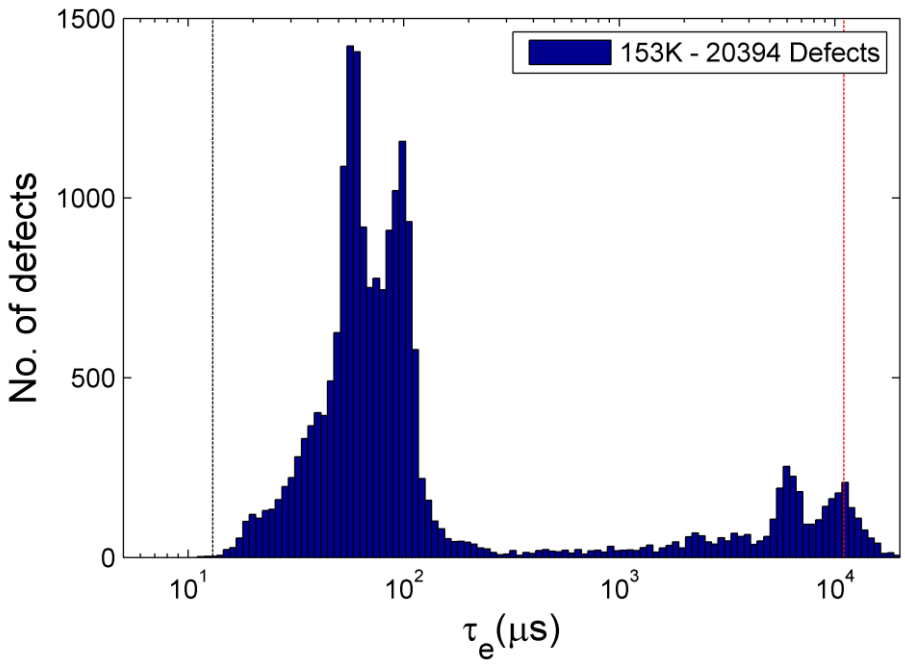

Figure 6.11 – The defect emission time constant distribution at 153K at the 1-day anneal stage.

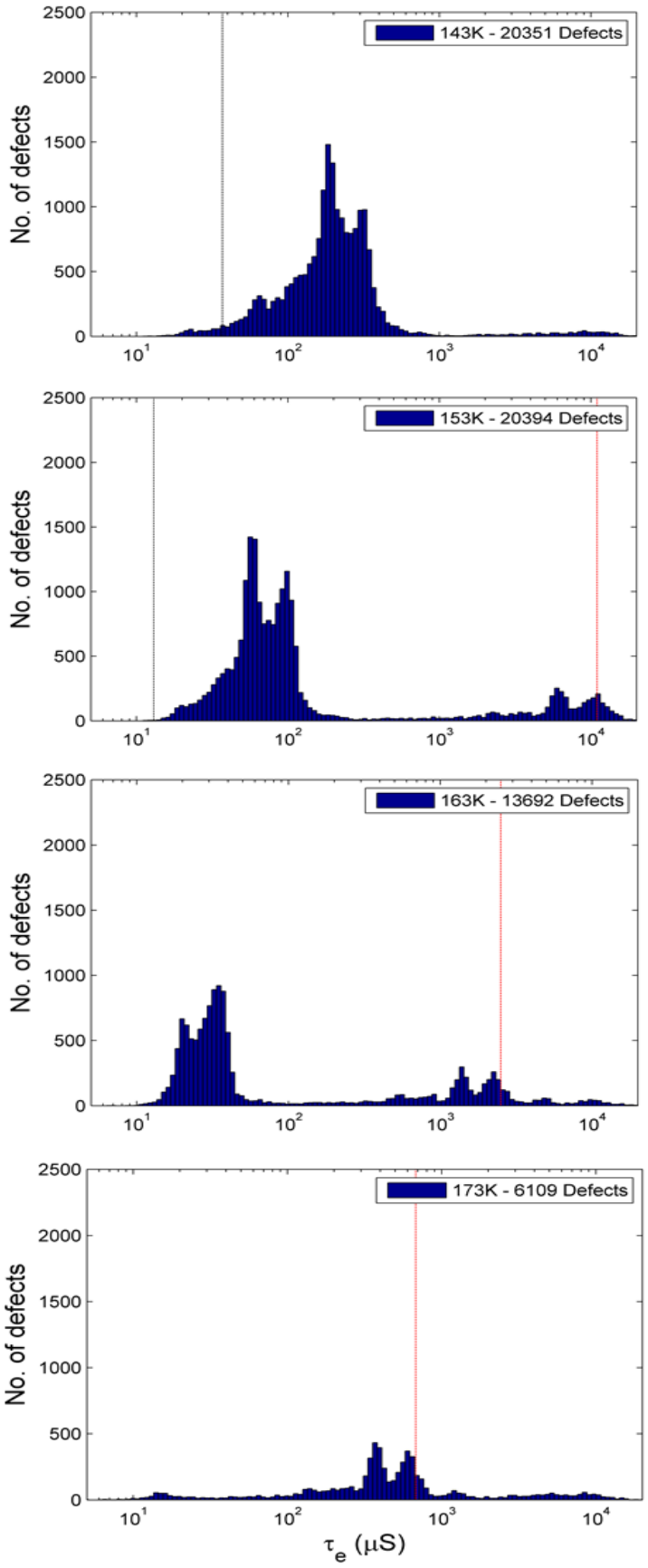

Figure 6.12 – The defect emission time constant distributions at 143-173K (top to bottom) following the first anneal stage.

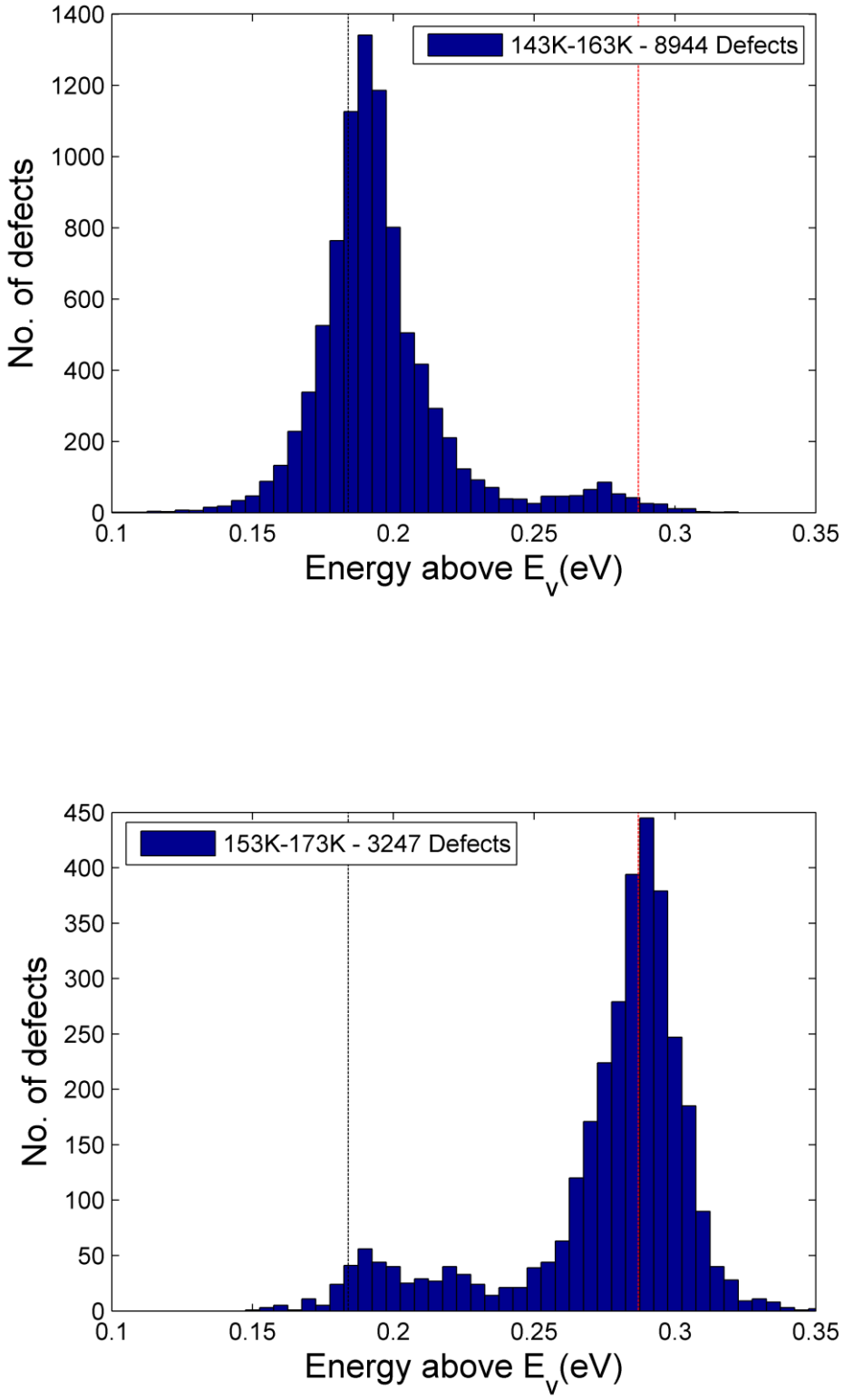

Figure 6.13 – The defect energy level distributions following the first anneal stage. Top: for all defects appearing at the three tested temperatures between 143-163K. Bottom: for all defects appearing at 153-173K. Note the difference in y-axis limits. Shown also are the energy level values for the divacancy (black line) and carbon interstitial (red line) from Mostek, (2010).

6.4.2 - 1 week RT anneal

The defect emission time constant distribution at 153K following the 1w anneal stage is shown in Figure 6.14. The total number of defects found within the tested range has increased slightly to 22848. The distribution is dominated by a single broad peak at around *10-200 µs* which appears to be split into 3 smaller independent peaks at approximately *33 µs, 57 µs, 100 µs*. This is an interesting result since the two peaks seen in the 1d anneal stage distribution are still present, although in reduced numbers. The transition of the defect distribution between the 1d and 1w stages is shown in Figure 6.15, which gives the emission time constant histograms at 153K for all defects which were detected following both stages. Both the x- and y-axes are fixed to the same scale and the histograms are binned identically. Figure 6.15 shows clearly the presence of the two peaks at *57 µs* and *100 µs* in both datasets. However by the 1w anneal stage some of the defects are no longer present, and instead there is a peak beginning to form at around *33 µs*, which is close to the emission time constant peak for the RT device. This shows that even defects which remain detectable after further anneal are not completely stable at these timescales, with defect parameters changing over time, possibly tending towards the RT device distribution.

Again 3 additional temperatures between 143-173K were tested at the 1w stage, allowing for analysis of defect energy levels. The resulting distributions are shown in Figure 6.16. A total of 5993 defects were found at all three temperatures between 143-163K with a single large peak at an energy value of:

$E = (Ev + 0.19 \pm 0.02)\ eV$

For the three temperatures between 153-173K, 1593 defects were found. In this distribution both defect species appear to be present with peaks in the distribution at values of:

E = (Ev + 0.21±0.02) eV

E = (Ev + 0.27±0.01) eV

These energy values correspond again to the donor level of the divacancy and the carbon interstitial defect. All of the results at the 1w anneal stage therefore suggest that there has not been a significant change in the number or type of defects present from the 1d stage, however there have been changes in the defect emission time constant distributions. Since divacancies are stable at RT (Watkins, 2000) there is not expected to be any movement of defects, and so the cases where a defect is present in only one of the two datasets is likely down to a change in emission time constant resulting in it being undetectable. There are also however a large number of defects which can be found at both stages with almost identical measured emission time constants, showing whilst there are still changes occurring many defects are stable at this point.

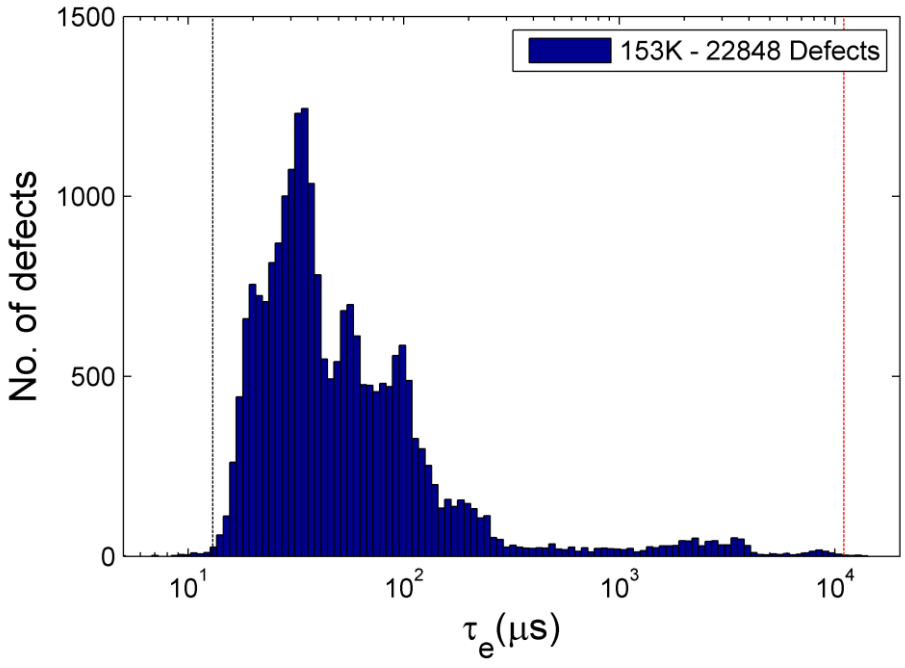

Figure 6.14 – The defect emission time constant distribution at 153K at the 1-week anneal stage.

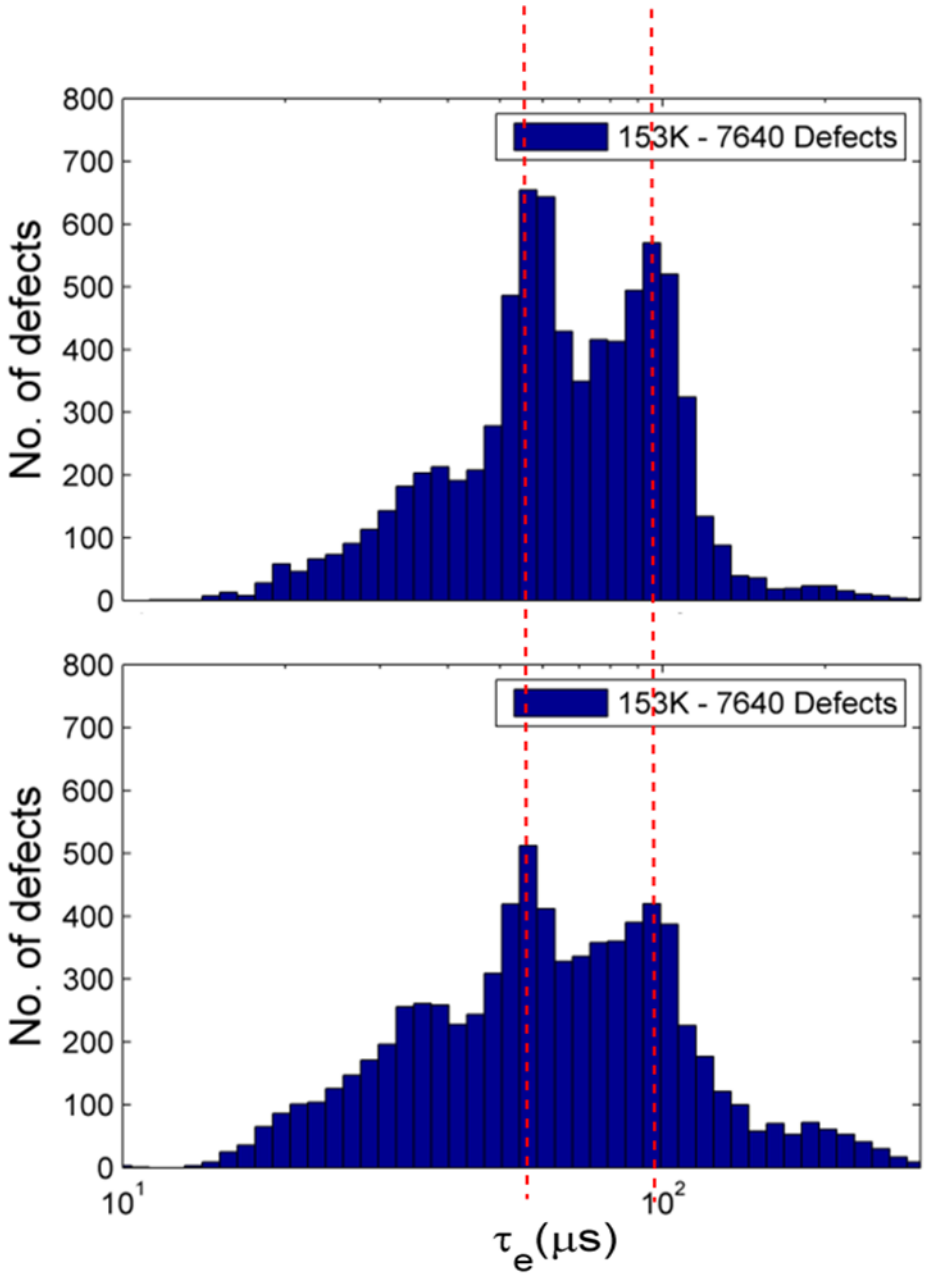

Figure 6.15 – Defect emission time constant histograms at 153K for all defects appearing at both the 1-day and 1-week stages. Top: time constants for those defects following the 1-day stage. Bottom: time constants for those same defects following the 1-week stage. The axes and binning are identical in each case. Both peaks in the distribution are discernible following both stages. The dashed lines are shown only to guide the eye.

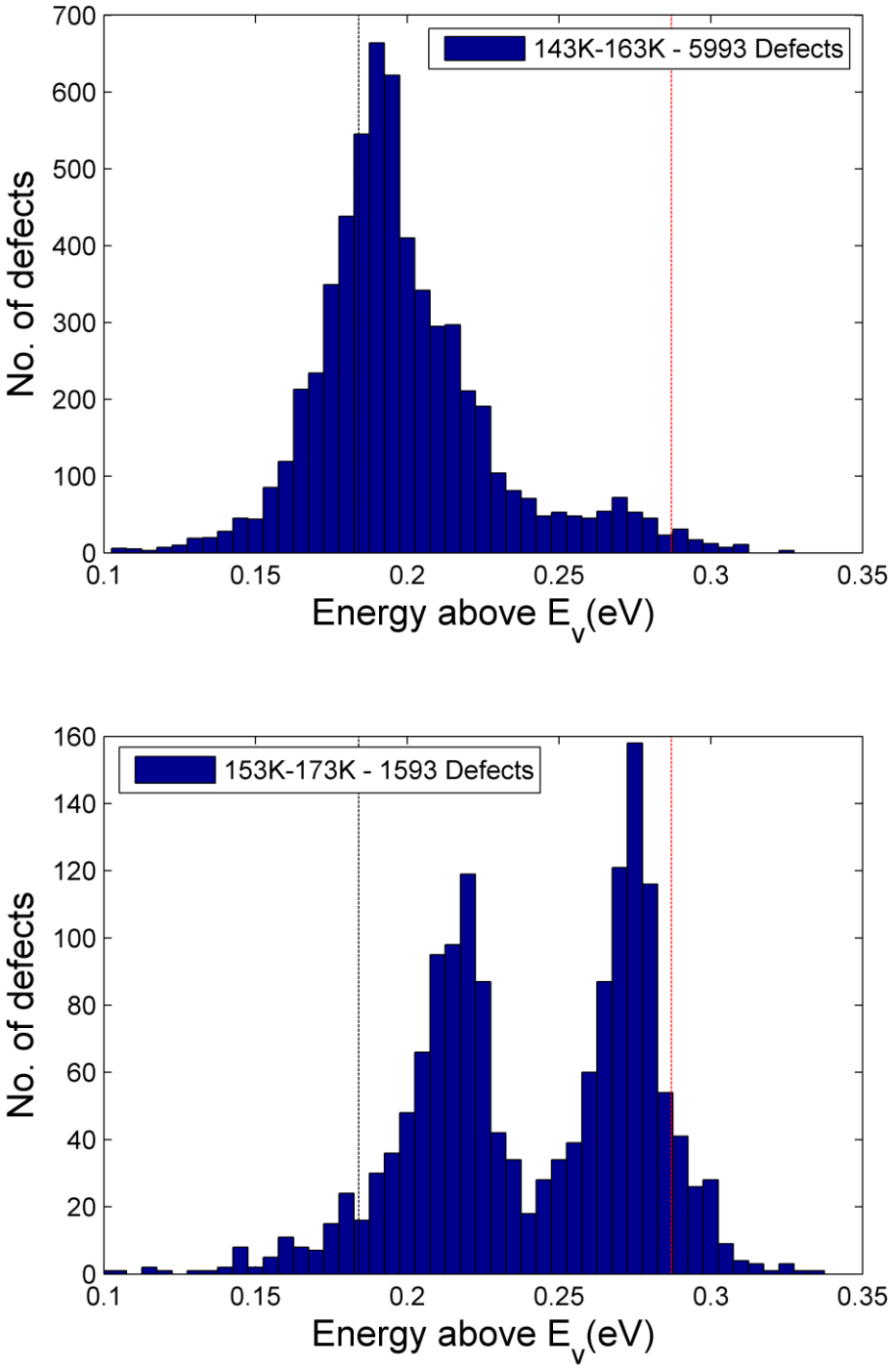

Figure 6.16 – The defect energy level distributions following the 1-week anneal stage. Top: all defects found at 143-163K. Bottom: all defects found at 153-173K. Note the difference in y-axes. Shown also are the energy level values for the divacancy (black line) and carbon interstitial (red line) from Mostek, (2010).

6.4.3 – 1 month RT anneal

The defect emission time constant distribution at 153K following the 1m anneal stage is shown in Figure 6.17. The total number of defects has fallen slightly to 21186. Overall the distribution looks has a single dominant peak at approximately *35 μs*. There are also two small peaks at around *280 μs* and *470 μs*. This continues the trend seen in the evolution of the 1d to 1w stages, where as previously discussed the initial split divacancy peak was tending towards a single peak at around *35 μs*. It again appears at this stage that the defect distribution is tending towards the RT distribution, with a single dominant divacancy related peak. Between the 1d and 1m stages we see divacancy defects with varying emission time constants, as the lattice continues to adjust following irradiation. It is clear that the situation remains dynamic over timescales of at least several weeks.

Two additional temperatures between 143-163K were analysed at the 1m stage. In total 2927 defects were found at all three temperatures. The energy level distribution (Figure 6.18) shows again two peaks, with energy levels of:

$E = (Ev + 0.20 \pm 0.02)\ eV$

$E = (Ev + 0.26 \pm 0.01)\ eV$

Which as with the results at previous stages correspond to the donor level of the divacancy and the carbon interstitial defect. An interesting result is the appearance of the carbon interstitial defect across the three temperatures 143-163K. This was not the case at the 1-week stage, where they did not appear at the coldest temperature 143K. This suggests the possibility that much like the divacancy defects there is a general trend for emission time constants to be getting faster over time, although further study would be required to draw any definite conclusions from this.

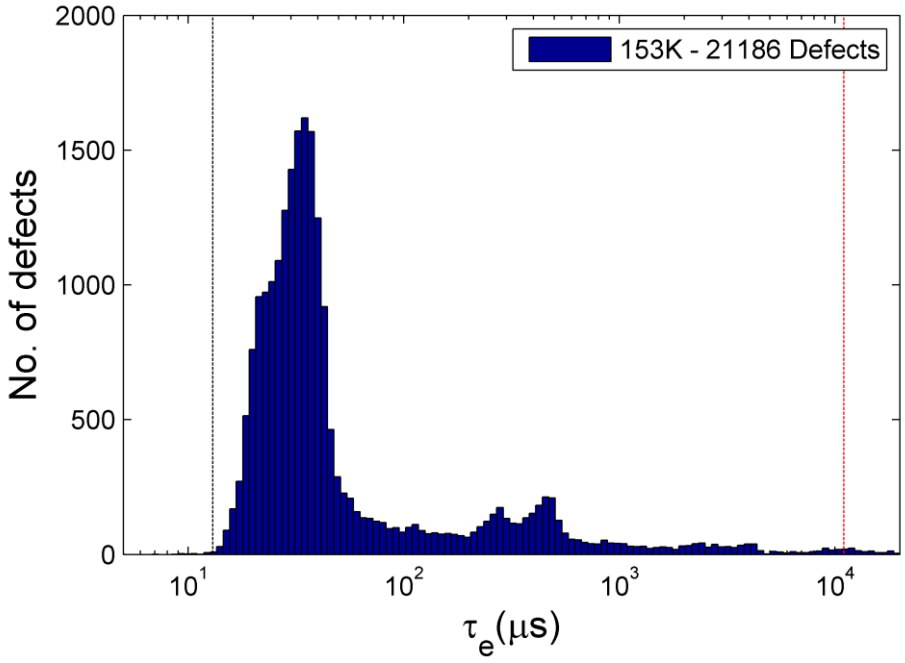

Figure 6.17 – The defect emission time constant distribution following the 1-month anneal stage.

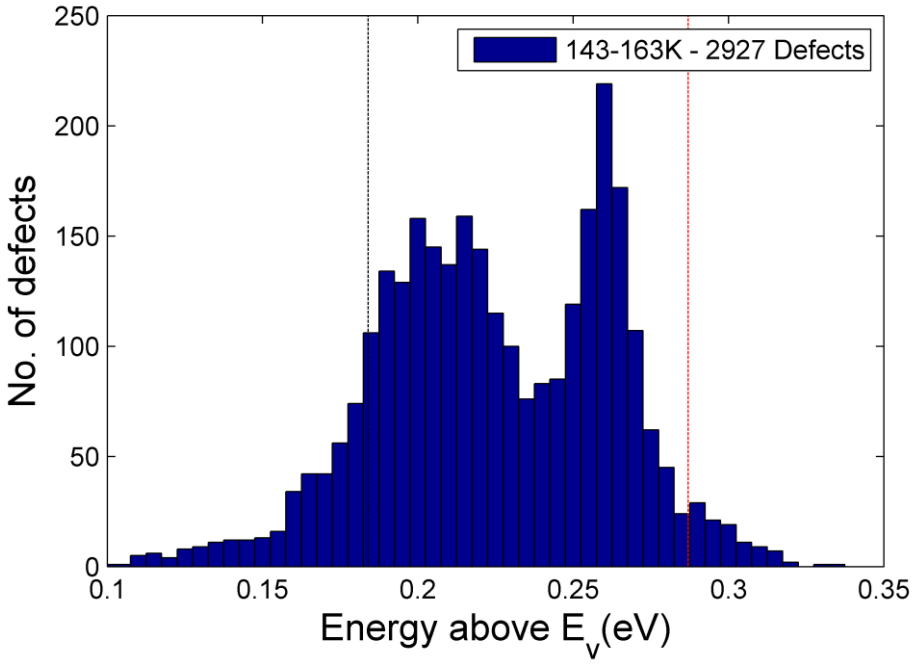

Figure 6.18 – The defect energy level distributions following the 1-month anneal stage. For all defects which appear at all three tested temperatures between 143-163K. Shown also are the energy level values for the divacancy (black line) and carbon interstitial (red line) from Mostek, (2010).

6.4.4 – 3-month RT anneal

The emission time constant distribution at 153K for the 3-month anneal stage is shown in Figure 6.19. It is very similar to the distribution seen following the 1-month stage, suggesting that the lattice is now more in a more stable state as would be expected. Again the defect distribution is dominated by a single peak at approximately *34 μs*, with secondary peaks at around *280 μs* and *450 μs* which have now increased slightly in number. The total number of defects within the tested range is 23415.

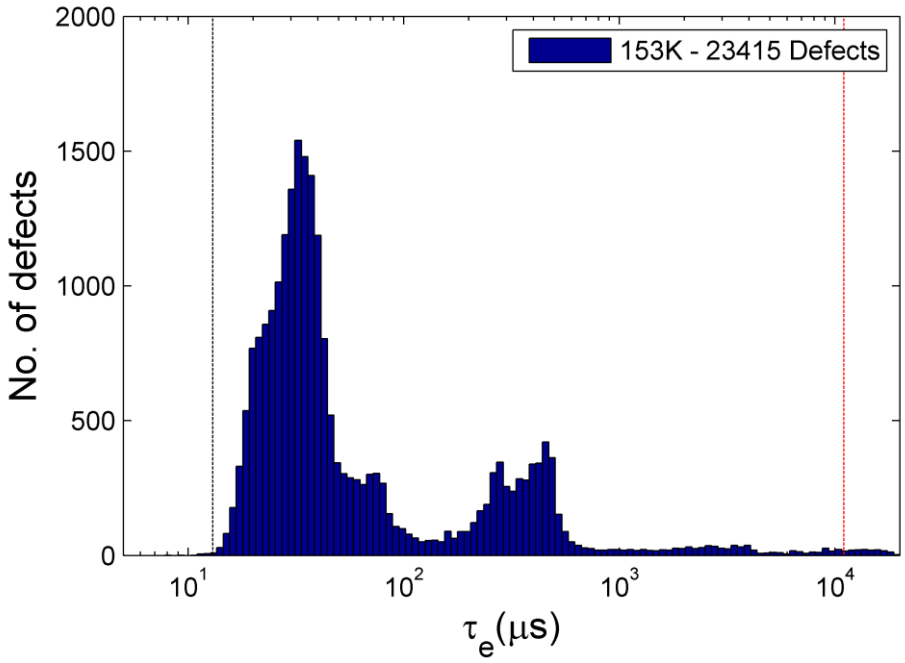

Figure 6.19 – The defect emission time constant distribution at 153K following the 3-month anneal stage.

6.4.5 – 10-month RT anneal

At the final stage the defect emission time constant distribution at 153K (Figure 6.20) still shows small changes but is overall much the same as the distributions seen for the 1m and 3m stages, with a dominant peak at around *35 μs* and secondary peaks at around *280 μs* and *450 μs*. There is however the emergence of a shoulder peak at approximately *20 μs.* It appears as though this is close to the likely final stable defect distribution if the device was allowed to anneal indefinitely, since no major new changes are occurring over timescales of several months.

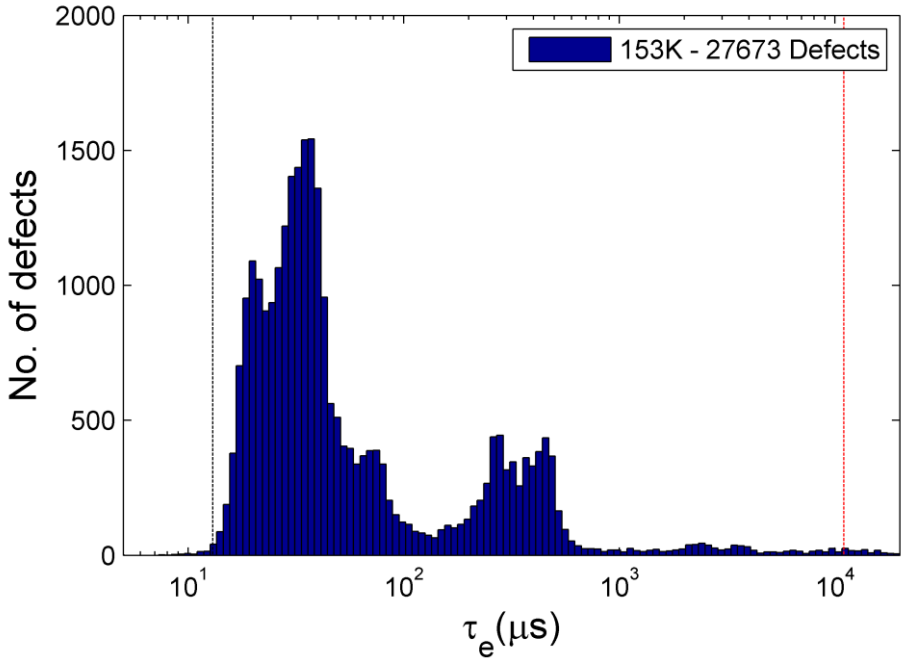

Figure 6.20 – The defect emission time constant distribution at 153K following the 10-month anneal stage

6.4.6 – Discussion

It has been shown in this study that temperature as expected has a significant impact on the defect distribution in an irradiated CCD. At each tested stage there are differences observed in the emission

time constant distributions. This leads to the question of what happens to the emission time constants of defects which appear at all stages, if indeed there are any. Since trap-pumping can study defects individually, the pixel location of each within the device is known. Therefore it is possible to track the defects which appear at multiple stages. As stated previously, since we are searching only for defects within the given phase-time range, there are expected to be many more defects present than are detected. This is shown by the large number of compound dipole intensity curves which are seen post-irradiation. Therefore the fact that two defects appear in the same pixel at two or more stages does not guarantee that they are the same defect. However if they produce intensity curves which give similar values for both emission time constant and P_c then it can be assumed that they are likely the same defect.

The total number of defects post-irradiation in the cryogenic device was 5341. Table 6.2 gives for each anneal stage the number of defects which were found in the same location. As expected the number of common defects is reduced at each anneal stage with the changing defect distributions. However a total of 381 defects were found to appear at every stage, and so these were analysed further to investigate any changes in their emission time constants over time. It is possible that a number of these defects were present pre-irradiation, however many more are observed than would be expected if this were the case for all of them, since only 1 fitted defect in the divacancy range was found per 3000 pixels in the device control region. Defects with both fast and slow emission time constants were found across all stages. Figure 6.21 shows for a random selection of the faster defects the emission time constants following each anneal stage. Each line corresponds to a single defect detected and fit successfully in the same pixel within the device. There are a few cases where the defect emission time constant changes significantly; which suggests two different defects have been located within the same pixel following different stages. However in general there is a good degree of stability in the emission time constants, with many changing by less than 10% over the entire study. Since the time constants are highly sensitive to temperature, and also to local field effects etc. it would be expected to see changes of this order over multiple tests even if no

changes to the device made between them. A number of slower ($\tau > 1000\ \mu s$) defects were also analysed in this way that are not shown in Figure 6.21, and a similar situation was observed. This is a very interesting result, since a number defects can be seen which appear highly stable in terms of their emission time constants over a period of 10 months, even through the first anneal stage in which the overall defect distribution changed dramatically.

As previously outlined, both defect species are not expected to diffuse (at least thermally activated) within the device at the tested temperatures. Therefore an alternative cause of the large changes in defect density observed throughout the study is that emission time constants are changing such that some defects move in or out of range. In particular, results from the 1-week to 10-months stage suggest that perhaps the general effect is a decrease in emission time constant (i.e. defects get faster) over time. However no such trend is apparent in Figure 6.21. It appears therefore that although there are clearly large-scale changes taking place within the CCD lattice throughout this study, not all defects are affected in the same way.

Stage	Total time at RT (hrs)	No. of defects
1. Cryo PI	0	5341
2. 1 Day	26	2039
3. 1 Week	194	1127
4. 1 Month	698	560
5. 3 Month	2042	429
6. 10 Month	6074	381

Table 6.2 – The number of defects found following each anneal stage which also appeared in the initial distribution post-irradiation, in the same pixel within the device.

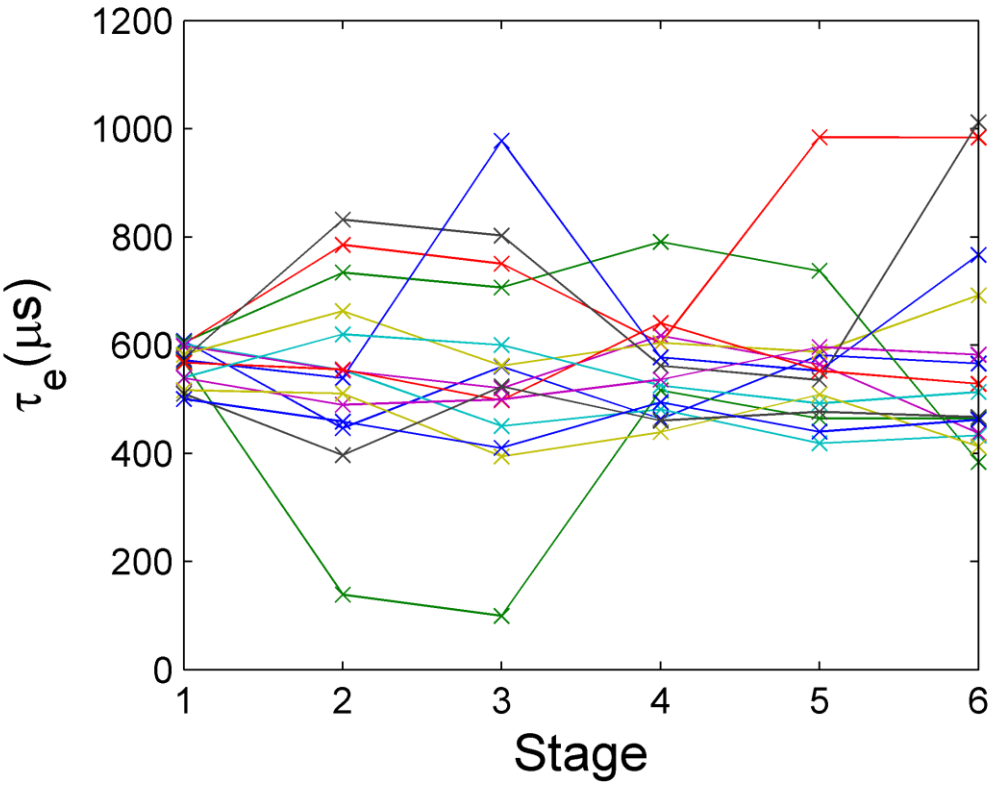

Figure 6.21– For each stage (1 refers to post-irradiation, 2 to post 1-day anneal etc.) the defect emission time constant for a selection of the faster defects found to appear at all stages. Each line represents a single defect.

6.5 – Divacancy behaviour following cryogenic irradiation

This study has given insight into the evolution of radiation induced defects within a CCD over a period of several months following cryogenic irradiation and subsequent room-temperature anneal. Whilst the long-term defect distribution has crucial implications for device performance in a harsh radiation environment, from a physical point of view the initial few minutes and hours immediately post-irradiation are of great interest. As part of this study it was possible to take data with the cryogenic device at 153K from immediately following the irradiation up until the first anneal. A full trap-pumping analysis was performed as part of the main study (see Figure 6.9 and related discussion) however the full data-set of 160 images covering the entire phase-time range takes several hours to perform. Therefore a method with reduced temporal resolution was employed,

giving the possibility to estimate the defect density every few hours post-irradiation. It was found through testing that dipole intensity curves could still be fit reliably providing there were sufficient data points either side of the peak. Although some accuracy is lost on emission time constant analysis, the data can be taken in around an hour. The tested phase-time values were chosen in order to provide enough points either side of the suspected intensity peak for the donor level of the divacancy at 153K, as taken from the values in Mostek and from the previous work in this thesis. Since only a few phase-time values can be tested a compromise must be made on which defect species to focus on; the divacancy was chosen since it was the dominant species in the room-temperature device, and also since it is a faster defect level than the carbon interstitial level, meaning the trap-pumping frames are quicker to obtain.

This data was taken as part of a wider study which demanded that the device remain at 153K during the period immediately post-irradiation. Therefore the defect species must be estimated from the emission time constant data. A cut-off point was made where every defect which was fit successfully with an emission time constant less than *120 μs* was deemed a divacancy. This value was chosen as it is around the upper limit for the divacancy time constant at 153K. Whilst an approximation, using this method of a simple cut-off point is adequate for an initial estimate of defect numbers after a cryogenic CCD irradiation, which is a topic that has not been investigated using a method such as trap-pumping with the ability to locate individual defects. The results, showing defects per pixel for the two analysed areas (control and irradiated) of 600x400 pixels, are given in Figure 6.22. For the first few days following irradiation and before the first anneal stage there are small changes in the number of divacancy defects. This is better illustrated in Figure 6.23, which shows an image of the data-points from the irradiated section of the device for the first 100hrs after irradiation. In the control region the density of traps is very low as expected, with less than one detected and fitted divacancy defect per 3000 pixels. In the irradiated region the number of divacancy defects is increased by approximately a factor 20, however this value is still unexpectedly low when compared

to the typical density of divacancy defects seen after a RT irradiation (Mostek, 2010). For the first 100 hours following irradiation, a small decrease of approximately 5% is seen in the number of fitted defects. Although this is an interesting result it must be treated cautiously since if a defect emission time constant moves out of the tested phase-time range it is not detected. It is evident that changes are taking place over the initial days after irradiation, however since divacancies are highly stable defects at 153K (Watkins, 2000) a potential explanation for the result is a change in defect emission time constants, which was also a result seen in the full distributions post-anneal. This could be expected in a device immediately post irradiation where the lattice state remains dynamic and mobile defects can still be present. Other explanations could include potential isothermal annealing of defects, as the CCD lattice is restored to a stable state following irradiation. It is also possible at low temperature that other defect species may take more time to form in large numbers. Although other defect species will not be counted in this analysis, if they are present in the same pixel as a divacancy defect there is the potential for interference between the two as discussed in Chapter 4. This can lead to dipole intensity curves that cannot be fit with Equation 4.3. The downward trend in divacancy density appears to be levelling off at the point of the first anneal, and so a strong case for further work would be similar analysis over a longer timescale, to see if the density converges to a final value.

Also of note is the first point on the curve, which has an anomalous low density value. A similar case is seen for the control region of the device, which could suggest that this is potentially not a true physical effect but rather a difficulty in identifying defects across the whole device for this set of images. However since it is the first dataset taken post-irradiation and all sets were taken under the same conditions, it is possible that the low value is due to irradiation-induced defects still being formed in the CCD. Therefore the first few hours post-irradiation is a good candidate for future work.

Immediately obvious from Figure 6.22 is the significant increase in the number of divacancy defects

found following the first room-temperature anneal stage. This increase of approximately 10x matches what was observed in the full-trap pumping runs pre- and post-anneal, and also potentially explains the approximate 10x increase in serial CTI (at *1 μs* serial transfer time) observed by Mostek (Mostek, 2010). No discernible increase was found in the control region of the device and so this observation must be due to radiation damage effects. This is a result not previously published and has very important implications for CCD detectors, since it is clear that the potentially beneficial effects of a cryogenic irradiation with respect to the preferable defect distribution are lost if the device cannot be maintained at a cryogenic temperature. This also presents an opportunity for further study to better quantify the effect at various temperatures and under various operating conditions.

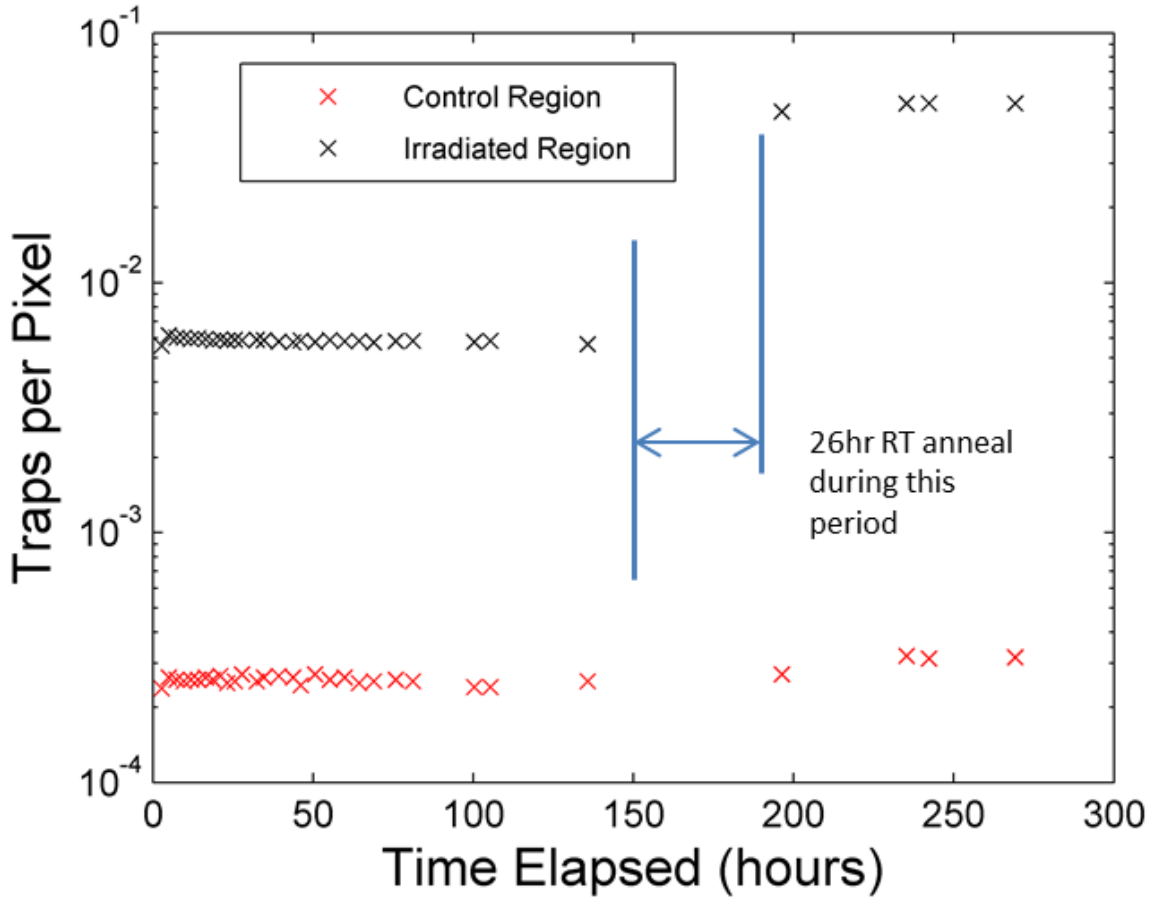

Figure 6.22 – The number of fitted divacancy defects following the cryogenic irradiation and first anneal stage.

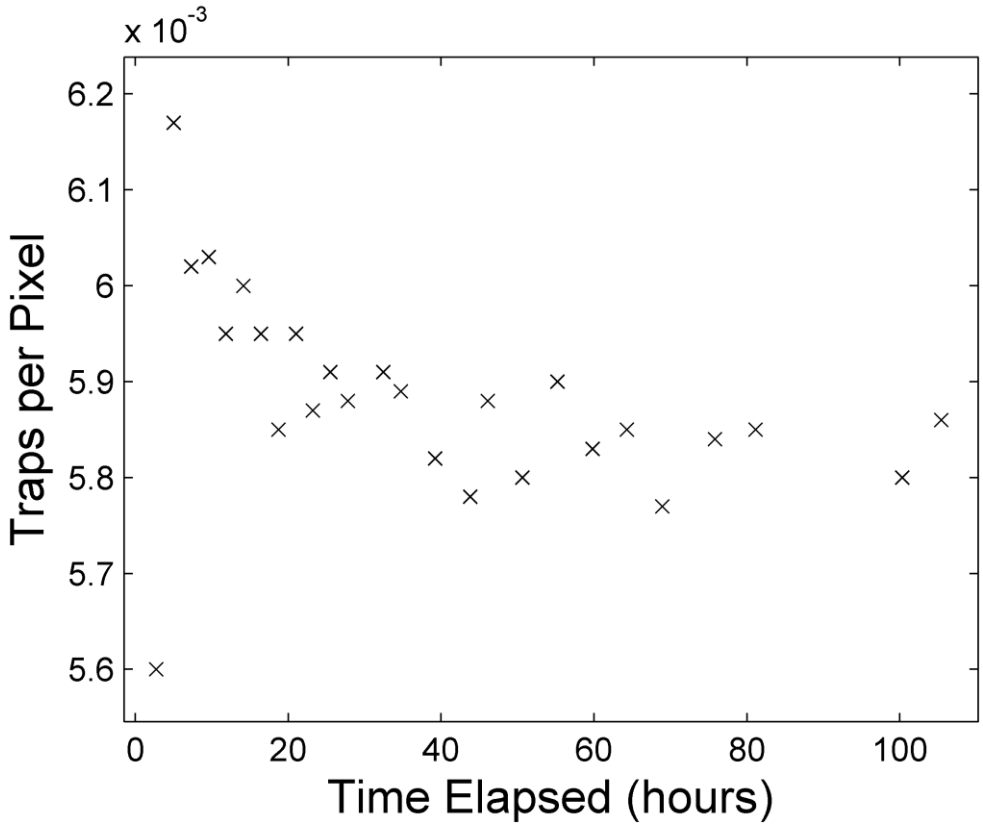

Figure 6.23 – An image of only the first 100 hours following irradiation, for the irradiated region of the device. Note the anomalous first data-point in which a lower defect density was observed.

6.6 – Summary

The purpose of the work in this Chapter was to investigate the effect of irradiation temperature on the defect distribution in a proton irradiated p-channel CCD. The main aims were to identify any major differences between a device irradiated at RT and one irradiated at 153K. Defects were analysed using the method of single trap-pumping. One CCD was irradiated at RT, whilst a second identical CCD was irradiated and tested at 153K, followed by a number of RT anneal stages, each followed by further testing. In total 5 anneal stages were analysed, culminating in a total RT anneal time of approximately 10-months. The main results from the trap-pumping analysis are summarised in Table 6.3.

An approximate 4x decrease in the number of defects within the tested range was found for the cryogenic device when compared with the RT device, which was dominated by the donor-level of the

divacancy. However following the first anneal stage the number of defects in the cryogenic device increased by approximately the same factor, with around a 10x increase in the number of divacancy defects in particular. This result supports the work seen by Mostek in which the CTI at a temperature of 140K and a transfer time of *1 μs* was found to increase by a factor 10x following the RT anneal of a CCD irradiated cryogenically (Mostek, 2010). Progressing through the anneal stages, the defect emission time constant distribution began to more closely resemble that seen in the RT device, with a dominant peak around *20-50 μs*. A number of slower defect peaks were also observed in fewer numbers. From the 1-month stage onwards the distribution is more stable however there are still small changes, particularly in the total number of fitted defects which continued to increase up until the final tested stage.

The results from this study show that temperature, as expected, plays a major role in the development of the defect-distribution post-irradiation. Both the divacancy and the carbon interstitial defect are not mobile at RT, and so any defect movement would have to be induced by other means. It was therefore suggested that the large changes in defect density are due to the defect emission constants moving in/out of our tested phase-time range. However, a number of defects were found in the same location within the device at all stages, and their emission time constants are reasonably stable, with many changing by less than 10% throughout the entire study. Whilst it is possible that some of these defects were present pre-irradiation, it is unlikely from the densities seen in the control region that this is the case. This leads therefore to the question of the cause of the large changes seen in the defect distributions observed throughout this study. It is possible that not all defects are affected in the same manner by the anneal process, especially at a short time after irradiation where the situation is still expected to be relatively dynamic.

The crucial result from this study, particularly with respect to space-based detector missions, is the differences observed in the initial defect distribution post-irradiation between the two devices, and the large changes observed in the cryogenic device after the first room-temperature anneal. This has

not been reported previously for the case of image sensors, and the implications for radiation testing are significant. As part of the larger study into cryogenic irradiations these results were presented at the European Space Agency ESTEC facility in the Netherlands, and they have since dedicated considerable resources to further investigations of cryogenic irradiations and their potential benefits for detector performance. As previously stated all current radiation damage testing for ESA missions is done using room-temperature irradiations, whilst in space devices receive damage operating at cryogenic temperatures. The very large differences between the defect distribution in both cases may mean that device optimisation completed pre-launch actually recommends operating conditions which are not at all optimal, which is the main aim of such characterisation work.

A complete explanation of the effects of temperature on the radiation damage effects is therefore an important area for further studies, particularly one in which a device is irradiated cold and maintained at such a temperature without ever being annealed. In the author's view, the most likely explanation for the large increase observed in the divacancy density post-anneal is that since both mobility and lattice energy are reduced with decreasing temperature, it is not possible at 153K for the large scale production of divacancy defects. It may be that most single vacancies do not have enough energy to form a divacancy defect at 153K and therefore are either still mobile within the lattice or produce another, more energetically favourable defect that is not within the tested phase-time range. Fewer vacancy collisions in general would also be expected at lower temperature, even though single vacancy defects are still highly mobile down to temperatures of only a few Kelvin (Watkins, 2000). Following the RT anneal and increase in lattice energy, the mobility and energy of any remaining vacancy defects will increase, and this could be the cause of the increase observed in divacancy density. Again this study has shown that further work is clearly important in this area in order to better understand the role of temperature on radiation damage processes in a CCD and to contribute to our basic understanding of defect behaviour. In the context of a space-mission it could potentially be vital, since the current standard for pre-flight device characterisation is using a RT anneal, whilst the actual device in space receives radiation whilst operating at cryogenic

temperatures. Therefore, transfer times may be incorrectly chosen to avoid defect species which are expected to dominate CTI.

Stage		No. of defects		Main τ peak (μs) – FWHM		Secondary peak (μs)		Energy (eV) - FWHM
RT device		18160 (scaled)		20-50				0.16-0.24
Cryo PI		5341						
1-day		20394		50-70		80-110		0.18-0.20
1-week		22848		20-40		55, 100		0.18-0.21
1-month		21186		20-45		280, 470		0.25-0.27
3-month		23415		20-45		280, 460		
10-month		27673		20-45		20, 280, 460		

Table 6.3 – A summary of the results from the trap-pumping analysis of the RT device (red) and the cryogenic device (blue).

Chapter 7 – Proton-irradiated N-channel CCD study

Two studies have been carried out on radiation-induced defects in p-channel CCDs. Whilst p-channel CCDs have become more viable options for use in space-based detectors recently, currently n-channel CCDs are the standard, and as such the charge-trapping defects have been more extensively covered in literature. The advantages of the trap-pumping technique as previously outlined give the opportunity to supplement this information with a study of radiation-induced deep-level defects directly in the time domain, which is of importance when considering CCDs for use in harsh radiation environments such as space. The aim of the work within this Chapter is to study a proton irradiated n-channel device using trap-pumping. The emission time constants of the primary charge trapping defects are measured at a number of different temperatures, along with analysis of energy-levels and cross-sections. An initial observation is also made into the possible effects of signal level or electric field on the defect emission time constant.

For an n-channel CCD, the defects which are of potential importance when considering CTI are the single and double acceptor levels of the silicon divacancy, the vacancy-oxygen (VO) defect and the vacancy-phosphorous defect (VP). Since phosphorous is often used as a donor dopant in n-type silicon the VP defect is often cited as the most predominant radiation-induced defect in an n-channel CCD (Holland, 1991). However, at typical operating temperatures for a space-based mission the VP defect is slow, and therefore would not be expected to dominate for effects such as shape measurement error. As previously stated it is also difficult to study slow defects with trap-pumping. Therefore we concentrate on the other defects and particularly the double acceptor level of the divacancy, which at typical operating temperatures has an emission time constant comparable to the parallel clock width. Figure 7.1 shows the expected defect emission time constants for the temperature range 150-250K. These were calculated using SRH theory (see Chapter 3) from the generally accepted defect energy levels as reported in the literature. As in the case for p-channel defects, numerous results are given in the literature for both defect energy level and cross-section

which do not always agree. The values used for the curves in Figure 7.1 came from a DLTS study by Eremin, with the upper and lower limits calculated using upper and lower energy level limits from other DLTS studies (Hallen, 1996; Eremin, 1999; Zangenberg, 2002; Auret, 2004; Nyamhere, 2006). These curves provide a baseline for comparing the measured defect emission time constants from trap-pumping work. Also shown in Figure 7.1 is an "unknown" defect species with an energy level around *0.30 eV* which was observed in an X-ray CTI study by Holland but whose origin was not identified (Holland, 1993). This possible defect level will be discussed further later in this Chapter.

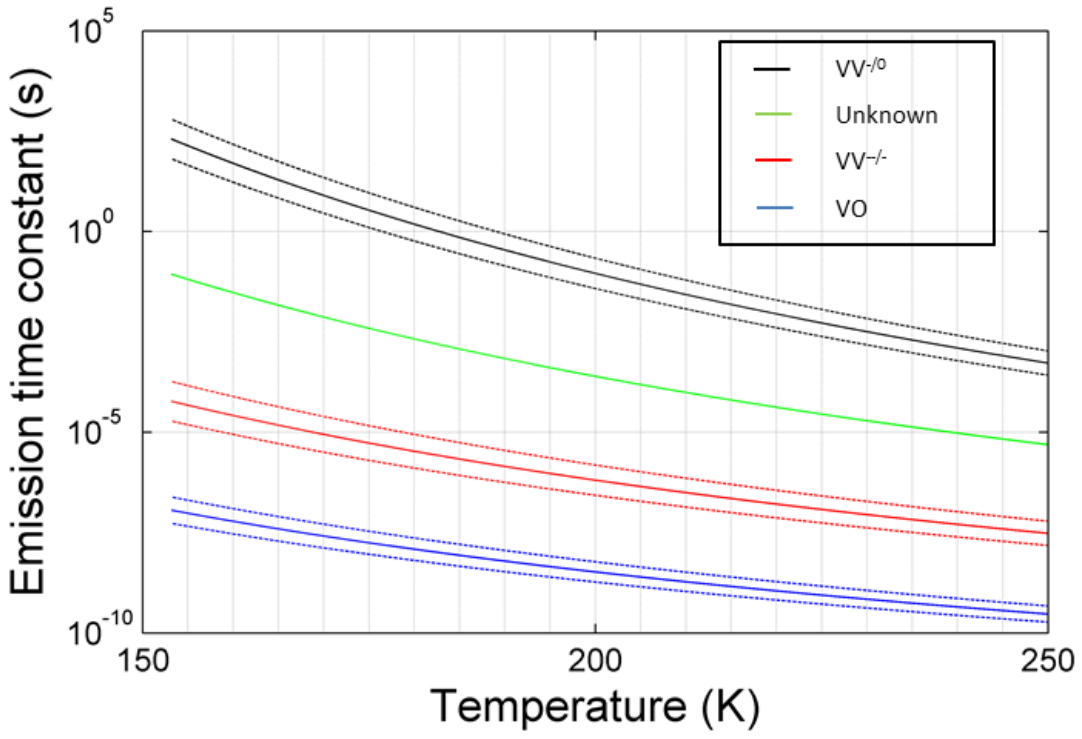

Figure 7.1 – The calculated emission time constant vs. temperature for the predominant charge trapping defects of concern for this study. The green line represents a defect with energy-level of around E_c-0.30eV which was reported in an X-ray CTI study by Holland (Holland, 1993).

7.1 – Room-temperature irradiated n-channel CCD test campaign

For the work on p-channel CCDs described in Chapters 5 and 6 data was taken as part of a larger CCD characterisation study and under strict time limits, meaning it was not always possible to gather as much trap-pumping data as desired. In this Chapter a trap-pumping study of a proton-irradiated n-channel CCD is described, where the experimental set-up was designed entirely for the purpose of taking trap-pumping data. This allowed for more freedom in the direction of the study, and enabled parameters such as temperature to be more strictly monitored. The device used for this work was the e2v CCD47-10 (e2V datasheet A1A-100021, version 9) which is a 1k x 1k pixels full-frame, back-illuminated n-channel CCD with 13µm square pixels. The CCD47-10 has a single serial register with nodes at either end such that charge can be read out through one of them or split between the two. The CCD47-10 is available in both inverted and non-inverted mode operation with the device used for this work a non-inverted mode operation variant. A schematic of the CCD47-10 is shown in Figure 7.2. A single device was irradiated with protons at the Paul Scherrer Institut in Switzerland to a 10 MeV equivalent fluence of 2.5×10^{9} p cm^{-2}. The complete device was irradiated to the same fluence, at room-temperature.

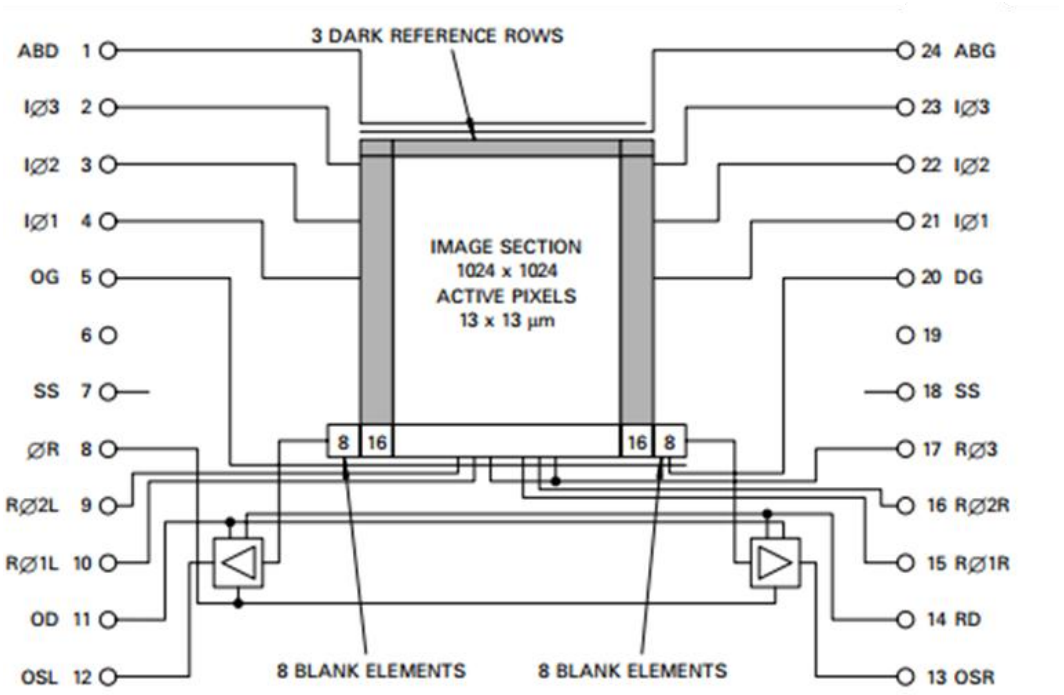

Figure 7.2 – A schematic of the CCD47-10 showing the various connections and the single output register with two separate output nodes. Taken from the CCD datasheet (e2v A1A-100021, version 9).

The experimental set-up follows much of the same principles which were described in Chapter 4. A schematic of the basic set-up is shown in Figure 7.3, and a photograph of the chamber is shown in Figure 7.4. The CCD is contained within a vacuum chamber and cooled using a PolyCold PCC cooler and Cryotiger cold-end. A copper contact, cold bench and cold finger were designed in AutoCAD and maintain a thermal connection between the cold-end and the CCD, as shown in Figure 7.5. The minimum device temperature achieved with good stability over a long period of time was measured to be around 160K. The CCD temperature was monitored using a pt-1000 as an input to a Lakeshore temperature controller. The sensor was attached directly to the CCD packaging, giving the highest possible accuracy for such an important parameter with respect to defect analysis. The temperature was recorded for every image taken, ensuring that there was no large deviation during any particular run, as they can take several hours. Any significant temperature changes were always followed by a waiting period to ensure temperature had stabilised sufficiently across the device. The Lakeshore has a temperature stability of 0.2K, and the maximum total deviation in temperature between

measurements across a single trap-pumping run was found to be 0.5K. The CCD input and output connections, as well as an LED light source, were controlled using an XCAM camera system. The phase-time parameter was controlled as the parallel clock width in the CCD sequencer. A time parameter was set in the CCD sequencer which had a linear relationship with the clock width. The relationship between this time parameter and the actual clock width was measured and recorded such that the phase-time conditions could always be set through a single parameter in the sequencer.

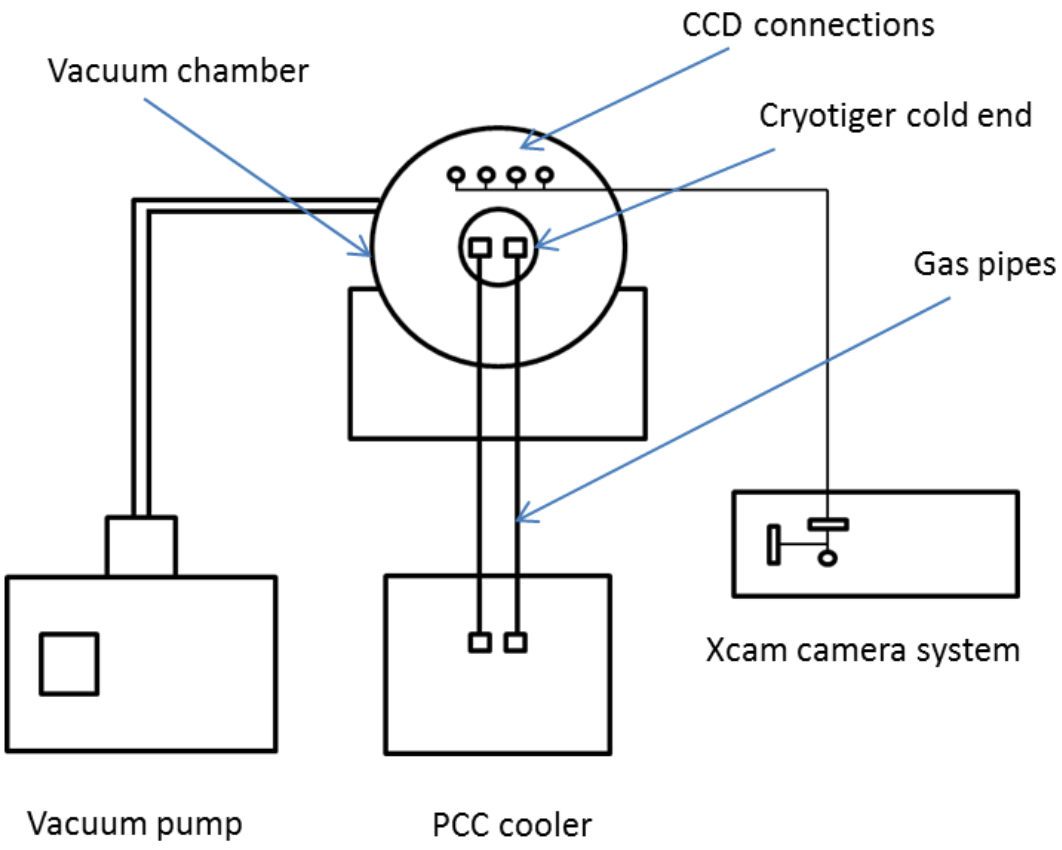

Figure 7.3 – A schematic of the basic experimental set-up for the work presented in the Chapter.

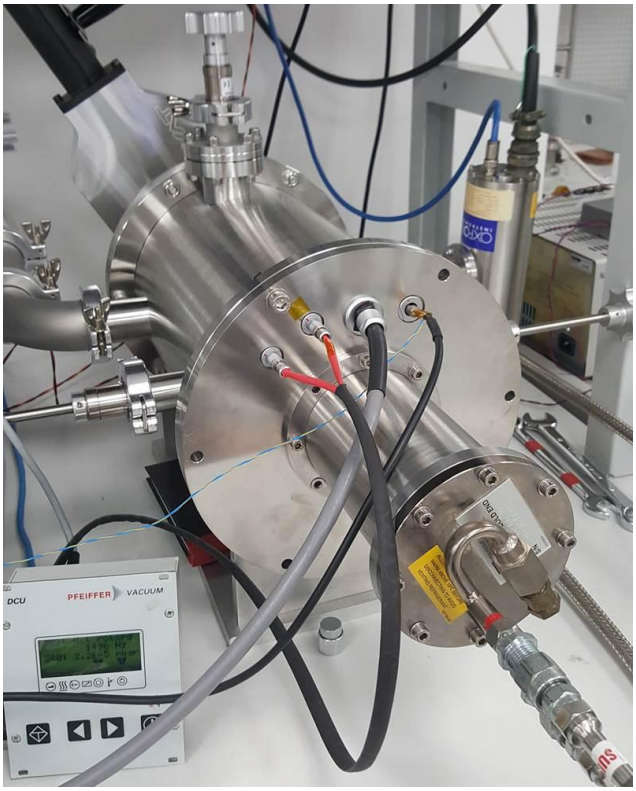

Figure 7.4 – A photograph of the vacuum chamber showing the Cryotiger cold-end casing and the CCD input/output connections.

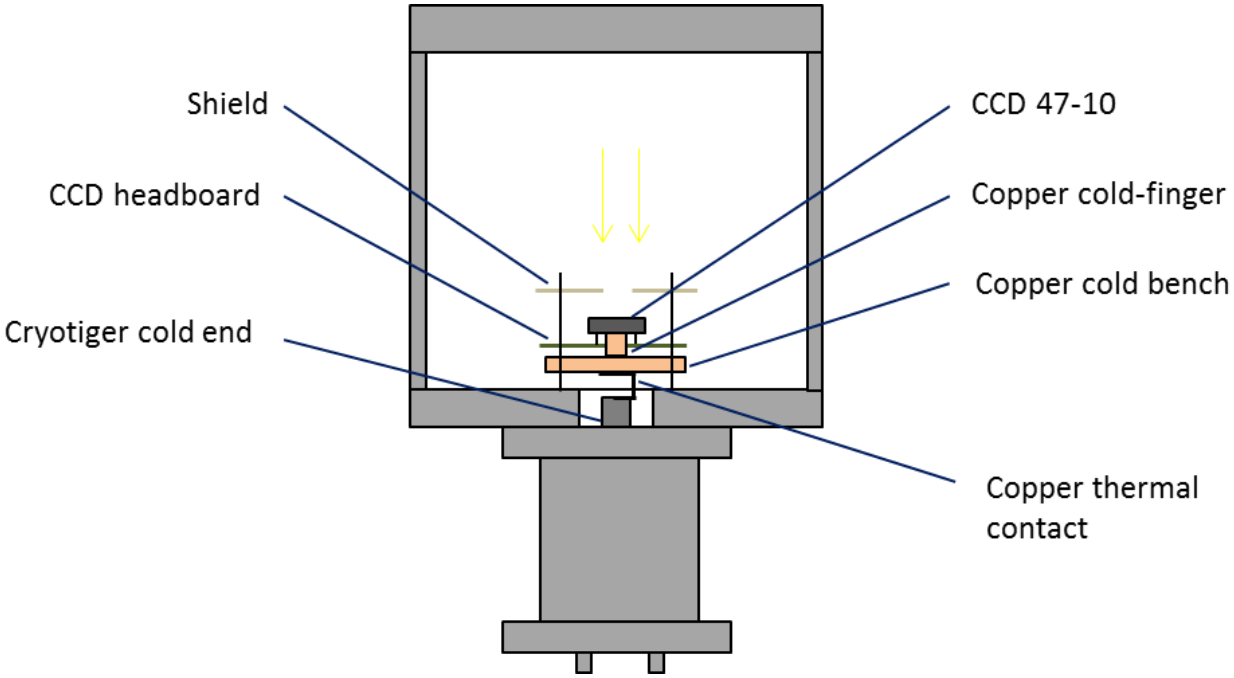

Figure 7.5 – A schematic of the inside of the vacuum chamber, showing the thermal connection made between the Cryotiger cold-end and the CCD47-10.

The trap-pumping analysis was carried out in much the same way as for the p-channel work described in Chapters 5 and 6. An 800x600 pixel ROI was used for all analysis, as indicated in the sample image shown in Figure 7.6. Signal dipole intensity curves were fit with Equation 4.3 and only those curves with an r-value greater than 0.85 were included in the final analysis. A selection of the observed curves is shown in Figure 7.7. The number of pumps used for each image taken was *N=1500*. For dipole detection, a threshold of 3σ was used for the signal level background. A phase time range of *1-500 μs* was used for all work. Again not all images were searched for signal dipoles but instead a selection of images which cover the entire phase time range at a given temperature.

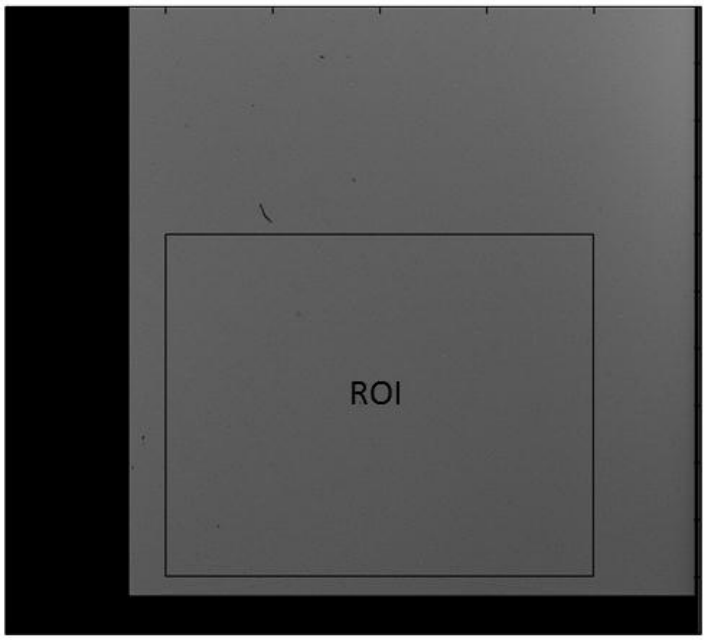

Figure 7.6 – An example CCD47-10 image showing both the parallel and serial overscan regions and the 800x600 pixel ROI.

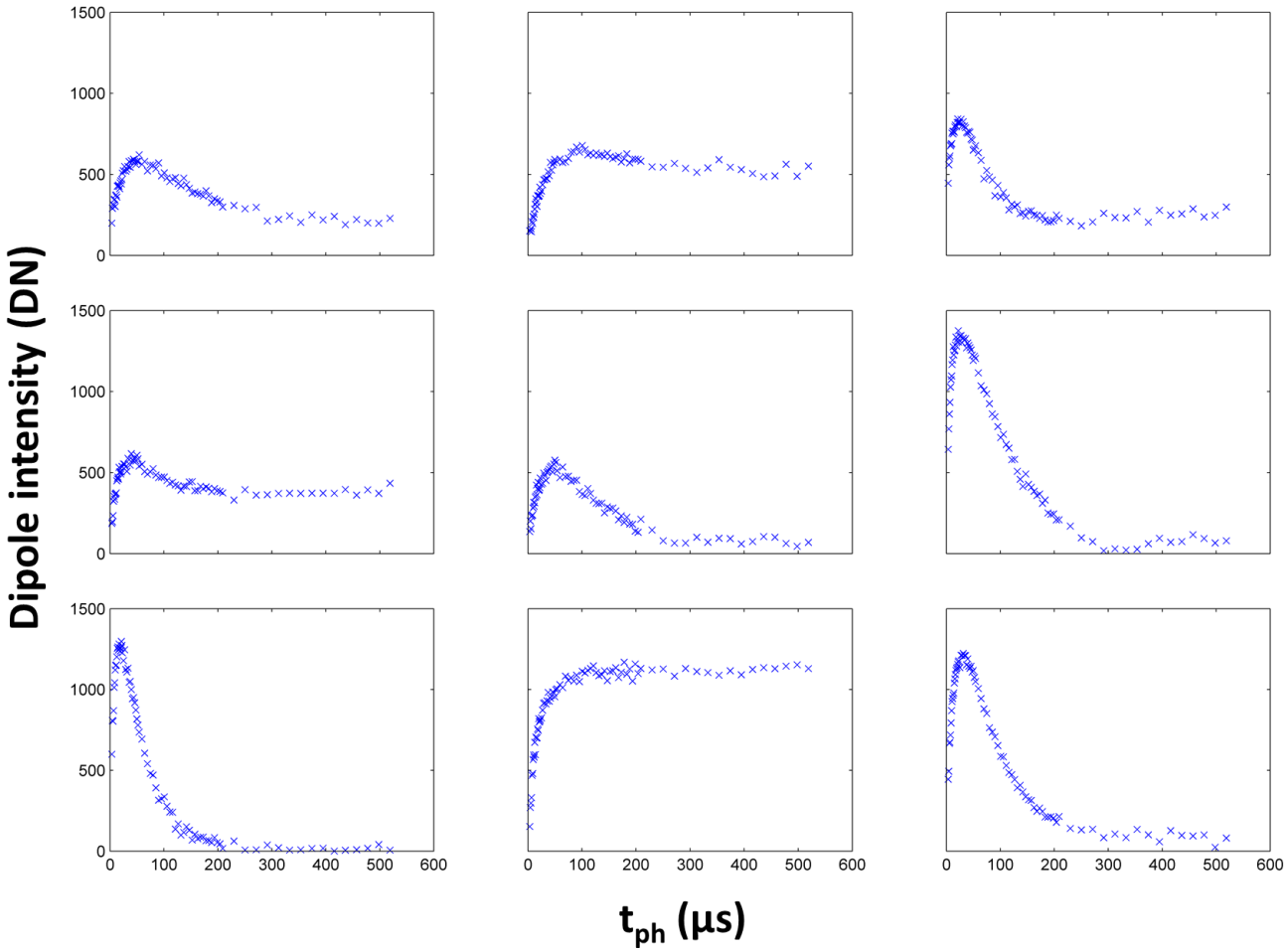

Figure 7.7 – A selection of the observed signal dipole intensity curves across a range of temperatures in trap-pumped images of the n-channel CCD47-10.

7.2 – Trap-pumping study

As previously discussed the main aim of the work in this Chapter was to analyse both the single and double acceptor levels of the silicon divacancy, and to probe the range between them where the is a potential defect level of unknown species as reported by Holland, (1993). Three temperature ranges were therefore chosen for investigation which along with the achievable phase time range will cover all three defect levels. The results from the work at each temperature range are presented and discussed here.

7.2.1 – Trap-pumping results: Temperature range 170-184K

The first temperature range analysed was 170-184K, with the intention of probing the double acceptor level of the silicon divacancy. A total of eight temperatures were tested under the conditions described earlier in this Chapter. Between 6000 and 10000 defects were found at each temperature, with a total of 3849 found to appear across all eight. A selection of the defect emission time constant histograms are shown in Figure 7.8 along with the theoretical emission time constant for the tested temperature. The results at all eight temperatures show one dominant approximately Gaussian shaped peak; however as was observed in the p-channel work there appears to be a splitting effect around the peak maximum, potentially showing two separate Gaussian shape distributions which overlap.

The measured defect emission time constant range at 170K is around *20-70 μs* and as expected defects become faster with increasing temperature, with a range of approximately *6-20 μs* at 184K. As can be seen in Figure 7.8 the defect emission time constants are in general slightly slower than the theoretical value for the double acceptor level of the divacancy but are around the correct range. This is shown more clearly in Figure 7.9 which shows for the 3849 defects which were found at all temperatures the measured emission time constant, overlayed on the theoretical curve shown in Figure 7.1. Both the histograms and Figure 7.9 also display the observed spread in emission time constants which is considerable; however as in the p-channel case the lines for each individual defect run relatively parallel to one another, indicating that this spread is not the result of uncertainties in the measurement.

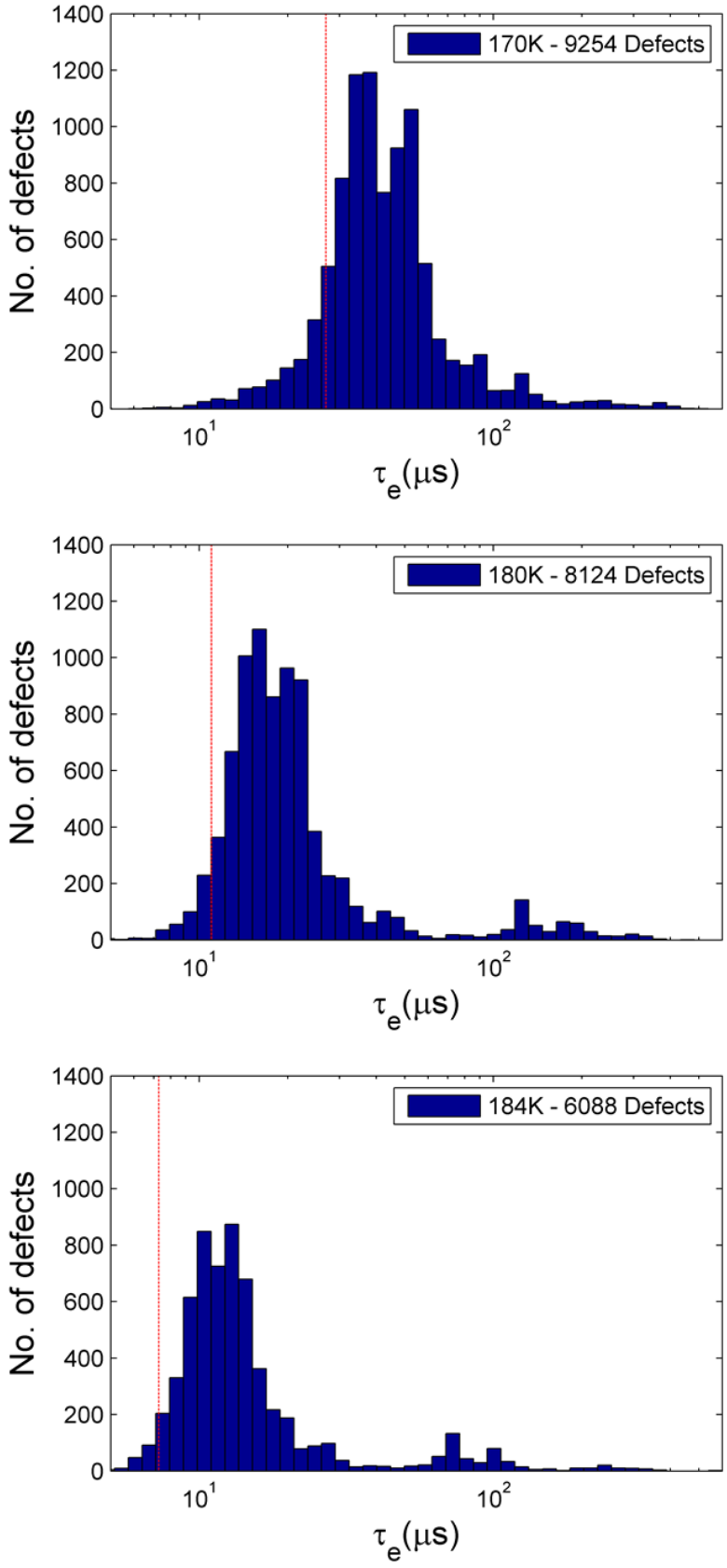

Figure 7.8 – A selection of the defect emission time constant distributions for 170-184K. The red line shows the expected value for the double-acceptor divacancy level as from Figure 7.1.

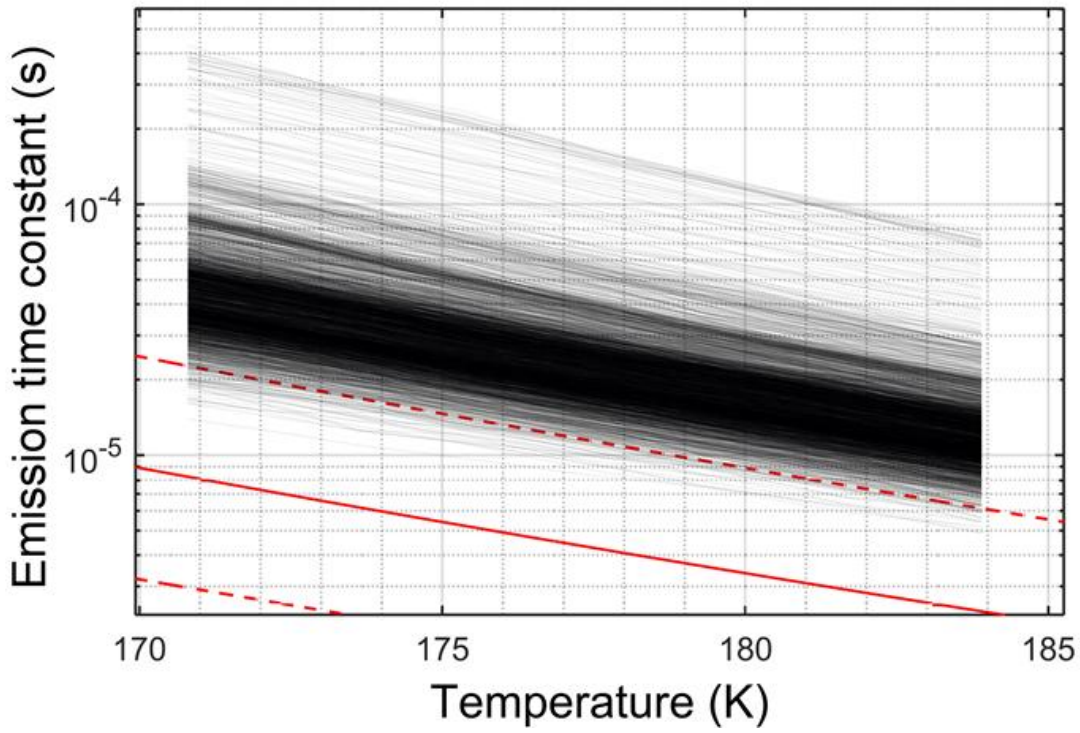

Figure 7.9 – The measured defect emission time constant against temperature for the 3849 defects observed across all temperatures. Each line represents a single defect. The red lines are the expected values for the double acceptor level of the divacancy as in Figure 7.1.

For those defects found at all temperatures the curves in Figure 7.9 were fit using Equation 4.3 to estimate the defect energy level and cross sections. The distributions are shown in Figures 7.10 and 7.11. Both show a dominant single Gaussian shaped peak indicating the presence of a single dominant defect species. The energy level at FWHM is found as:

$E = (E_c - 0.24 \pm 0.02)\ eV$

With the cross-section range is observed as:

$\sigma = (0.5\text{-}5)\ x10^{-19} m^2$

Both of these values are in agreement with the accepted values for the double acceptor level of the divacancy, although the energy level is at the high end of the range. This may be due to the fact that energy levels are only calculated for the defects which appear at all temperatures, which in this case are the slower defects (and hence those furthest from the conduction band edge) as the very fastest

defects have moved out of range of the trap-pumping technique by 184K, as seen from the reduction in fitted defects observed with increased temperature. There are no other defect species with a similar energy level expected to capture charge in an irradiated CCD at these temperatures and so it is concluded that at the temperature range 170-184K the dominant charge-trapping defect is the double acceptor level of the silicon divacancy, with an energy level of $E = (E_c - 0.24 \pm 0.02)\ eV$.

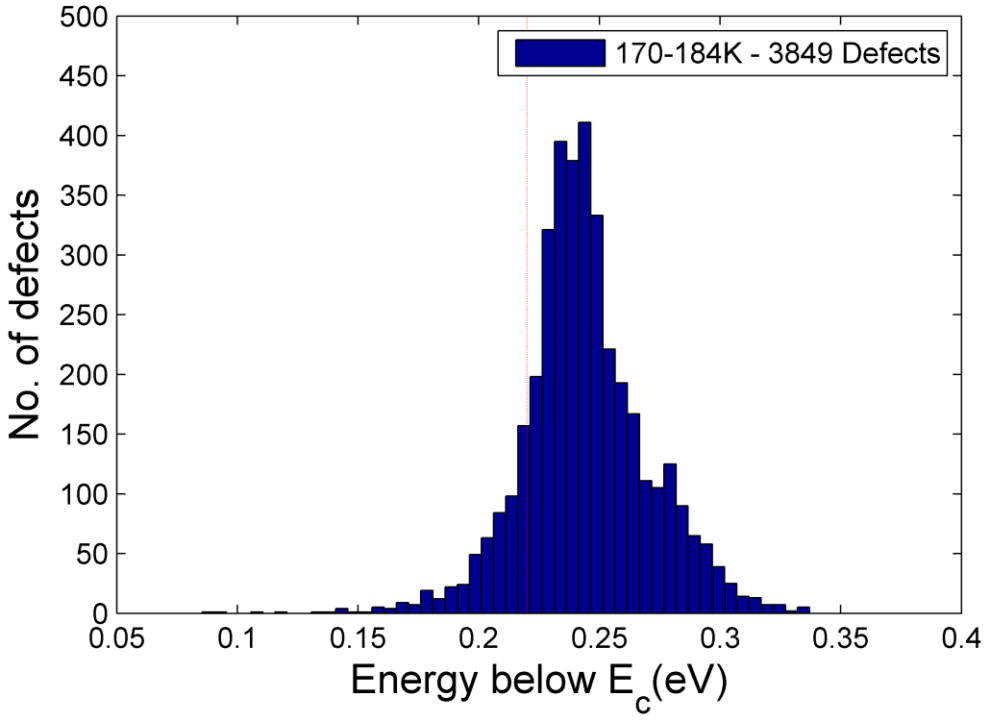

Figure 7.10– The energy level distribution for the 3849 defects found at all temperatures 170-184K. The red line shows the approximate energy level for the double acceptor level of the divacancy as reported in various DLTS studies.

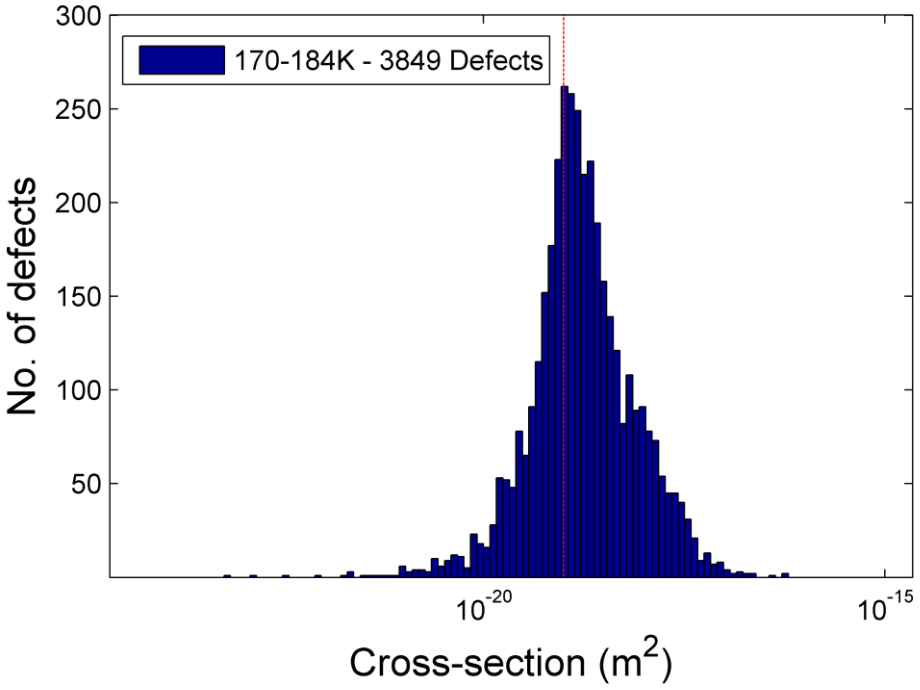

Figure 7.11 – The cross-section distribution for all defects found at all temperatures 170-184K. The red line shows the approximate cross-section for the double acceptor level of the divacancy as reported in various DLTS studies.

7.2.2 – Trap-pumping results: Temperature range 187-198K

The second temperature range tested was 187-198K. As seen in the results from the 170-184K testing the number of divacancy defects detected at 184K is almost a factor two lower than the number which were detected at 170K, since the defects become faster with increased temperature and begin to move out of range of the technique. It is therefore expected that by around 200K there will be very few of these defects detected, however the single acceptor level of the divacancy is also not expected to be detected in significant numbers at these temperatures, since it will be too slow. The aim of studying this temperature range was to both confirm these two expectations and also to probe if there are any charge-trapping defects of relevance. As outlined briefly earlier in this Chapter a paper by Holland in 1993 used X-ray CTI measurements to identify charge trapping defects in an n-channel CCD and found an unidentified defect with energy level $E = (E_c - 0.30)\ eV$. DLTS studies have

shown the existence of a possible hydrogen-related defect at around these energies in n-channel silicon (Svensson 1989; Hallen, 1996).

At 187K a total of 2209 defects were found and fit successfully. By 198K this was reduced to 502 defects, representing only around one defect per 650 pixels. Two of the defect emission time constant distributions are shown in Figure 7.12 along with the expected values for both the double acceptor level of the divacancy and the possible unknown defect. This Figure shows that at 191K two peaks are observed, indicating the presence of two separate defect species. However at 196K it can be seen that only one peak remains, since the other has moved out of range. From the emission time constants observed, the first (faster) peak is believed to show the remaining divacancy defects, which as predicted do indeed move out of range by around ~200K. This is a potentially important result for device optimisation in situations where this defect level is of concern, since with emission time constants less than ~*1 μs* no discernible CTI effects would be expected from it.

The second (slower) peak which remains at 196K has an emission time constant range of around *12-25* μs at this temperature, which is significantly different from the expected values for any of the predominant defect species. This is seen in Figure 7.13 which shows the defect emission time constant relationship with temperature for the 336 defects which were detected and fit successfully at all four temperatures. Again the data are overlayed onto the curves in Figure 7.1 and show that the observed emission time constants are not close to any of the expected charge-trapping defect levels in an n-channel CCD. Again a large spread is observed although there is a clear bunching at the centre of the distribution. Further evidence of the low measurement uncertainty is provided by the parallel nature of the lines for each individual defect.

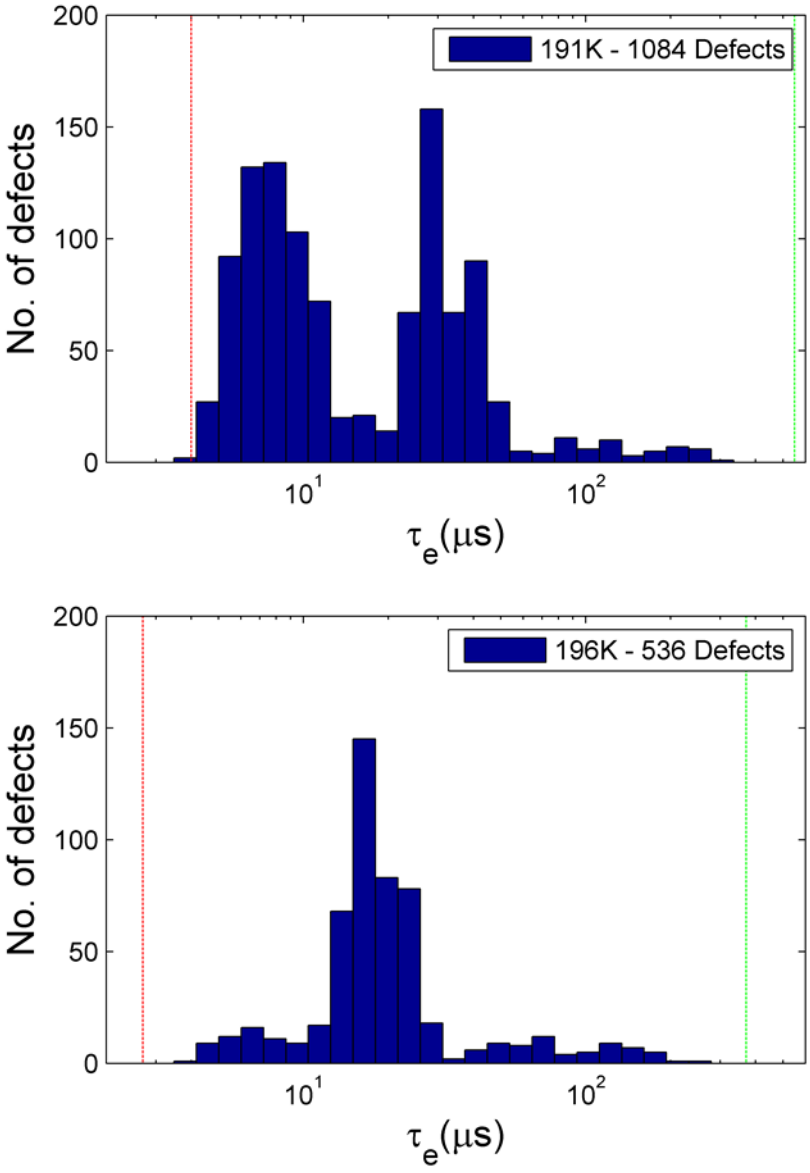

Figure 7.12 – Two of the defect emission time constant distributions from the 187-198K temperature range. The red and green lines show the expected values for the double-acceptor divacancy level and the "unknown" defect respectively, as from Figure 7.1.

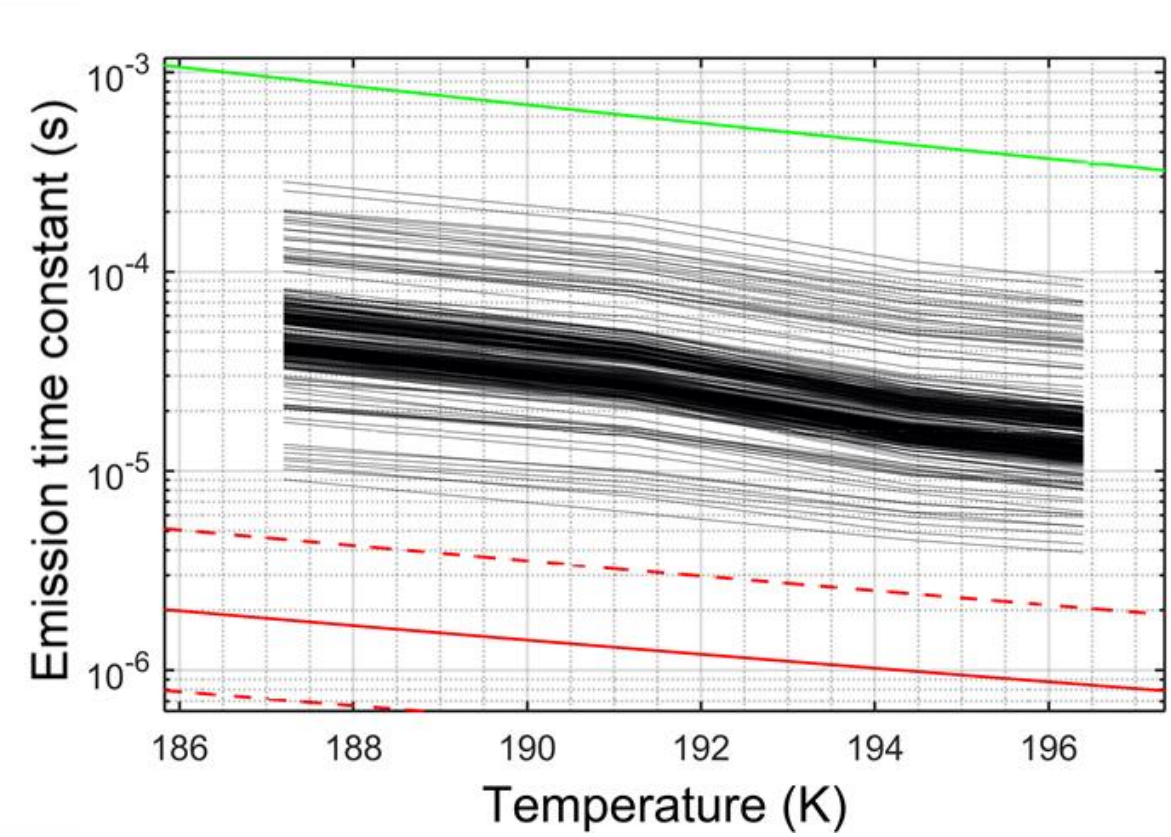

Figure 7.13 – The defect emission time constant against temperature for all 336 defects found at all temperatures. Each line represents an individual defect. The red and green lines show the expected values for the double-acceptor divacancy level and the "unknown" defect respectively, as from Figure 7.1.

For the defects appearing at all temperatures the energy level and cross-section analysis was carried out with the aim of potentially identifying the defect species which was observed. The distributions are shown in Figures 7.14 and 7.15. The energy level at FWHM was found as:

$E = (E_c - 0.30 \pm 0.015)\ eV$

With a cross-section range of:

$\sigma = (0.3\text{- } 4)\ x10^{-18} m^2.$

This is a very interesting result with respect to the work by Holland since the energy level quoted for the defect observed was $E = (E_c - 0.3)\ eV$. Although only present in low densities within the tested device, there is strong evidence that a charge-trapping defect level was observed with this energy

level and therefore there is the potential for further work towards classifying exactly which defect level it is. DLTS studies have shown the existence of a possible hydrogen-related defect at around *0.3 eV* below the conduction band edge in n-channel silicon (Svensson 1989; Hallen, 1996). The large difference in emission time constants compared to the calculated value for the "unknown" defect in Figure 7.1 could come from differences in the cross-section, which as shown in Chapter 3 have a significant effect and are difficult to measure accurately. Another important result is that if using an n-channel CCD with a line transfer time of the order of microseconds to hundreds of microseconds, then this temperature range appears optimal with respect to the number of defects which could negatively affect charge transfer performance since there are few defect levels with emission time constants in this time range.

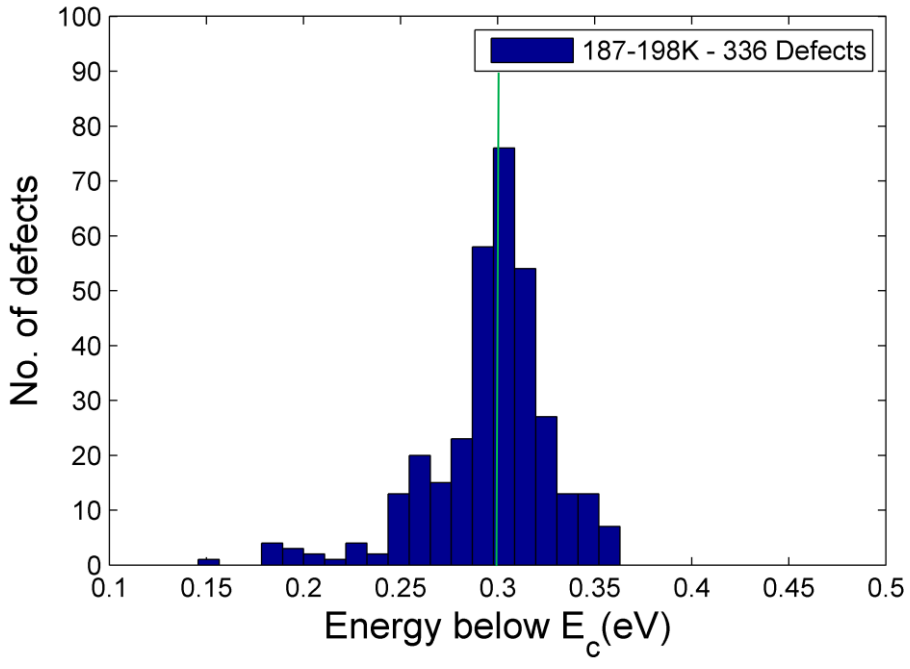

Figure 7.14 – The energy level distribution for all defects found at all temperatures in the range 187-198K. The green line shows the approximate energy level for the "unknown" defect as reported by Holland, (1993).

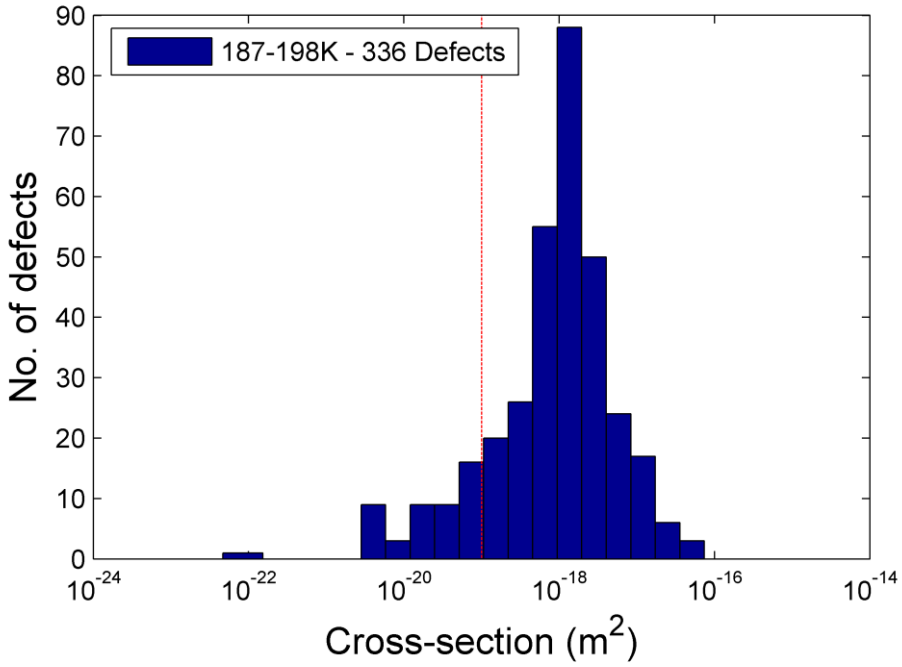

Figure 7.15 – The cross-section distribution for all defects found at all temperatures in the range 187-198K. The red line shows the value for the double acceptor level of the divacancy as reported by various DLTS studies. It can be seen that the observed cross-sections do not match this value, giving further evidence that the defects are of an "unknown" species.

7.2.3 – Trap pumping results: Temperature range 229-245K

The third temperature range tested was 229-245K, with the intention of analysing the single acceptor level of the silicon divacancy. A total of five temperatures were tested across this range. A selection of the emission time constant distributions are shown in Figure 7.16 with fixed axes and binning. A total of 2242 defects were found and fitted successfully at 229K, with the number falling to 1319 by 245K. At 229K there is a single dominant peak with an emission time constant range of around *80-200 µs*. By 245K there are two separate small peaks with emission time constant values of approximately *20-50 µs* and *150-280 µs*. The second (slower) peak only appears at the highest tested temperature, indicating the presence of a slow defect species which until this point was out of range of the technique. It is possible that these could be the VP defect although further testing around this temperature range would be required to gather further information.

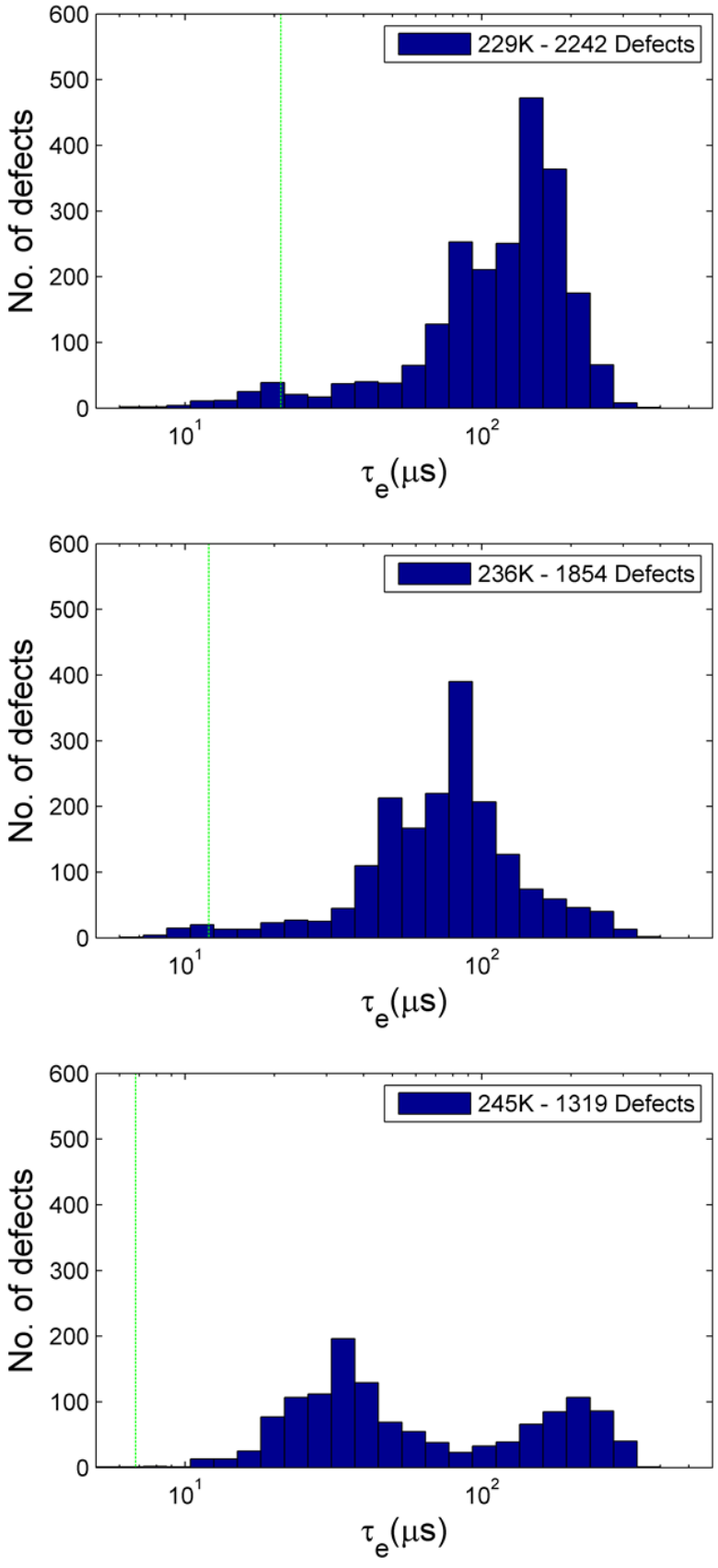

Figure 7.16 - A selection of the defect emission time constant distributions for the range 229-245K. The green line shows the expected time constant value at each temperature for the "unknown" defect, as in Figure 7.1.

The spread of the emission time constant distribution can be seen clearly in Figure 7.17 which shows the measured emission time constants for the 684 defects which were found at all five temperatures. It is also observed that the emission time constants lie quite far from the expected values for the single acceptor level of the divacancy and in fact are relatively close to the "unknown" defect curve. However the energy level and cross-section analysis which was performed (see Figures 7.18 and 7.19) showed an energy level at FWHM of:

$E = (E_c - 0.41 \pm 0.02)\ eV.$

This strongly suggests that the observed defects are indeed the single acceptor level of the silicon divacancy, for which the accepted literature value for energy level is around 0.41eV below the conduction band edge. The cross-section range at FWHM was observed as

$\sigma = (1 - 5)\ x10^{-18} m^2.$

These values are slightly high in comparison to the cross-section used to calculate the curve in Figure 7.1, however it is still in agreement within uncertainties with the values reported in the literature, for which there is a range larger than an order of magnitude. The difference in cross-section between the observed defects and the theoretical curve can explain the faster than expected emission time constants which were seen. All of the results suggest that at these temperatures the predominant charge-trapping defect level in an n-channel CCD is the single-acceptor level of the silicon divacancy, with an energy level of $E = (E_c - 0.41 \pm 0.02)\ eV$.

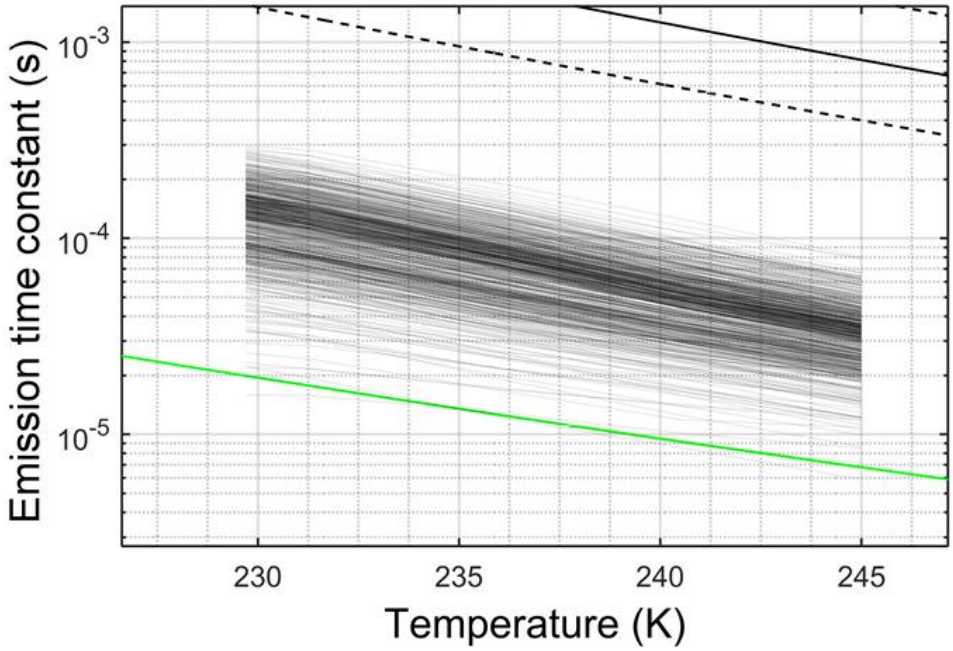

Figure 7.17 – The defect time constant against temperature for the 684 defects found at all temperatures in the range 229-245K. The green and black lines show expected values for the "unknown" defect level and the single acceptor level of the divacancy respectively, while the black dashed line shows a lower bound for the divacancy value.

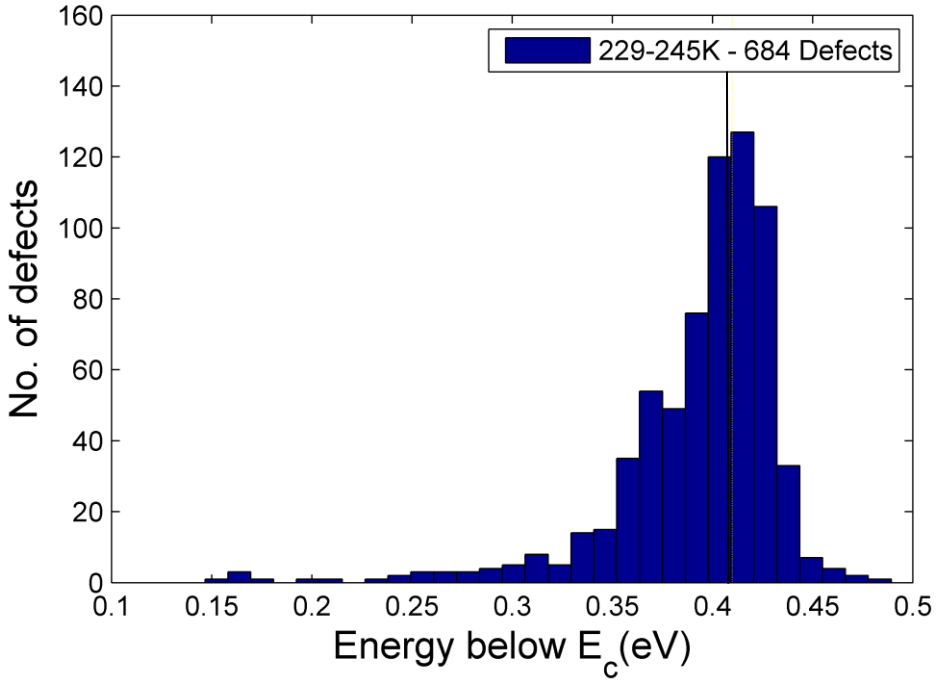

Figure 7.18 – The energy level distribution for all defects found at all temperatures in the range 229-245K. The black line shows the approximate energy level for the single acceptor level of the silicon divacancy as reported by various DLTS studies.

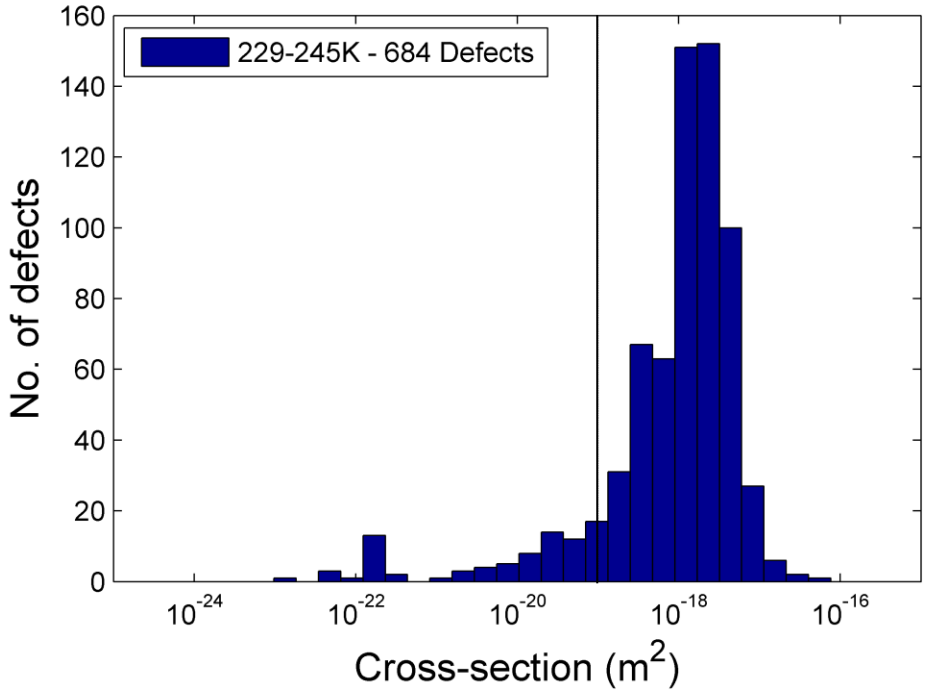

Figure 7.19– The cross-section distribution for all defects found at all temperatures in the range 229-245K. The black line shows the approximate cross-section for the single acceptor level of the silicon divacancy as reported by various DLTS studies.

7.3 – Summary

An n-channel CCD47-10 irradiated with protons to a 10 MeV equivalent fluence of 2.5×10^{9} p cm^{-2} was analysed using the method of single trap-pumping. An experimental test station was designed and built for this purpose, with the main aim of obtaining accurate emission time constant data for both acceptor levels of the silicon divacancy, as well as probing a temperature/clocking frequency region in which it is potentially optimal to run an n-channel CCD detector. Three temperature ranges were therefore selected for analysis; 170-184K, 187-198K and 229-245K. Signal dipoles were detected in sufficient numbers to generate statistics across all three temperature ranges. With respect to the individual defect emission time constant distributions, they exhibited similar properties to those observed in the p-channel CCD204 in the work in Chapter 5, showing significant spread, and the presence of a split-peak distribution in many cases. As discussed previously the spread in emission time data does not come from measurement uncertainty as shown by the

stability of the relationship between emission time constant and temperature for each individual defect. For this n-channel study temperature was controlled stringently, with readings taken and recorded for every trap-pumped image taken, and so it does not appear that all of the spread comes from temperature fluctuations either. Most likely a considerable portion of the spreading observed comes from effects of studying defects in an operational CCD, with the associated electric fields. Further work in this area to better quantify the emission time constant spread is required however it is clear that certainly with respect to image sensors it does not make sense to quote an exact emission time constant value for a particular defect level at a given temperature. This has potential consequences for radiation damage characterisation where operating conditions that could be expected to be optimum based on theoretical emission time constant values may in fact lead to signal charge encountering many charge-trapping defects.

Based on the energy level and cross-section estimates for defects appearing across multiple temperatures within a particular tested range, both the double and single acceptor levels of the silicon divacancy were observed, with energy levels of:

$E = (E_c - 0.24 \pm 0.02)$ eV - double acceptor level

$E = (E_c - 0.41 \pm 0.02)$ eV – single acceptor level

Both of these results match the energy levels reported in various DLTS studies in the literature. For the temperature range 187-198K a small number of the slowest double-acceptor level defects were observed as well as the presence of another defect level with energy level:

$E = (E_c - 0.30 \pm 0.015)$ eV

This is an interesting result as it matches the estimated energy level for the unknown defect level reported in (Holland, 1993). There is therefore evidence to support the existence of a defect level present in CCDs with this energy level, although appears with relatively low density compared to the two divacancy levels and so would remain a good operating region for a detector. Overall this study

has again shown the ability of the single trap-pumping method to measure defect emission time constants in a CCD with high resolution and has allowed for a more typical n-channel device to be analysed with the potential for results such as these to be inputted into future radiation damage models and correction algorithms, such as those described in Chapter 4.

Chapter 8 – Future work with single trap-pumping

The main focus of the work in this thesis has been to analyse charge-trapping defects in a CCD using the technique of single trap-pumping, with a focus on the accurate analysis of defect emission time constants and their relationship with temperature. However the advantages of the technique, and particularly the ability to locate individual defects, presents the opportunity for interesting avenues of further study such as the effect of various parameters on defect densities and emission constants, and the defect evolution under annealing (including at high-temperature). Presented here are brief initial studies into some of the potential areas for future work. All of the results in this Chapter were taken from the n-channel CCD4710 used for the work in Chapter 7 and using the same experimental test station.

8.1 – Defect emission time constant stability

As part of this work it was possible to run repeat trap-pumping studies under the exact same conditions but several days apart. This was done in order to test how stable the measured defect emission time constants were over repeat runs, since they have such a high sensitivity to changes in temperature and potentially other parameters such as electric field, local strain etc. The unprecedented resolution on emission time constant measurements which is achieved through trap-pumping enables any small changes to be observed. Four temperatures 171K, 172K, 174K and 175K were tested three times each with a period of approximately 24hrs between each run. The maximum temperature difference between any of the identical runs was 0.2K, as taken from the on-chip sensor. Table 8.1 shows a summary of the results. Approximately 10000 defects were found at each temperature. The variation in the number of defects found between each of the three identical runs (three identical runs at each temperature) was less than 2% for all temperatures. This shows that at least with respect to estimating defect density the technique of trap-pumping shows good

repeatability. Regarding the measured defect emission time constants the average deviation was around 3% between the three runs at each temperature, with a maximum deviation of around 25% observed particularly for some of the fastest defects. These results are important for several reasons. Firstly they reassure that the trap-pumping technique is able to take repeat measurements of the same device with good consistency. Secondly they provide useful information when estimating any uncertainties in the defect emission time constants measured throughout this work. Finally they also show that although in general there is a large spread observed in the distribution of measured defect emission time constants for a given set of conditions, each individual defect is relatively consistent. This provides further evidence that much of the observed spread seen repeatedly throughout this work is genuine and not either the result of measurement uncertainties or volatility of individual defect emission time constants.

Temperature (K)	Run	No. of defects	Max deviation in τ (%)	Avg deviation in τ (%)
170.8	1	9254	22.7	3.5
	2	9188		
	3	9311		
172.3	1	9339	23.5	3.4
	2	9348		
	3	9297		
173.6	1	9248	25.6	2.9
	2	9288		
	3	9165		
175.3	1	8643	24.7	4.6
	2	8613		
	3	8701		

Table 8.1 – A summary of the results from the repeat trap-pumping runs at 4 separate temperatures, showing the maximum and average percentage deviation found in the emission time constant results for a single defect across each run.

8.2– Effect of clock phase voltage

In Chapter 2 the effects of field on defect emission time constant was discussed, since it is expected to have a large effect and could potentially be a cause of the large spreads which are observed consistently in emission time constant distributions. It is possible for emission rates to be enhanced through particular alignment with an electric field via the Poole-Frenkel effect, or through quantum tunnelling effects (Martin, 1981; Ganichev, 2000). In a CCD pixel the electric field is complex, since the signal charge cloud has its own self-induced field along with those produced by the potential difference used to move charge. It is therefore very difficult to test the entire effect of electric field on defects within a CCD; however it is possible at least to test the effect of changing the phase voltages. As shown earlier in this Chapter the defect emission time constants are stable with respect to repeat measurements and so by changing the electrode voltages any significant changes could confidently be attributed to that change. Trap-pumping also provides a good opportunity for testing this due to the ability to analyse individual defects and the high resolution possible in measuring defect emission time constant distributions.

The effect of clock phase voltage was tested at 172K with using seven voltages between 8-14V. No significant differences were observed in the number of defects found at each tested voltage. A total of 6013 defects were found and fitted successfully at all seven voltages. For these defects no change was observed with changing voltage; the mean defect emission time constant at 8V is *41.8 μs* and the mean at 14V is also *41.8 μs*. The largest deviation the mean observed at any of the tested voltages was less than 1%. As an example of the stability of the emission time constants, Figure 8.1 shows for a random selection of defects the measured time constant against voltage. Each individual line represents a single defect and it can be seen that although there are small individual fluctuations as expected there is no overall effect. This is a useful result in showing that the gate voltage is not a concern when considering device optimisation for charge transfer, however it also

gives evidence that any field effects in a CCD if present must come from sources other than the gate voltage and are difficult to measure or predict.

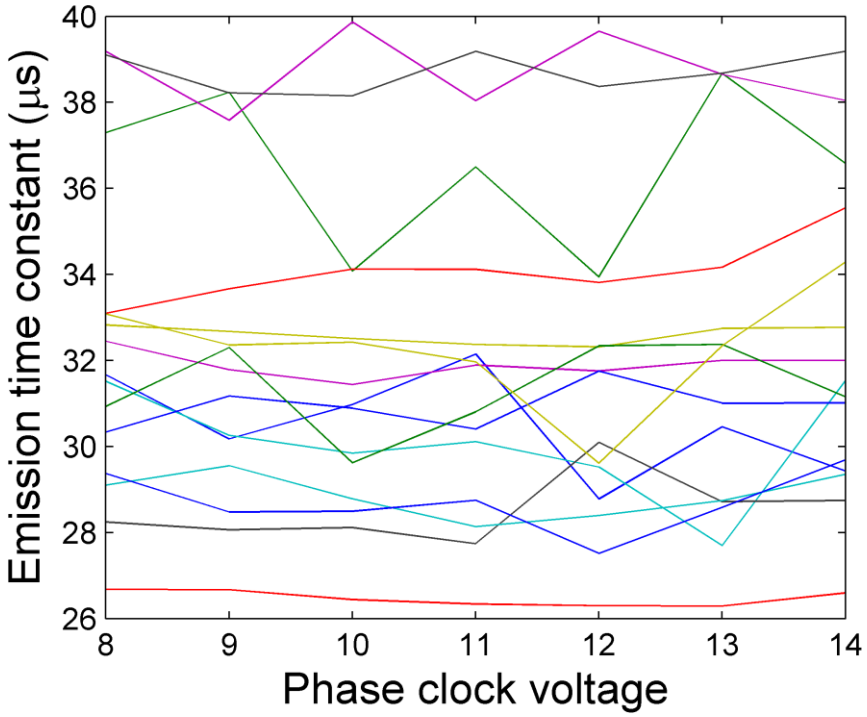

Figure 8.1 – The defect emission time constant against phase voltage for a small selection of the 6013 defects which were found at all tested voltages between 8-14V. Each individual line represents a single defect. It can be seen that changing voltage has no discernible and systematic effect on emission time constant.

8.3 – Signal level effects

As outlined in Chapter 4 the signal level within a CCD is expected to affect the number of defects found through trap-pumping, since a larger signal level implies a physically larger charge cloud and therefore more defects are expected to be encountered by it. For this reason signal level is known to affect the CTI of a device (see for example Hardy, 1998). To test the effects of signal level on the number of signal dipoles found two temperatures were tested, 165K and 169K, where from earlier work it was known a significant number of charge trapping defects are present. In this study only the number of signal dipoles found was analysed, and so no intensity curves were produced or fitted. Two separate phase time values of *50* and *500* µs were tested at each temperature. The results are

shown in Figure 8.2. Three of the four curves show the expected result that increasing the signal level leads to an increase in the number of signal dipoles which are observed. This is important for trap-pumping studies as it shows both the importance of choosing a suitable signal level and also the approximations that are made with respect to defect density estimations using the technique. Studies of this kind could also potentially help to further understand charge distribution in a CCD which is difficult to model accurately. The data could be used as part of confirmation of a model of the charge cloud size for a given signal level in a particular CCD pixel structure.

One of the curves however shows an unexpected result; at 169K and *500 μs* phase-time the number of signal dipoles initially rises sharply before falling with signal level over the range ~2000-4000 ADU. Following this point the curve begins to follow the expected trend. The result does not appear to be related to issues with noise or measurement uncertainties as the curve follows a strong trend even when the number of dipoles is being reduced. It is possible that there were issues with the temperature control during the taking of this data, which could lead to a situation where the number of defects within range are reduced as the temperature settles . However, currently there is no clear explanation for why the number of signal dipoles might be reduced with increasing signal level, particularly when the expected trend was observed for the other three tests. This experiment would therefore be a strong candidate to be repeated, with further work required to test whether this unexpected result was a one-off or is a real effect.

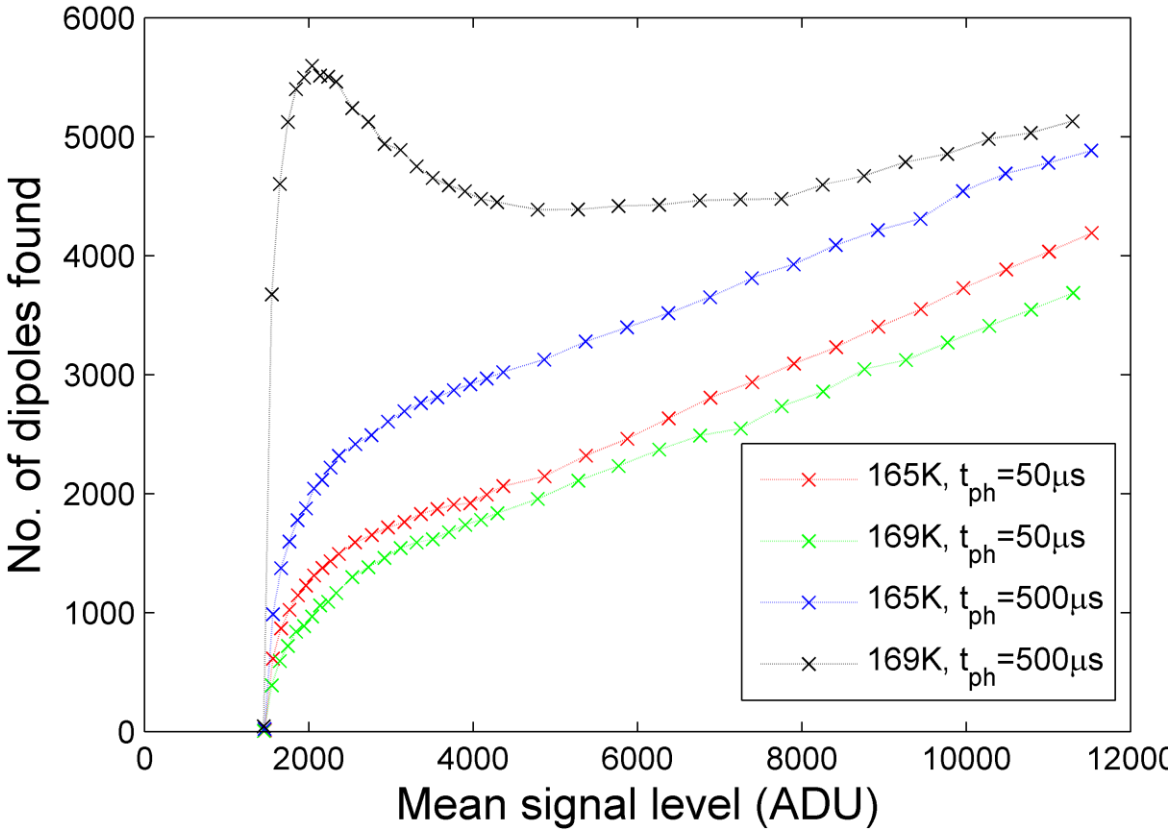

Figure 8.2 – The number of signal level dipoles found using a 3σ threshold for the background signal level, for two different phase times at two different temperatures. Note the black curve which shows an unexpected result where the number of dipoles found decreases with increasing signal level over a small range.

8.4 – Summary

The ability of the trap-pumping technique to locate charge-trapping defects in a CCD and accurately measure their time constants on an individual basis leads to the possibility of several interesting areas for further work which were outside the main scope of this thesis but have been introduced with some preliminary results. The stability of defect emission time constants over periods of several days was monitored, with the average deviation for approximately 10000 defects being around 3% over the course of three trap-pumping datasets. This shows that even under CCD operating conditions emission time constants at a given temperature are relatively stable, and that the large spreading observed in many of the distributions seen in earlier work in this thesis is not caused

simply by fluctuations in the measured value. The effect of clock phase voltage on defect emission time constants was also tested as a potential source of the observed spread. For the small dataset taken no discernible effect was observed and measured values remained relatively constant, however this also remains an opportunity for further work in order to better understand any possible field effects resulting from an increase in electrode voltage.

The effect of signal level on the number of defects observed showed the expected trend in 3 out of 4 tested cases; the increased signal level and so increased physical size of the charge cloud results in more defects being encountered. In one tested case however there was an unexpected result at low signal which is currently unable to be explained. This confirms signal level effects as an interesting topic for further work, firstly to observe if such an effect occurs again under certain conditions and then if so to try to explain it. This data could also potentially be used to help confirm charge cloud size for a given signal level in models of CCD pixel structures.

Chapter 9 – Conclusions

This Chapter summarises the main results from this study and their impact, as well as potential areas for future work.

9.1 – Development of the single trap-pumping method

The idea of manipulating the charge transfer process in a CCD has been previously used to detect potential pockets from the design and production processes (pocket-pumping) and at the time of starting this work had begun to be developed into a tool for probing radiation induced defects to study their relationship with CTI and begin to analyse some of their properties. For this work the method of single trap-pumping was further developed into a tool for the precise analysis of defect emission time constants in both 3-phase and 4-phase CCDs, giving unprecedented accuracy on measurements. The technique has been shown to be a powerful tool for defect emission time constant analysis with the potential for providing the highly accurate data required if future space-based CCD detector missions are not going to have their scientific goals compromised by radiation damage effects. The work done to allow single trap-pumping in a 4-phase CCD and particularly one with unequal clock phase widths has also given rise to interesting effects relating to the position of a defect beneath a particular phase and/or interference between two or more defect levels. With further development and modelling of the numerous potential resulting signal dipole curves this could prove to be a useful method for locating defects to a sub-pixel resolution in 4-phase devices and potentially studying properties of defects which are not within the limits of analysis for single defect only curves.

9.2 – Study of a proton irradiated p-channel CCD204

A p-channel CCD204 irradiated with protons to a 10MeV equivalent fluence of 4.0×10^{9}p cm^{-2} was analysed across two temperature regions of 149-159K and 172-180K using the method of single trap-pumping. The main results are summarised here:

- The technique was able to successfully locate individual defects from the signal dipoles produced in a trap-pumped image and obtain defect emission time constants with high resolution.
- The emission time constant distributions at each tested temperature showed the presence of significant spread which is not associated to measurement uncertainties. This spread is likely the culmination of a number of effects including the fact that defects are studied in an operational CCD. Further work would be required to better understand the exact sources of this spread.
- Many of the emission time constant distributions exhibited a split-peak which arises due to the effects of interphase trapping during CCD readout (Skottfelt, 2018). From the energy level estimates for those defects appearing at all tested temperatures in a given range no evidence was found for the presence of multiple defect species at a single temperature.
- Between 149-159K the dominant defect level observed within the tested phase time range of ~*1-10000 μs* was the donor level of the silicon divacancy with an energy level of $E = (E_v + 0.21 \pm 0.02)$ *eV*.
- Between 172-180K the dominant defect observed was the carbon interstitial defect with an energy level of $E = (Ev + 0.31 \pm 0.02)$ *eV*.
- Both of the energy level estimates closely match results reported in various DLTS studies for the two respective defect levels.

Overall the method of single trap-pumping was shown to be highly effective in probing defect emission time constants with excellent resolution. This has potential impact for CCD detector missions in terms of device optimisation and radiation damage mitigation algorithms, where defect parameters will be required to the level of a few percent or better. The results and further work using the technique on p-channel CCDs can also be used to build a case for or against the use of such devices over more standard n-channel CCDs in terms of tolerance to radiation damage at operational temperatures and operating speeds.

9.3 – Analysis of a cryogenically-irradiated p-channel CCD204 and subsequent room-temperature anneal study.

The effect of device temperature during irradiation on the defect distribution post-irradiation was studied. Two proton irradiated p-channel CCD204 devices were used for this work; one irradiated at 153K and one at room-temperature.

- Results from the RT device tested at 153K showed a dominant defect species with an emission time constant strongly suggesting the donor level of the silicon divacancy. A small number of a second defect species was also present with an emission time constant relating to the carbon interstitial defect.
- Initial results from the cryogenic device post-irradiation at 153K show a large reduction in the number of defects detected within the tested phase-time range. In particular there is an approximate 10x reduction in the observed number of silicon divacancies.
- Following the first anneal stage a large increase in the number of divacancy defects was observed in the cryogenic device when tested at 153K.
- Over the subsequent anneal stages culminating in an approximate total time of 10 months at room-temperature, the defect distribution undergoes several changes whilst appearing to be converge to a very similar distribution to that observed in the RT device

- The two dominant defect species throughout remain the donor level of the silicon divacancy and the carbon interstitial defect.

The most important results from this work are the large differences observed post-irradiation between the two devices, and the large increase in divacancy defects observed post room-temperature anneal. These results have significant impact since currently all radiation testing is carried out on devices irradiated at room-temperature, even if the device will be operating cryogenically whilst receiving radiation damage. Therefore predictions of damage based on such tests will not give representative results and may result in incorrect device optimisation. It is also apparent that any potential benefits of a cryogenic irradiation with respect to device performance are lost if the conditions are not maintained. Cryogenic irradiation studies therefore offer a fascinating avenue for further work and indeed based on these results and the wider study that this work was part of significant resources have been committed to such an investigation.

9.4 – Trap-pumping analysis of a proton irradiated n-channel CCD47- 10

Similar to the work carried out in Chapter 4 on the p-channel CCD204, an n-channel CCD47-10 irradiated with protons to a 10 MeV equivalent fluence of 2.5×10^{9} p cm^{-2} was analysed using the method of single trap-pumping with the main aim of accurately measuring defect emission time constants for both the single and double-acceptor levels of the silicon divacancy. An experimental test station was designed specifically for this purpose. The main results are summarised below:

- Signal dipoles were observed at all tested temperatures allowing for the measurement of defect emission time constants.
- Emission time constant distributions again showed considerable spreading, and often the presence of a split peak, as seen in the p-channel case.

- For the temperature range 170-184K the dominant defect species observed using the tested phase-time range of ~*1-500 μs* was the double level of the silicon divacancy, with an energy level of $E = (E_c - 0.24 \pm 0.02)\ eV$.
- For the range 229-245K the dominant defect species observed was the single level of the silicon divacancy with an energy level $E = (E_c - 0.41 \pm 0.02)\ eV$.
- A third temperature range of 187-198K was tested and a small number of defects were observed with an energy level of $E = (E_c - 0.30 \pm 0.015)\ eV$. This matches the energy level for a presently unknown defect species reported by Holland (1993).
- Initial analysis was carried out into the effects of signal level on the number of observed defects, which showed in 3 out of 4 tested cases the expected trend of an increase in signal level resulting in more defects being found. A brief study of the potential effects of phase voltage on defect emission time constant was also carried out and showed no discernible relationship. Both of these subjects remain areas for future work using the trap-pumping technique.

Both the single and double-acceptor levels of the silicon divacancy were observed, with energy level estimates closely matching the values reported from various DLTS studies in the literature. Again the single-trap-pumping technique demonstrated its ability to measure defect emission time constants of important charge-trapping levels in CCDs with the accuracy which will be required going forward for space-based CCD detector missions.

Overall the work throughout this thesis has provided previously unseen insight into the behaviour of charge-trapping deep-level defects in CCDs and has provided several interesting and important avenues for further work. The use of CCDs as imaging and spectroscopy sensors for space-based telescopes looks set to continue for the foreseeable future and it is hoped that work such as this can be of use for improving device performance in order to answer the exciting and intriguing scientific questions which are driving such missions.

Bibliography

1. F. Auret, P. Deenapanray, “Deep level transient spectroscopy of defects in high-energy light-particle irradiated Si,” *Crit. Rev. Solid State,* **29**(1) p1, 2004.

2. M. Balkanski, “Semiconductor Physics and Applications,” *O.U. Press*, 2000.

3. E. K. Banghart, J. P. Lavine, E. A. Trabka, E. T. Nelson, B. C. Burkey, “A model for charge transfer in buried-channel charge-coupled devices at low temperature,” *IEEE Trans. Electron Devices* **38**(5) p1162, 1991.

4. G. A. Baraff, E. O. Kane, M. Schlueter, “Theory of the silicon vacancy: An Anderson negative-U system,” *Phys. Rev. B* **21**(12) p5662, 1980.

5. W.S. Boyle, G.E. Smith, “Charge Coupled Semiconductor Devices,” *Bell Systems Technical Journal* **49**(4) p587, 1970.

6. A. S. Clarke, D. J. Hall, a Holland, D. Burt, “Modelling charge storage in Euclid CCD structures,” *J. Instrum.* **7**(1) C01058, 2012.

7. K. Dawson, J. Bebek, J. Emes *et. al*., “Radiation Tolerance of Fully Depleted P-Channel CCDs Designed for the SNAP Satellite,” *IEEE Trans. Nucl. Sci*. **55** p1725, 2008.

8. J. Endicott, S. Darby, S. Bowring, D. Burt, T. Eaton, A. Grey, I. Swindells, R. Wheeler, L. Duvet, M. Cropper, D. Walton, A. Holland, N. Murray, J. Gow, “Charge-coupled devices for the ESA Euclid M-class mission,” *Proc. SPIE - Int. Soc. Opt. Eng.* **8453** , 2012.

9. V. Eremin, A. Ivanov, E. Verbitskaya, Z. Li, S. U. Pandey, “Analysis of divacancy related traps induced by proton, neutron and gamma radiation in high resistivity silicon detectors,” *Nucl. Instruments Methods Phys. Res. Sect. A* **426**(1) p120, 1999.

10. J. H. Evans-Freeman, A. R. Peaker, I. D. Hawkins, P. Y. Y. Kan, J. Terry, L. Rubaldo, M. Ahmed, S. Watts, L. Dobaczewski, “High-resolution DLTS studies of vacancy-related defects in irradiated and in ion-implanted n-type silicon,” *Mater. Sci. Semicond. Process.* **3**(4) p237, 2000.

11. B. A. Fowler, A. E. Gamal, D. X. D. Yang, H. Tian, “Method for estimating quantum efficiency for CMOS image sensors,” *proc. SPIE* **3301**, 1998.

12. A. R. Frederickson, A. S. Karakashian, P. J. Drevinsky, C. E Caefer, “Radiation-induced carbon-related defects in p-type silicon,” *J. Appl. Phys.* **65**(8) p3272 , 1989.

13. E. Fretwurst, M. Kuhnke, G. Lindström, M. Moll, “Radiation Hardness of Silicon Detectors for Applications in High-Energy Physics Experiments,” *J. Optoelectron. Adv. Matter.*, **2**(5) p575, 2000.

14. S. D. Ganichev, E. Ziemann, W. Prettl, I. N. Yassievich, A. A. Istratov, E. R. Weber, “Distinction between the Poole-Frenkel and tunneling models of electric-field-stimulated carrier emission from deep levels in semiconductors,” *Phys. Rev.* **61**(15) p361, 2000.

15. J. P. D. Gow, N. J. Murray, A. D. Holland, D. J. Hall, M. Cropper, D. Burt, G. Hopkinson, L. Duvet, “Assessment of space proton radiation-induced charge transfer inefficiency in the CCD204 for the Euclid space observatory,” *J. Instrumentation* **7** C01030, 2012.

16. J. P. D. Gow, D. Wood, D. Burt, D. J. Hall, B. Dryer, A. D. Holland, N. J. Murray, “Initial results from

a cryogenic proton irradiation of a p-channel CCD," *Proc. SPIE*, 2015.

17. A.S. Grove, "Physics and Technology of Semiconductor Devices," *Wiley Press,* 1967.

18. D. J. Hall, N. J. Murray, A. D. Holland, J. Gow, A. Clarke, D. Burt, "Determination of in situ trap properties in Charge Coupled Devices using a single-trap ' pumping ' technique," *IEEE Trans. Nuc. Sci*, **61**(4) p1826, 2014.

19. N. Hall, 'Electron-hole recombination in germanium', *Phys. Rev.* **87** p387, 1952.

20. A. Hallen, N. Keskitalo, "Lifetime in proton irradiated silicon," *J. Appl. Phys.* **79**(8) p3906, 1996.

21. T. Hardy, R. Murowinski, M. J. Deen, "Charge transfer efficiency in proton damaged CCD's," *IEEE Trans. Nucl. Sci.* **45** p154, 1998.

22. A. D. Holland, "The effect of bulk traps in proton irradiated EEV CCD's," Nucl. Instrum. Methods **326** p335, 1993.

23. S. E. Holland, D.E. Groom, N.P. Palaio, R.J. Stover, M.Wei, "Fully-Depleted, Back-Illuminated Charge-Coupled Devices Fabricated on High-Resistivity Silicon," *IEEE Trans. Electron Devices*, **50**(1), 2003.

24. G.R. Hopkinson, C.J. Dale, P.W. Marshall, "Proton effects in charge-coupled devices," *IEEE Transactions on Nuc. Sci*. **43**(2) p614, 1996.

25. G. R. Hopkinson, "Radiation effects on CCDs for spaceborne acquisition and tracking applications," *Proc. RADECS,* 1991.

26. J. Janesick, "Scientific Charge-Coupled Devices," *SPIE Press,* 2001.

27. L. C. Kimerling, H. M. DeAngelis, J. W. Diebold, "On the role of defect charge state in the stability of point defects in silicon," *Solid State Commun.* **16** p171, 1975.

28. L. C. Kimerling, *Radiation Effects in Semiconductors Conference 1976* (*Inst. Phys. Conf. Ser. 31*), 1977.

29. C. Kittel, "Introduction to Solid-state Physics", *John Wiley & Sons,* 1996.

30. R. Kohley, "Gaia: operational aspects and tests of Gaia Flight Model CCDs," *Proc. SPIE* **7439**, 2009.

31. M. S. Lazo, D. M. Woodall, P. J. McDaniel, "Silicon and silicon dioxide neutron damage functions," *Proc. Fast Burt React. Workshop*, 1986.

32. G. Lindström, "Radiation damage in silicon detectors," *Nucl. Instruments Methods Phys. Res. Sect. A.* **512** p30, 2003.

33. C. A. Londos, "Defect States in Electron-Bombarded n-Type Silicon," *Phys. Stat. Sol.* **113** p503, 1989.

34. D. H. Lumb, "CCD radiation damage in ESA Cosmic Vision missions: assessment and mitigation," *Proc. SPIE* **7439**, 2009.

35. G. Lutz, "Applications of Charge-Coupled Devices," *Springer*, 1999.

36. L. F. Makarenko, S. B. Lastovski, F. P. Korshunov, L. I. Murin, M. Moll, "Primary defect transformations in high-resistivity p-type silicon irradiated with electrons at cryogenic

temperatures," *Phys. B Condens. Matter* **404** p4561, 2009.

37. D. Maneuski, "Simulation of the charge transfer inefficiency of column parallel CCDs," *Nucl. Instruments Methods Phys. Res. Sect. A* **591**(1) p252, 2008.

38. C. Marshall, P. Marshall, A. Wczynski *et al.*, "Comparisons of the proton-induced dark current and charge transfer efficiency responses of n- and p-channel CCDs," *Proc. SPIE* **5499**, 2004.

39. P. A. Martin, B. G. Streetman, K. Hess, "Electric field enhanced emission from non-Coulombic traps in semiconductors," *J. Appl. Phys.* **52** p7409, 1981.

40. R. Massey, C. Stoughton, A. Leauthaud, J. Rhodes, R. Ellis, E. Shaghoulian, "Pixel-based correction for Charge Transfer Inefficiency in the Hubble Space Telescope Advanced Camera for Surveys," MNRAS **401**, 2010.

41. R. Massey, H. Hoekstra, T. Kitching, J. Rhodes, M. Cropper, J. Amiaux,D. Harvey, Y. Mellier, M. Meneghetti, L. Miller, S. Paulin-Henriksson,S. Pires, R. Scaramella and T. Schrabback,"Origins of weak lensing systematics, and requirements on future instrumentation (or knowledgeof instrumentation)", MNRAS **429**(1) p661, 2013.

42. R. Massey, T. Schrabback, O. Cordes, O. Marggraf, H. Israel, L. Miller, D. Hall, M. Cropper, T. Prod'homme, S.-M. Niemi, "An improved model of Charge Transfer Inefficiency and correction algorithm for the Hubble Space Telescope," *Mon. Not. R. Astron. Soc* **907**, 2014.

43. P. M. Mooney, L. J. Cheng, M. Suli, J. D. Gerson, J.W. Corbett, "Defect Energy Levels in Boron Doped Silicon Irradiated With 1Mev Electrons," *Phys. Rev. B* **15**(8) p3836 , 1977.

44. N. J. Mostek, C. J. Bebek, A. Karcher, W. F. Kolbe, N. A. Roe, L. Berkeley, "Charge trap identification for proton-irradiated p+ channel CCDs," *Proc. SPIE* **7742**, 2010.

45. N. J. Murray, A. D. Holland, J. P. D. Gow, D. J. Hall, J. H. Tutt, D. Burt, J. Endicott, "Mitigating radiation-induced charge transfer inefficiency in full-frame CCD applications by 'pumping' traps," *SPIE High Energy, Opt. Infrared Detect. Astron. V* **8453**, 2012.

46. N. J. Murray, D. J. Burt, D. Hall, A. D. Holland, "The relationship between pumped traps and signal loss in buried channel CCDs," *SPIE Opt. Eng. + Appl.* **44**, 2013.

47. R.C. Newman, "Defects in silicon," *Reports on Progress in Physics* **45** p1163, 1982.

48. C. Nyamhere, P. N. K. Deenapanray, F. D. Auret, F. C. Farlow, "Characterization of defects created in Cz and epitaxial Si doped with Ga or B using Laplace-DLTS," *Phys. B Condens. Matter* **376** p161, 2006.

49. M. C. M. O'Brien, "The Jahn–Teller effect: An introduction and current review," *American Journal of Physics* **61**(8) p688, 1993.

50. P. Pichler, "Intrinsic Point Defects, Impurities, and their Diffusion in Silicon", *Springer*, 2004.

51. B. Prod'homme, T., Holl, L. Lindegren, A. G. A. Brown, "The impact of CCD radiation damage on Gaia astrometry - I. Image location estimation in the presence of radiation damage," *Mon. Not. R. Astron. Soc.* **422** p2786, 2012.

52. W. Shockley, W. T. Read Jr., "Statistics of the Recombination of Holes and Electrons," *Phys. Rev.* **87**(5) p835, 1952.

53. A. Short, C. Crowley, J. H. J. de Bruijne, T. Prod'homme, "An analytical model of radiation-

induced charge transfer inefficiency for CCD detectors," *Mon. Not. R. Astron. Soc.* **430** p3078, 2013.

54. L. W. Song, X. D. Zhan, B. W. Benson, G. D. Watkins, "Bistable interstitial-carbon-substitutional-carbon pair in silicon," *Phys. Rev. B* **42**(9) p5765 , 1990.

55. J. Skottfelt, D. J. Hall, B. Dryer, N. Bush, J. P. D. Gow, A. D Holland, "Importance of charge capture in interphase regions during readout of charge-coupled devices," *J. Astrom. Telesc. Instrum. Syst* **4**(1) p018005 , 2018.

56. J. R. Srour, C. J. Marshall, P. W. Marshall, "Review of displacement damage effects in silicon devices," *IEEE Trans. Nucl. Sci.* **50**(3) p653, 2003.

57. B. G. Svensson, A. Hallén, B.U.R. Sundqvist, "Hydrogen-related electron traps in proton-bombarded float zone silicon," *Materials Science and Engineering B*, 1989.

58. B. G. Svensson, J.Lindstrom, "Generation of divacancies in silicon by MeV electrons," *J. Appl. Phys.* **72**(12) p5616, 1992.

59. R. H.Walden, R. H. Krambeck, R. J. Strain, J. Mckenna, N. L. Schryer, G. E. Smith, "The Buried Channel Charge Coupled Device," B.S.T.J. **51**, p1635, 1972.

60. G. D. Watkins, J. W. Corbett, "Electron Spin Resonance of the Si-A Center," *Phys. Rev.* **121**(4) p1001, 1961.

61. G. D. Watkins, J. W. Corbett, "Electron Paramagnetic Resonance and Electron Nuclear Double Resonance of the Si-E Center," *Phys. Rev.* **134**(5) p1359, 1964.

62. G. D. Watkins, "A review of EPR studies in irradiated silicon," *Radiation Damage in Semiconductors 1964,* p97, 1964.

63. G. D Watkins, J. W. Corbett, "Electron Paramagnetic Resonance of the Divacancy," *Phys. Rev.* **138** p543, 1965.

64. G. D. Watkins, "Negative-U properties for point defetcs in silicon," *Phys. Rev. Lett.* **44**(9) p593, 1980.

65. G. D. Watkins, "Intrinsic defects in silicon," *Mater. Sci. Semicond. Process.* **3**(4) p227, 2000.

66. S. J. Watts, "Overview of radiation damage in silicon detectors - Models and defect engineering," *Nucl. Instruments Methods Phys. Res. Sect. A Accel. Spectrometers, Detect. Assoc. Equip.* **386**(1) p149, 1997.

67. N. Zangenberg, J. J. Goubet, A. Nylandsted Larsen, "On-line DLTS investigations of the mono- and di-vacancy in p-type silicon after low temperature electron irradiation," *Nucl. Instruments Methods Phys. Res. Sect. B* **186** p71, 2002.

68. O. Zeynali, D. Masti, S. Gandomkar, "Shielding Protection of Electronic Circuits Against Radiation Effects of Space High Energy Particles," *Adv. Appl. Sci. Res.* **3**(1) p446, 2012.

69. S. Zhao "Defect reactions and impurity control in silicon," *PhD thesis*, 1997.